Thermal Measurements with a 2S Module on a TEDD-like Structure for the CMS Phase-2 Upgrade

Masterarbeit in Physik

von

Vanessa Oppenländer

vorgelegt der
Fakultät für Mathematik, Informatik und Naturwissenschaften der
RWTH Aachen

im
November 2023

angefertigt im
I. Physikalischen Institut B

bei
Prüfer: Prof. Dr. Lutz Feld
Zweitprüfer: Prof. Dr. Oliver Pooth

Contents

1 Introduction 1

2 The LHC and the CMS Experiment 3
- 2.1 The Large Hadron Collider . . . 3
- 2.2 The Compact Muon Solenoid Experiment . . . 4

3 The High Luminosity LHC and the Phase-2 Upgrade 9
- 3.1 The High Luminosity LHC . . . 9
- 3.2 The CMS Phase-2 Upgrade . . . 9
  - 3.2.1 The CMS Phase-2 Tracker . . . 9
- 3.3 Cooling of the Phase-2 Tracker . . . 10
  - 3.3.1 The 2PACL Principle . . . 11
  - 3.3.2 CO_2 as a Coolant . . . 11

4 The 2S Module 13
- 4.1 Description of the 2S Module Design . . . 13
- 4.2 General Concept of the p_T Module . . . 14
- 4.3 Power Consumption of the 2S Module . . . 15
- 4.4 CO_2 Cooling and Thermal Design . . . 17
  - 4.4.1 Thermal Design of the 2S Module . . . 17
  - 4.4.2 CO_2 Cooling in the TEDD . . . 18
  - 4.4.3 Thermal Runaway . . . 19

5 Experimental Setup 21
- 5.1 CO_2 Cooling System . . . 21
- 5.2 Module Cooling Box . . . 22
- 5.3 Cooling Structure and Inserts . . . 23

6 Preparatory Measurements 27
- 6.1 Thermal Characterization of Temperature Sensors . . . 27
- 6.2 Gluing Tests of Temperature Sensors on Dummy Sensors . . . 30
- 6.3 Gluing of Temperature Sensors on the 2S Module . . . 33
- 6.4 Generation of Leakage Current with LEDs . . . 35
  - 6.4.1 Regulation of the Generated Current using a PID Control . . . 38

7 Thermal Characterization of the Setup and Integration of the 2S Module 41
- 7.1 Thermal Characterization of the Inserts . . . 41
- 7.2 Thermal Contact between Bridge and Insert as a Function of the Torque . . . 43
- 7.3 Integration of the 2S Module on the Cooling Structure . . . 44
  - 7.3.1 Measurement of the Noise . . . 45

8 Thermal Measurements with the 2S Module 49
- 8.1 Possible Scenarios for the Operation at the HL-LHC . . . 49
- 8.2 Measurements with Realistic Power Consumption for Different Scenarios at the Nominal CO_2 Temperature . . . 51
  - 8.2.1 Analysis of the Thermal Interfaces . . . 54

8.2.2 Comparison with a Thermal Simulation 59
8.3 Thermal Runaway for the Ultimate at 800V Scenario 60
8.3.1 General Concept of the Measurement 61
8.3.2 Measurement of the Thermal Runaway 62
8.3.3 Comparison with a Thermal Simulation 67

9 Summary **71**

Bibliography **73**

A Cooling System, Module Cooling Box and Cooling Structure **77**

B Characterization of Temperature Sensors **79**

C Measurement of the Noise **80**

1 Introduction

The discovery of the Higgs boson [1] at the Large Hadron Collider (LHC) at CERN, the European Organization of Nuclear Research, near Geneva in 2012 has been a great success for the Standard Model of Particle Physics. At the LHC the interactions of matter are investigated by accelerating two beams of protons almost to the speed of light and colliding them with each other at center-of-mass energies of up to 13.6 TeV, making the LHC the most powerful particle accelerator to date [2]. The decay products of the interactions are studied by placing four main detectors around the collision points of the two particle beams, with the CMS (Compact Muon Solenoid) detector representing one of them. The CMS detector is composed of several subdetectors to identify the particles based on their measured properties [3].

Since its start of operation the LHC has already exceeded its design value by reaching an instantaneous luminosity of $2.0 \times 10^{34}\,\mathrm{cm}^{-2}\mathrm{s}^{-1}$ in 2018. To increase the precision of the measurement of several Standard Model processes as well as to search for physics beyond the Standard Model the LHC will receive its next major upgrade, the High-Luminosity LHC (HL-LHC), after the end of Run 3 in 2025. The HL-LHC is expected to reach peak instantaneous luminosities of $5.0 - 7.5 \times 10^{34}\,\mathrm{cm}^{-2}\mathrm{s}^{-1}$ with an estimated integrated luminosity of $300\,\mathrm{fb}^{-1}$ per year. At its scheduled end of lifetime in 2041 the HL-LHC is expected to have delivered an integrated luminosity of $3000\,\mathrm{fb}^{-1}$. In a scenario of maximal performance a total integrated luminosity of $4000\,\mathrm{fb}^{-1}$ could even be possible [4].

As part of the HL-LHC upgrade the CMS detector needs to be upgraded as well to cope with the new operating conditions of the HL-LHC. This is referred to as the CMS Phase-2 upgrade. Within this upgrade the complete tracking system of the CMS detector will be replaced. A part of the new Phase-2 tracker will be composed of so-called 2S modules that represent a new type of silicon module. The main feature of the 2S module are two silicon strip sensors that are stacked on top of each other. By correlating the measured hits in both sensor layers particle tracks can be reconstructed and the transverse momentum of the particles determined. For particles with a high transverse momentum this information will be sent to the Level-1 trigger, which marks the first time that tracking information is included in the first stage of the event selection process at CMS [4].

The challenging conditions of the HL-LHC include the operation of the 2S modules at high radiation levels. After irradiation the silicon sensors exhibit a leakage current that is exponentially dependent on the sensor temperature. For the Phase-2 tracker a new cooling system based on evaporative CO_2 cooling will be installed. In a case of unstable cooling it is possible that the 2S modules enter an uncontrolled self-heating loop called thermal runaway which leaves the modules unusable in the detector. Therefore the longevity of the tracking detector is strongly influenced by the performance of the cooling system. To ensure a reliable and successful operation of the 2S modules until the planned end of lifetime it is of utmost importance that the nominal operating temperature of $-33\,^{\circ}\mathrm{C}$ provides enough margin to the expected point of thermal runaway. Thus it is crucial to characterize the thermal properties of the 2S module and test the performance of the cooling system. This includes the assessment of the CO_2 temperature at which the thermal runaway would occur.

Depending on the location inside the detector the 2S modules will be mounted onto different cooling and support structures. In the endcap of the Phase-2 tracker the 2S modules will be mounted on the so-called Tracker Endcap Double-Disks (TEDD). In the TEDD region the 2S modules themselves will have six cooling points at which they will be mounted onto aluminum inserts that provide the thermal interface to the cooling pipe. Within this thesis thermal measurements of a 2S module are carried out on a small version of such a TEDD cooling structure. For this the cooling structure is connected to a CO_2 cooling system that is based on the same principle as the future cooling system in the detector. To minimize the heat exchange with the ambient the cooling structure is placed in a module cooling box that is actively cooled by an external chiller. By setting the ambient temperature to the mean sensor temperature of the 2S module a thermal equilibrium can be achieved between the sensors and the ambient.

Since the 2S module used for this thesis is not irradiated a setup has been developed that allows the emulation of the expected leakage current of irradiated sensors by illuminating them with light emitted by LEDs. For the operation at the HL-LHC three scenarios are under investigation: the nominal, Ultimate@600V, and Ultimate@800V scenario. The latter denotes the case of maximal performance that would lead to the highest expected power consumption for the silicon sensors of the 2S module. The adjustment of the leakage current in this setup via the LEDs allows to emulate the power consumption of the 2S modules according to the expected values of each scenario. By gluing small temperature sensors onto several components of the 2S module including the silicon sensors the temperature distribution on the 2S module can be measured and analyzed. Within this thesis the thermal properties of the 2S module have been assessed for all three scenarios at the nominal CO_2 temperature of $-33\,^{\circ}\mathrm{C}$. Additionally a method has been established that enabled the measurement of the thermal runaway for the Ultimate@800V scenario within the given setup.

This thesis starts with a detailed introduction to the LHC and the current CMS detector in Chapter 2, followed by a description of the HL-LHC and the CMS Phase-2 upgrade, including the working principle of the cooling system, in Chapter 3. Subsequently the 2S module with focus on the thermal design and the power consumption will be introduced in Chapter 4. The experimental setup as well as the preparatory measurements are presented in Chapter 5 and 6. The thermal characterization of the setup and the integration of the 2S module onto the cooling structure are discussed in Chapter 7. The thermal measurements of the three scenarios at the nominal operating temperature as well as the measurement of the thermal runaway for the Ultimate@800V scenario are explained and analyzed in Chapter 8. Finally a summary is given in Chapter 9.

2 The LHC and the CMS Experiment

The Large Hadron Collider (LHC) is the world's largest and most powerful particle accelerator to date. It is located at CERN, the European Organization of Nuclear Research, near Geneva in Switzerland. The LHC is a circular synchrotron that accelerates mainly protons and collides them with each other to study the fundamental structure of matter by analyzing the particles that arise from these collisions [2]. This is achieved by the installation of four main experiments at the crossing points of the particle beams: ALICE (A Large Ion Collider Experiment) [5], ATLAS (A Toroidal LHC ApparatuS) [6], LHCb (Large Hadron Collider beauty) [7] and CMS (Compact Muon Solenoid) [3]. Both ATLAS and CMS are general purpose detectors that aim to perform precision measurements of a wide range of Standard Model processes as well as to look for new particles beyond the Standard Model, such as supersymmetry. The detectors have similarities but differ in design and technical implementation. ALICE and LHCb are covering more specific fields of particle physics. While ALICE is specialized in heavy ion collisions to study the quark-gluon plasma, LHCb has its focus on particle interactions involving bottom quarks to investigate the matter-antimatter asymmetry. The following sections provide a description of the LHC and the CMS experiment.

2.1 The Large Hadron Collider

The LHC was commissioned in 2008 and re-uses the 26.7 km long tunnel around 100 m underground between the Jura Mountains and Lake Geneva that was previously built for the Large Electron-Positron (LEP) Collider. In the tunnel two counter-rotating beams of protons or lead nuclei are accelerated almost to the speed of light and collide with each other at four crossing points [2]. In general pp, PbPb and pPb collisions are possible. The following descriptions focus on protons, but are applicable also to lead ions.

The proton beams are arranged in bunches. Each beam consists of 2808 bunches with approximately 10^{11} protons per bunch. The bunch crossing frequency is at 40 MHz which corresponds to a bunch spacing of 25 ns. The number of particle interactions during a single bunch crossing is called pileup [8]. Three other parameters important for the characterization of a particle accelerator are the center-of-mass energy and the instantaneous and integrated luminosity. The center-of-mass energy $\sqrt{s}$ is considered as the total energy of the particle collision while the instantaneous luminosity measures the rate of potential particle collisions per unit area and time. The integrated luminosity describes the rate of potential particle collisions per unit area for a given time interval. Thus the integrated luminosity is used as a quantity that expresses the amount of data collected by a detector.

Before traversing the LHC, the protons are passing through a chain of pre-accelerators with each machine having an increasingly higher energy. Figure 2.1 shows an overview of the accelerator complex at CERN. First the protons are extracted from hydrogen gas before the acceleration process starts at the LINAC 2 (LINear ACcelerator). There they are accelerated to 50 MeV before being injected into the PS Booster (PSB), where they are accelerated to 1.4 GeV. Then the protons reach the second circular accelerator, the Proton Synchrotron (PS), and are accelerated to 25 GeV. Before entering the LHC, the protons are fed into the Super Proton Synchrotron (SPS), accelerated to 450 GeV and finally transferred to the LHC [8].

The accelerator ring of the LHC can be divided into eight sections, each consisting of an arc and a longer straighter section. The arc section includes superconducting dipole mag-

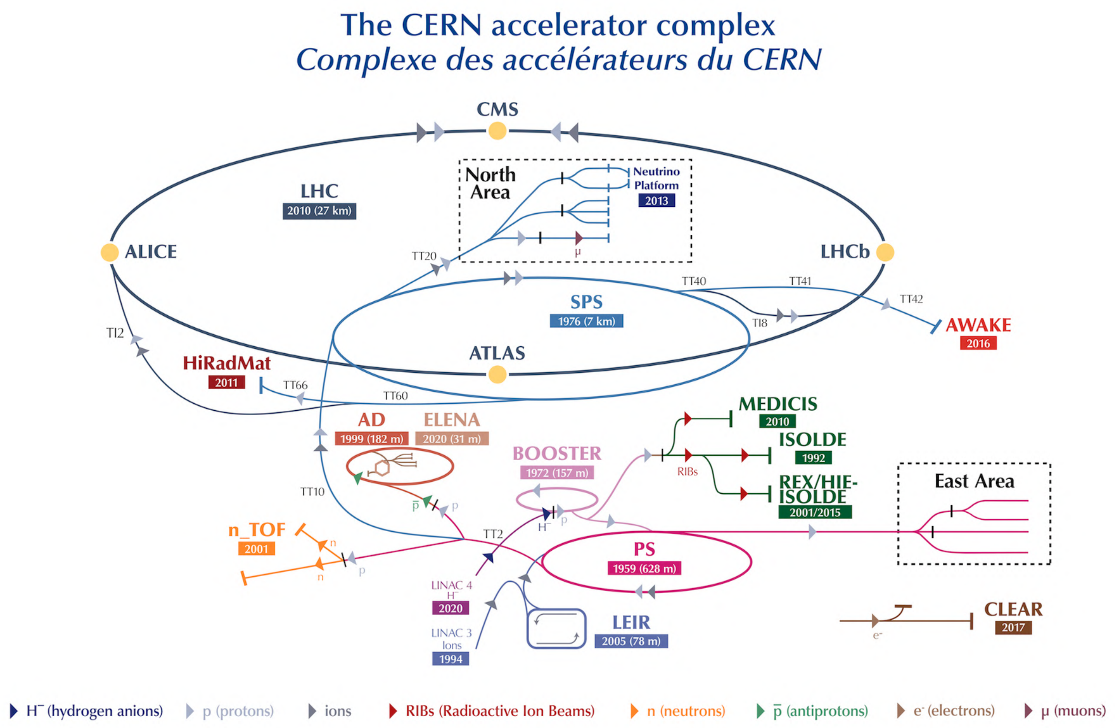

Figure 2.1: Overview of the LHC and the accelerator complex at CERN, modified from Ref. [9].

nets that are used to bend the particle beam in order to maintain the curved trajectory, whereas quadrupole magnets are installed at the collision points to focus the beam to the smallest possible diameter before the two beams are crossing. The long straight sections are composed of so-called cavities which are electromagnetic resonators that accelerate the particle beam up to the maximum energy reachable at the LHC [8].

The LHC was originally designed to reach a center-of-mass energy of $\sqrt{s} = 14\,\text{TeV}$ with an instantaneous luminosity of $1.0 \times 10^{34}\,\text{cm}^{-2}\text{s}^{-1}$. Since the start of the operation in 2009 it has already exceeded this value with a peak instantaneous luminosity of $2.0 \times 10^{34}\,\text{cm}^{-2}\text{s}^{-1}$ in 2018. During the last running period from 2015 to 2018, which is referred to as Run 2, the CMS experiment has collected data at center-of-mass energies of $\sqrt{s} = 7\,\text{TeV}$, $8\,\text{TeV}$ and $13\,\text{TeV}$ that correspond to an integrated luminosity of $178\,\text{fb}^{-1}$ collectively [10]. Run 2 was followed by Long Shutdown 2 (LS2) during which the LHC machine received several repairs and updates. The present running period, referred to as Run 3, has started in 2022 with the aim of reaching $300\,\text{fb}^{-1}$ at its end in 2025. So far the CMS detector has collected around $67\,\text{fb}^{-1}$ of pp collision data at a center-of-mass energy of $\sqrt{s} = 13.6\,\text{TeV}$ during the ongoing Run 3 with a peak instantaneous luminosity of $2.2 \times 10^{34}\,\text{cm}^{-2}\text{s}^{-1}$. In Run 3 up to now the pileup was on average in the order of 50 [10].

2.2 The Compact Muon Solenoid Experiment

The CMS experiment is one of the four main experiments at the LHC, installed around 100 m undergound at Point 5 near the village Cessy in France. It is designed as a general-purpose detector consisting of several subdetector systems that are arranged in cylindrical layers around the collision point and the beam pipe. This central part is also known as

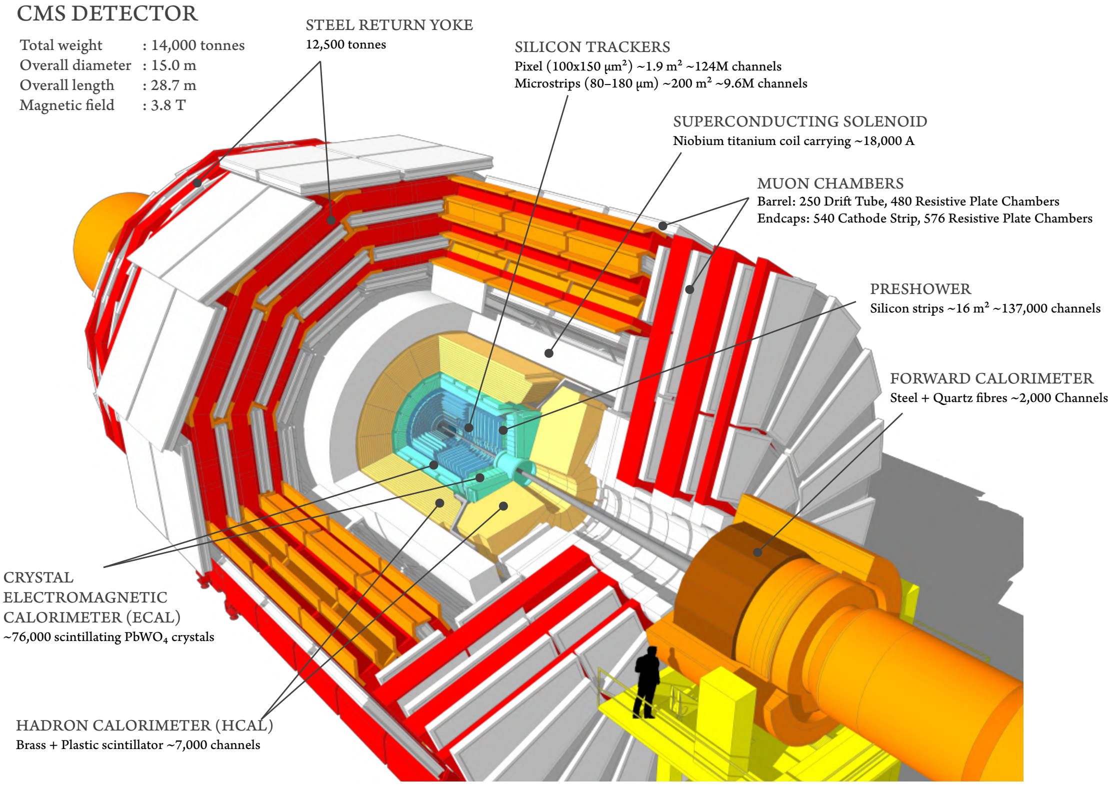

Figure 2.2: Sketch of the CMS detector with an overview of its subdetectors [11].

the barrel. It is closed at each side with the so-called endcaps that are also composed of several detector layers orientated perpendicular to the beam axis. Figure 2.2 shows an overview of the detector architecture with its subdetectors. Overall the CMS detector has a length of 28.7 m and a diameter of 15.0 m with a weight of 14 000 t. A central piece of the detector is the solenoid magnet that is also giving the detector its name [3].
The CMS Collaboration adapted the following coordinate system: the center is at the collision point inside the experiment, the x-axis is pointing to the direction of the center of the LHC accelerator ring while the y-axis is going vertically up and the z-axis is orientated along the beam axis in the counterclockwise direction. Additionally the radial coordinate r and the azimuthal angle ϕ are defined in the x-y plane with ϕ starting at the x-axis. The polar angle θ is defined in the r-z plane and measured from the z-axis, while the pseudorapidity η can be calculated from $\eta = -\ln[\tan(\theta/2)]$ [3].

The Pixel Detector

The pixel detector is the innermost subdetector installed close to the beam pipeline and therefore exposed to the highest radiation levels within the detector. As a consequence the original pixel detector was replaced and upgraded during the year-end technical stop 2016/2017 with the CMS Phase-1 pixel detector which is in operation since. The detector is subdivided into two parts: the barrel pixel detector (BPIX) with four concentric layers and the forward pixel detector (FPIX) that is composed of six disks, three disks positioned at each side of the BPIX as an endcap. The BPIX and the FPIX are both populated with modules that have silicon sensors with 160 × 416 pixels connected to 16 readout chips. Figure 2.3 shows an overview of the layout of the current tracking detector. The modules

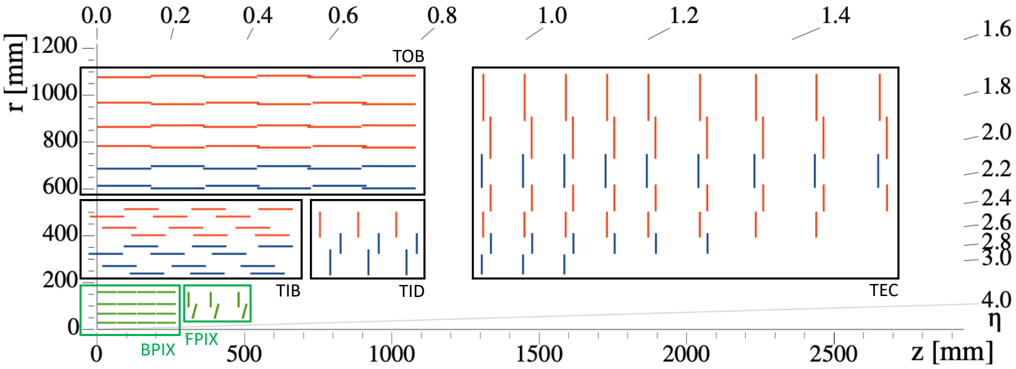

Figure 2.3: Overview of one quarter of the current layout of the tracking system. The modules of the Phase-1 pixel detector are shown in green, while the modules of the silicon strip detector are depicted in blue and red, respectively. Modified from Ref. [4].

of the Phase-1 pixel detector are depicted in green. In total the pixel detector contains 1856 modules that yield an area of approximately 1.9 m^2 covered by silicon. With a number of roughly 124 million channels the Phase-1 pixel detector provides the foundation for excellent tracking and vertex reconstruction [12].

The Silicon Strip Tracker

The pixel detector is surrounded by the silicon strip detector as the second part of the tracking system. It is subdivided into four sections: the Tracker Inner Barrel (TIB), the Tracker Inner Discs (TID) and the Tracker Outer Barrel (TOB) forming the barrel part of the detector and the Tracker EndCaps (TEC) as a closure on both sides of the barrel. The strip detector uses single-sided micro-strip silicon sensors with a size of about $10 \times 10\,\mathrm{cm}^2$. Throughout the strip detector overall 29 different module designs are used. As a consequence the individual sensor specifications with regard to the sensor thickness and strip pitch vary depending on the module location in the detector, for example there are modules whose silicon sensors are aligned back-to-back to each other with a rotation angle of 100 mrad, whereas most of the modules are composed of a single strip sensor. The double-sided modules enable the measurement of a second coordinate of a particle track. The four subdetectors are indicated in the layout overview of one quarter of the whole tracking detector in Figure 2.3, where single-sided modules are marked in red and double-sided modules in blue. As a whole the tracking detector has a diameter of 2.5 m, a length of 5.8 m and covers a pseudorapidity of $|\eta| < 2.5$. In total 15 148 modules are integrated in the strip tracker covering an area of 198 m^2 with about 9.3 million strips that allow a precise measurement of the particle trajectories.

The Electromagnetic Calorimeter

The next layer, the electromagnetic calorimeter (ECAL), starts at a radius of 1.3 m and consists of 68 524 lead tungstate crystals ($\mathrm{PbWO_4}$) that are distributed over the barrel and the two endcaps. The main purpose of the calorimeters is to measure the energy of the emerging particles. In the ECAL particles that interact via the electromagnetic force mainly electrons and photons are absorbed by the crystals that convert the deposited energy by scintillation into photons. The photons are then detected by avalanche photodiodes (APDs) in the barrel or vacuum phototriodes (VPTs) in the endcaps. The segmentation of the ECAL into a high number of small crystals allows an energy measurement with a high spatial resolution.

The Hadron Calorimeter

Particles like neutrons or pions that interact via the strong interaction are fully detected in the hadronic calorimeter (HCAL) that sits behind the ECAL, starting at a radius of 1.8 m. It is a so-called sampling calorimeter built out of alternating layers of brass absorber plates and plastic scintillators. In total about 70 000 scintillator tiles are installed in the HCAL that are read out by silicon photomultipliers. When penetrating the brass plates the hadrons scatter inelastically and lose their energy producing hadronic showers that are measured in the subsequent scintillation layer.

The Solenoid Magnet

The solenoid magnet of the CMS detector surrounds the tracking system and the calorimeters with a length of 12.5 m, a diameter of 6 m, and generates a magnetic field of 3.8 T. The Lorentz force bends the trajectories of the charged particles, forcing them on a curved trajectory so that by measuring the radius and the direction of the curvature the momentum and charge of the particle can be determined. The magnet consists of superconducting NbTi and thus operates at a temperature of 4.5 K. Additionally the magnetic field is returned through an iron return yoke that is installed outside of the magnet and partly embeds the muon system. The iron yoke itself weighs 10 000 t, which makes the magnet system by far the heaviest part of the CMS detector.

The Muon System

The muon system is using four different types of gas detectors that are partly enclosed in the layers of the iron return yoke: the Drift Tubes (DT), the Cathode Strip Chambers (CSC), the Resistive Plate Chambers (RPC) and the Gas Electron Multipliers (GEM). The GEMs are the newest part of the muon system. The installation of the first station GE1/1 in the endcaps of the CMS detector has been finished in LS2. Since the iron yoke is also magnetized the momentum and charge of the muons can also be measured in the muon system with the muon tracks being bent in the opposite direction with respect to the tracker. Altogether this leads to a precise muon measurement being a central part of the CMS detector, as indicated by its name. The muon system is the last and outermost detector layer of the CMS experiment.

The Trigger System

Another important part of the CMS experiment is the trigger system. At a bunch crossing frequency of 40 MHz and a pileup of 50 it is not possible to store and process the data of all events, therefore a trigger system is employed in order to reduce the data rate and filter out the interesting events. CMS implemented a trigger system based on two stages: as a first step the hardware-based Level-1 (L1) Trigger is applied using the information from the calorimeters and muon system to reduce the output rate of the data to 100 kHz. As a second stage the software-based High-Level Trigger (HLT) further reduces the data rate to 1 kHz by performing an offline analysis using the complete data of all subsystems.

3 The High Luminosity LHC and the Phase-2 Upgrade

During the previous shutdowns the LHC has been constantly improved to reach its design values. To reach its full potential the next major upgrade, the High-Luminosity LHC (HL-LHC), will be installed after Run 3 in the Long Shutdown 3 (LS3), beginning in 2025 [13]. This also implies necessary upgrades for the detectors, which are referred to as the CMS Phase-2 Upgrade [4]. An overview of the upgrades foreseen for the HL-LHC and the CMS detector will be given in the next sections.

3.1 The High Luminosity LHC

Starting in 2029 after LS3 the HL-LHC is expected to reach a peak instantaneous luminosity of $5.0 - 7.5 \times 10^{34}\,\mathrm{cm}^{-2}\mathrm{s}^{-1}$ and an estimated integrated luminosity of $300\,\mathrm{fb}^{-1}$ per year, meaning that the LHC will have collected data corresponding to an integrated luminosity of $3000\,\mathrm{fb}^{-1}$ by its scheduled end of lifetime in 2041. In an ultimate scenario a maximal performance of $4000\,\mathrm{fb}^{-1}$ could even be possible. The pileup is estimated to reach a value of 140 to 200 [4]. To achieve this the main upgrades to the LHC machine contain new superconducting quadrupole magnets, the replacement of several beam-bending dipole magnets and new so-called crab cavities to increase the interaction probability at the collision points [8].

3.2 The CMS Phase-2 Upgrade

The increased luminosity of the HL-LHC entails increased particle rates, higher radiation levels and larger pileup. To cope with the challenging environment of the HL-LHC several subdetectors of the CMS experiment need to be improved or replaced as part of the CMS Phase-2 Upgrade. Since this thesis contributes to the new Phase-2 Outer Tracker of CMS, the following section will give a detailed portrayal of this specific upgrade, including the foreseen cooling system.

3.2.1 The CMS Phase-2 Tracker

The central features of the CMS Phase-2 tracker within the framework of the upgrade include increased radiation hardness to withstand the higher radiation levels, a higher detector granularity to keep the channel occupancy at the minimum level below 1 % for a good tracking performance as with the present tracker in Run 3 and the contribution of tracking information to the Level-1 (L1) trigger to cope with the increased amount of data. In order to fulfill these requirements the whole silicon tracking detector will be replaced with new silicon modules that have been developed during the last years. The Phase-2 tracker will be divided into the Inner Tracker (IT) and the Outer Tracker (OT). The IT will be equipped with silicon pixel modules, while two module types have been developed for the OT, the so-called 2S module, consisting of two silicon strip sensors, and the so-called PS module, which is composed of a silicon strip and a macro-pixel sensor. The key feature of these new module types for the OT is that the two silicon sensors of each module are stacked on top of each other, which enables the measurement of the particles' momentum by reconstructing the hit pattern of both sensors. As a result this information is used as a contribution to the L1 trigger in order to help reduce the amount of data that has to be

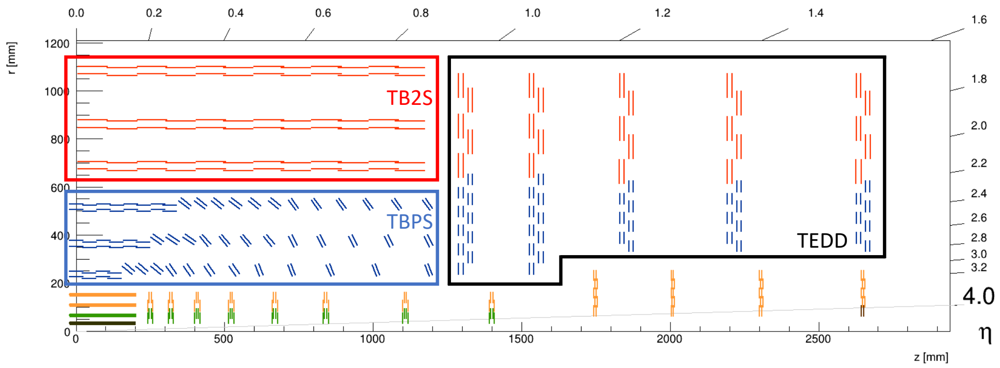

Figure 3.1: Sketched overview of one quarter of the new CMS Phase-2 tracker. The pixel modules of the Inner Tracker are shown in yellow and green, whereas the PS modules of the Outer Tracker are depicted in blue and the 2S modules in red. The black modules in the Inner Tracker mark modules that will be equipped with 3D sensors, while the outermost modules in brown will be used especially for the measurement of the luminosity. The Outer Tracker is subdivided into three regions: TBPS, TB2S and the TEDD, as marked in the Figure. Modified from Ref. [14].

processed. More information about this, also known as the p_T module concept, is provided in Section 4.2.

Figure 3.1 shows an overview of one quarter of the new Phase-2 tracker. The PS modules are indicated in blue, while the 2S modules are shown in red. The modules of the IT with two readout chips are marked in green and with four readout chips in yellow. In general the detector layout of the OT can be divided into two parts, the barrel in the center and the endcaps on each side. The barrel is furthermore subdivided into two sections, the Tracker Barrel which only contains 2S modules (TB2S) mounted on ladders parallel to the beam pipe, and the Tracker Barrel which is only composed of PS modules (TBPS) and located closer to the beam pipe. The TBPS itself has a region where the PS modules are mounted on "planks" parallel to the beam pipe and a second region with tilted PS modules to allow particles emerging from the interaction point to cross the modules perpendicular to their surface. The endcap region is known as the Tracker Endcap Double-Disks (TEDD) and is composed of five double-disks on each detector side that feature PS modules at smaller radii as well as 2S modules at larger radii. In total a number of 5616 PS modules and 7680 2S modules will be installed in the Phase-2 OT. The maximum expected fluence for the PS modules in the OT in case of the nominal scenario with an expected integrated luminosity of $3000\,\mathrm{fb}^{-1}$ has been simulated to reach $9.6 \times 10^{14}\,\mathrm{n_{eq}/cm^2}$, while a maximum value of $3.0 \times 10^{14}\,\mathrm{n_{eq}/cm^2}$ has been estimated for the 2S modules [4]. Here and in the following the fluence is expressed in 1 MeV equivalent neutron fluence per cm^2. The Phase-2 tracker will also cover an extended range in pseudorapidity of $|\eta| < 4$ compared to the present tracking system as well as a higher granularity and an improved radiation tolerance [4].

3.3 Cooling of the Phase-2 Tracker

The challenging operation conditions of the HL-LHC including the higher radiation levels and the expected readout rate lead to an increase in the overall detector power. For the Phase-2 OT the total dissipated power has been estimated to be about 100 kW [4]. As well as removing this heat load, the temperature of the silicon sensors of the 2S modules has to be kept at around $-20\,^\circ\mathrm{C}$ or lower in order to sustain a low leakage current. This is necessary since the radiation damage of silicon sensors induces a temperature dependent leakage current and thus power consumption that could lead to a thermal runaway of the modules [15]. A more detailed explanation of this effect will follow in Section 4.4.3. Such low sensor temperatures also help to avoid reverse annealing which is an effect that mainly occurs at high temperatures and can reinforce the radiation damage in the silicon sensors [15]. Consequently a cooling system has to be designed that is capable of fulfilling these requirements and provides stable cooling conditions throughout the whole detector operation with a low contribution to the detector material budget.

3.3.1 The 2PACL Principle

The present CMS strip tracker uses a liquid cooling system based on C_6F_{14}. With this cooling system temperatures down to −25 °C can be achieved. A flow rate of 1 l/s is needed to keep the temperature increase of the coolant within a cooling loop below 2 °C. The used aluminum cooling pipes have a diameter in the range of 6 mm [3].

For the Phase-2 OT and IT a common cooling system based on the 2-Phase Accumulator Controlled Loop (2PACL) [16] principle has been selected with two-phase CO_2 as a coolant. Such a cooling system is successfully operated at the LHCb VELO detector [17] since 2008 and has also been employed in the CMS Phase-1 pixel detector [12, 18] in 2017. The basic principle of the 2PACL method is the removal of heat by evaporating the liquid state of the circulating coolant. As a result the cooling lines contain a mixture of liquid and vapor. The evaporation occurs at a constant temperature and pressure. The friction inside the cooling pipes leads to a pressure decrease towards the outlet so that a small temperature decrease in the order of 2 °C occurs along the cooling lines. Overall this leaves the temperature of the boiling CO_2 as the central parameter that has to be controlled in a 2PACL system. This is realized by using an accumulator vessel that continually holds a mixture of liquid and vapor while heating and cooling regulates its pressure.

3.3.2 CO_2 as a Coolant

The use of two-phase CO_2 as a coolant offers a lot of advantages compared to mono-phase cooling systems. Two-phase CO_2 exists along its vapor pressure curve at reasonable conditions over a large temperature range from for example 12 bar at −35 °C to 57 bar at 20 °C and can consequently provide stable cooling for a wide range of temperatures. Furthermore evaporative CO_2 has a high latent heat of vaporization of about 436 kJ/kg at −35 °C so that in general a smaller mass flow can achieve the removal of the same heat load compared to mono-phase refrigerants like C_6F_{14} [19, 20]. Additionally the low viscosity of two-phase CO_2 allows the use of thin cooling pipes with a diameter in the order of a few millimeters.

The heat transfer at the interface of two materials is linearly dependent on the heat transfer coefficient (htc). It is defined as the proportionality constant h between the heat flux $\dot{Q}$ and the temperature difference ΔT:

$$\dot{Q} = h \cdot A \cdot \Delta T \tag{3.1}$$

with the contact surface A and therefore given in units of $\mathrm{W/m^2/K}$ [21]. The heat transfer between the materials improves with higher htc values. For the heat transfer between the inner wall of the cooling pipe and the boiling CO_2 with a temperature of −30 °C the htc value can be expected in the order of $5\,\mathrm{kW/m^2/K}$ to $10\,\mathrm{kW/m^2/K}$ [20]. A low vapor quality, which is defined as the fraction of gas in the liquid/vapor mixture, in the order of maximum 0.3 to 0.5, depending on the heat load, is targeted to achieve a high htc from the cooling pipe to the coolant fluid. Lastly the radiation hardness and the low cost of CO_2 as well as the lower environmental impact additionally contribute to the advantages of CO_2 as a suitable coolant for the application in a cooling system of a tracking detector. The design value for the operation in the Phase-2 OT is a CO_2 temperature of $-35\,°C$. The expected pressure drops along the cooling pipe are small compared to the absolute pressure, therefore a maximum CO_2 temperature of $-33\,°C$ is expected [4]. Currently the estimated CO_2 mass flows in the TEDD are in the range of 1.6 to 1.8 g/s [22], while the inner diameter of the cooling pipes are foreseen to be either 2.20 or 2.40 mm depending on the position in the endcap of the detector [23].

4 The 2S Module

The following sections will give a description of the design of the 2S module, the p_T module concept as the main feature of the 2S module as well as the composition of the power consumption of the 2S module. Furthermore a more detailed explanation of the cooling and the thermal design with a focus on the effect of the thermal runaway will follow.

4.1 Description of the 2S Module Design

The 2S module is one of two module types that have been developed for the CMS Phase-2 OT. The central part of the 2S module are two n-in-p doped silicon strip sensors with a size of about $10 \times 10\,\mathrm{cm}^2$ and an active thickness of $290\,\mu\mathrm{m}$ that are closely stacked on top of each other. Each silicon sensor is divided into two rows of 1016 AC-coupled micro-strips with a length of 5 cm and a pitch of $90\,\mu\mathrm{m}$ [24]. The rows of the strips are orientated in such a way that, when stacking the two sensors above each other, the strips of the top and the bottom sensor are on top of each other in the same overall orientation. Figure 4.1 shows a CAD drawing of the 2S module on the left as well as a CAD drawing with an exploded view on the right.

For unirradiated silicon sensors a depletion voltage of around $-300\,\mathrm{V}$ is necessary, which will be applied to the sensor backplane since the strips themselves are connected to the ground potential. For irradiated sensors the depletion voltage will increase to $-600\,\mathrm{V}$ or higher. In the following absolute values will be used to describe the depletion voltage.

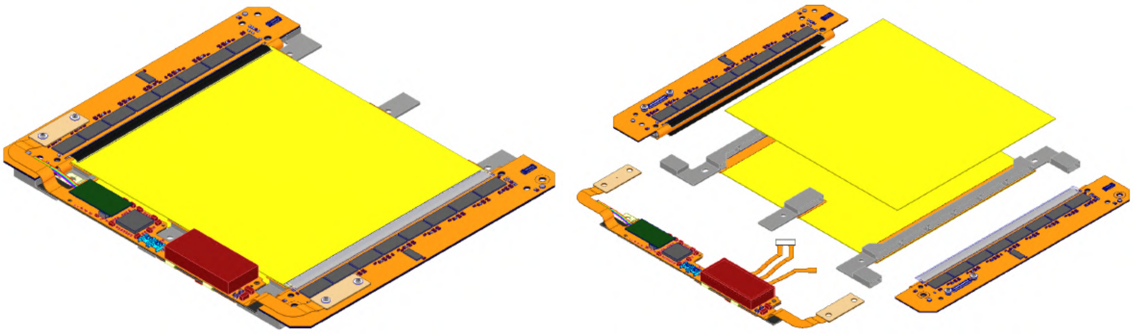

Figure 4.1: A CAD drawing of the 2S module on the left and a CAD drawing with an exploded view of the 2S module on the right [25].

The micro-strips are read out by two front-end hybrids (FEHs) that are each equipped with eight CMS Binary Chips (CBCs) [26] and one Concentrator Integrated Circuit (CIC) [27]. Each FEH reads out one half of the sensor sandwich, meaning that each CBC channel is connected to 127 strips of the top and bottom sensor, respectively, via wirebonds. In total one CBC is reading out 254 strips and one FEH thus 2032 strips. The data of the eight CBCs is then sent to the CIC which merges the data and further transfers them to the service hybrid (SEH). The SEH sits between the FEHs on one side of the module. Its main tasks are to supply the power to the module electronics, the readout of the module and the communication with the back-end. The essential components therefore are the Low-power Gigabit Transceiver (LpGBT) [28], the Versatile TRansceiver plus (VTRx+) [29] and two DC-DC converters [30]. The LpGBT receives the data from both CICs, transmits them to the VTRx+ and distributes signals like the clock and trigger received from the VTRx+ to the FEHs. The VTRx+ converts the received data signals into an optical signal and transmits it via an optical fiber to the back-end as well as converting received optical signals into electrical for the LpGBT. The two DC-DC converters on the SEH supply the necessary power to the module electronics by converting its input voltage of 10.5 V via two stages. The first stage converts the input voltage to 2.55 V that is required by the laser components of the VTRx+ while the second stage transforms the voltage further to 1.25 V which is distributed to all readout chips, the LpGBT and the VTRx+. For the DC-DC converter a total conversion efficiency of 66 % is expected. The SEH also directs the applied high voltage coming from the back-end necessary for the silicon sensors via so-called high-voltage pigtails, that are glued to the backside of each silicon sensor, to the sensors.

The main mechanical structure that holds the two sensors apart are the Aluminum Carbon Fiber (AlCF) spacers or so-called bridges that provide either a spacing of 1.8 mm or 4.0 mm between the two sensor mid planes depending on the foreseen location of the module in the detector. Apart from that each AlCF bridge has a hole that will be used to integrate the module onto its larger support structure in the detector by mounting it with screws to the so-called inserts that serve as an interface between the module and the cooling structure. Lastly the good thermal conductivity of AlCF ensures that the bridges also function as cooling contacts for the module to remove the heat load of the hybrids and the sensors adequately and transport it to the cooling system.

Each module has two long AlCF bridges on opposite sides of the sensor sandwich and one short spacer, also referred to as stump bridge, that sits halfway between the long spacers on one open side of the module. The long spacers provide the mechanical support for the sensor sandwich and the FEHs whereas the short spacer serves as a third support point for the SEH and an additional cooling contact. Some modules, for example all modules that will be installed in the TEDD, will have an additional short spacer on the opposite side of the stump bridge as a sixth cooling contact. The three hybrids are glued to the edges of the bridges.

To isolate the AlCF bridges from the sensor bias voltage that is applied to the backside of the silicon sensors, kapton strips with a thickness of 25 μm are glued to the backside of each sensor at the positions of the AlCF spacers during the assembly process. Long kapton strips are used for the long AlCF bridges at the outer sides of the sensors whereas only short kapton strips are used at the location of the stump bridges.

4.2 General Concept of the p_T Module

A central aspect of the 2S module design is the contribution of information to the L1 trigger based on the measurement of the transverse momentum of the particles, which is also known as the p_T module concept. It is based on the measurement of hit pairs as an indication of a particle track by the two silicon sensors of the 2S module that are closely stacked on top of each other. When a charged particle emerges from the collision point inside the CMS detector its trajectory is bent inside the magnetic field by the Lorentz force. Trajectories from particles that have a higher transverse momentum have a larger radius than trajectories from particles with a low transverse momentum so that low p_T particles have a stronger curved track. When passing through the 2S module, the particles are detected by both silicon sensors and create hits in the silicon strips along their trajectory in the top and bottom sensor. By comparing the hit pattern of the top and bottom sensor information about the particle p_T can be estimated. This works as follows. Based on the hit strip in the bottom sensor an acceptance window of up to 14 strips opens in the top

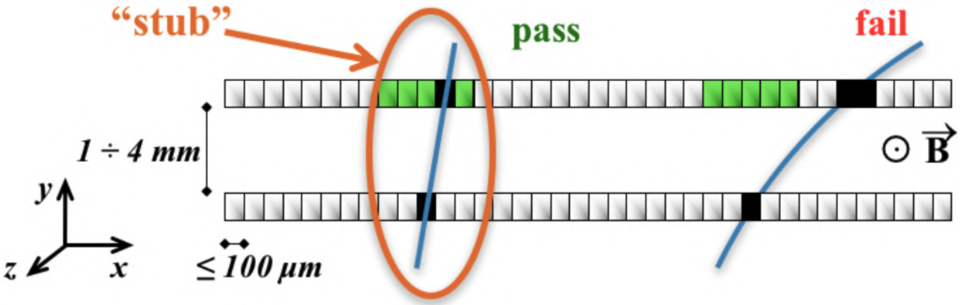

Figure 4.2: Illustration of the p_T module concept, showing a cross section of the strips of the two silicon sensors stacked on top of each other [4]. The measured hits are shown in black whereas the acceptance window based on the hit in the bottom sensor is depicted in green. Two cases are shown: the left track indicates a particle with a high p_T whose measured track is inside the acceptance window and therefore accepted as a stub, whereas the right track indicates a particle with a low p_T whose track is outside the window and therefore does not fulfill the stub criterion.

sensor. If the measured hit in the top sensor was detected inside the acceptance window a so-called stub is generated, otherwise the stub criterion is not fulfilled. A stub corresponds to a track segment that is made from hit clusters in the two layers. Since high p_T particles have a trajectory with a low curvature, a stub equals the measurement of a high p_T particle track. The maximum available acceptance window size corresponds to a p_T-threshold of 2 GeV so that particles with a lower p_T are rejected by the stub finding logic. In Figure 4.2 both of these cases can be seen: on the left a particle track with a high p_T is shown whose hits in the top sensor are inside the acceptance window and therefore accepted as a stub. On the right side a particle with low p_T is shown whose track is outside of the acceptance window and therefore does not fulfill the stub criterion.

The measured stubs are used to reconstruct particle tracks with the track finder that are then sent to the L1 trigger. The L1 trigger can initiate an L1 accept signal for the event by combining the tracks based on the stub data with information from the calorimeters and the muon system. The whole tracking information is readout and transmitted if such a signal has been issued for the event. The size of the acceptance window can also be further reduced to increase the p_T-threshold for the trigger. The stub finding logic itself is implemented in the CBCs that are performing the readout of the silicon strips and apply the stub algorithm to the measured hits. The acquired stub data of each CBC is transmitted further to each CIC, respectively, that combines the stub data of all CBCs and forwards them to the LpGBT. Overall this stub mechanism enables the selection of interesting events based on the measured p_T and thus reduces the amount of data sent out at the bunch crossing rate to the L1 trigger [4].

4.3 Power Consumption of the 2S Module

For the estimation of the power consumption the 2S module can be subdivided into two categories: a low voltage circuit for the three hybrids, including components such as the CBCs, LpGTB etc. and a high voltage circuit composed of the two silicon sensors. In the following a detailed description of the individual contributions to the two categories will be given.

Low Voltage Power

The low voltage power of the 2S module is produced by the components of the two FEHs and the SEH. In particular the eight CBCs and one CIC of the FEH yield an estimated power consumption of 1.3 W leading to a total power of 2.6 W for both FEHs. The contributions of the SEH involve the power consumption of the LpGBT and VTRx+ as well as the dissipated heat load of the DC-DC converters as a result of the estimated efficiency loss. Overall this leads to a value of 2.6 W for the SEH and a total hybrid power of $P_{\text{hybrids}} = 5.2\,\text{W}$. A summary of the individual contributions is given in Table 4.1.

Hybrid	Component	Power in W	Total power in W
Two front-end hybrids	2 × 8 CBCs	2.160	2.568
	2 × 1 CIC	0.408	
Service hybrid	VTRx+	0.206	2.592
	LpGBT	0.358	
	DC-DC converters	2.028	
All three hybrids			5.160

Table 4.1: Overview of the estimated power consumption of the individual components of the 2S module hybrids as well as the total expected power consumption for all three hybrids [31].

High Voltage Power

The high voltage power of the 2S module is generated by the leakage current of the silicon sensors as a product of the reverse bias voltage, U_{bias}, and the leakage current, I_{leakage}:

$$P_{\text{sensor}} = U_{\text{bias}} \cdot I_{\text{leakage}}. \tag{4.1}$$

The leakage current of unirradiated sensors is typically very low. For the silicon sensors of the 2S module with a depletion voltage of 300 V the leakage current is in the order of $10\,\mu\text{A}$, thus the contribution of the heat load of the unirradiated sensors to the total power consumption is negligible. This changes with irradiation of the sensors as the interaction of particles traversing the silicon damages the lattice leaving permanent defects in the crystal structure of the sensor bulk [32]. The appearance of these defects in the space-charge region of the sensor after irradiation has a dominant effect on the thermal generation of charge carriers inside the silicon and consequently induces a temperature dependency on the leakage current of irradiated silicon sensors, which is given by

$$I_{\text{leakage}}(T_{\text{sensor}}) \sim I_0 \cdot \left(\frac{T_{\text{sensor}}}{T_0}\right)^2 \cdot \exp\left(-\frac{\Delta E}{2k_{\text{B}}}\left(\frac{1}{T_{\text{sensor}}} - \frac{1}{T_0}\right)\right). \tag{4.2}$$

Here I_0 denotes the leakage current at a reference temperature of $T_0 = +20\,^\circ\text{C}$, $\Delta E = 1.21\,\text{eV}$ the band gap of silicon at $-20\,^\circ\text{C}$ and k_{B} the Boltzmann constant [15]. In addition to the temperature dependency the rise of the leakage current as a result of the experienced radiation damage is linearly dependent on the fluence Φ for a given volume V

$$\Delta I_{\text{leakage}} = \alpha_{\text{damage}} \cdot \Phi \cdot V_{\text{active}}, \tag{4.3}$$

with the radiation damage constant α_{damage} and $V_{\text{active}} = A_{\text{sensor}} \cdot d_{\text{active}}$ [15]. Altogether the leakage current of an irradiated sensor can be described with

$$I_{\text{leakage}}(T_{\text{sensor}}) = \alpha_{\text{damage}} \cdot V_{\text{active}} \cdot \Phi \cdot \left(\frac{T_{\text{sensor}}}{T_0}\right)^2 \cdot \exp\left(-\frac{\Delta E}{2k_{\text{B}}}\left(\frac{1}{T_{\text{sensor}}} - \frac{1}{T_0}\right)\right), \tag{4.4}$$

which leads to a power consumption of

$$P_{\text{sensor}}(T_{\text{sensor}}) = U_{\text{bias}} \cdot \alpha_{\text{damage}} \cdot V_{\text{active}} \cdot \Phi \cdot \left(\frac{T_{\text{sensor}}}{T_0}\right)^2 \cdot \exp\left(-\frac{\Delta E}{2k_{\text{B}}}\left(\frac{1}{T_{\text{sensor}}} - \frac{1}{T_0}\right)\right) \tag{4.5}$$

for a single sensor. Additionally the change of the charge density in the silicon as a result of the radiation damage requires an increase of the bias voltage to ensure a full depletion of the silicon sensor [15]. This further increases the power consumption of the silicon sensors. Based on this a power of 0.47 W can be estimated for a target sensor temperature of −20 °C with a high voltage of 600 V after 3000 fb^{-1}, which results in 0.94 W for both sensors. A detailed discussion of several possible scenarios will follow in Section 8.1.

Full Module Power

The full power of the 2S module is composed of the low voltage contribution of the three hybrids and the high voltage contribution of the two silicon sensors

$$P_{\text{module}} = P_{\text{hybrids}} + P_{\text{sensor}}\left(T_{\text{sensor}}^{\text{top}}\right) + P_{\text{sensor}}\left(T_{\text{sensor}}^{\text{bottom}}\right), \tag{4.6}$$

with the temperature of the top sensor $T_{\text{sensor}}^{\text{top}}$ and the bottom sensor $T_{\text{sensor}}^{\text{bottom}}$. Based on the estimations above a full module power of

$$P_{\text{module}} = 5.16\,\text{W} + 2 \cdot 0.47\,\text{W} \approx 6.1\,\text{W} \tag{4.7}$$

can be expected after 3000 fb^{-1} with a target sensor temperature of −20 °C and a high voltage of 600 V.

4.4 CO_2 Cooling and Thermal Design

The most important aspect in the thermal design of the 2S module and the cooling system is the ability to effectively remove the heat load of the silicon sensors as well as keeping them at a low temperature during operation while minimizing the contribution to the overall tracker material budget.

4.4.1 Thermal Design of the 2S Module

Within the 2S module the AlCF bridges that are glued to the silicon sensors are responsible for the cooling of both the sensors and the hybrids. The heat load of the sensors will be removed by the parts of the AlCF bridges that are directly glued to the sensors (with the kapton strips in-between), i. e. are mainly the long parts of the bridges and the short edges of the stump bridges. In the right CAD drawing of Figure 4.1 it can be seen that each AlCF bridge has a longer end with a hole that sticks out of the glued sensor sandwich. The holes are the mounting points of the module to the cooling system of the support structure whereas the remaining parts of these bridge edges serve as a gluing point for the three hybrids. The FEHs are only glued to the edges of the two long bridges whereas the SEH is glued to the long bridges on one side of the module as well as to the stump bridge. Thus the stump bridge on the SEH side of the module is in contact with the SEH and the sensors while it mainly serves as an additional cooling contact for the heat flux of the SEH. For modules with an additional sixth cooling contact, this cooling contact does not have contact to any hybrid and thus provides additional cooling to the silicon sensors. This thermal design allows to separate the heat fluxes of the hybrids from the sensors such that they only cross path when entering the cooling system at the mounting points of the bridges, except for the connection of the FEHs to the silicon sensors via the wirebonds. Nevertheless the heat fluxes of the hybrids and the sensors can be approximated as thermally independent. Since some cooling points of the module have contact to three hybrids while for example the sixth point is only glued to the sensors, one cannot assume that the overall heat load of the module is distributed equally among the five or six cooling points.

4.4.2 CO_2 Cooling in the TEDD

Since this thesis entails measurements on a small cooling structure that is built similar to a TEDD disk, the following discussions will focus on the cooling conditions in the TEDD, where all modules will have six cooling contacts. Each disk will be composed of two half disks that are called dee. Figure 4.3 shows a CAD drawing of one TEDD dee in the left that is fully assembled with 2S and PS modules. In the TEDD so-called inserts will provide the thermal interface between the cooling pipe and the cooling points of the module. A CAD drawing of such an insert can be found in the right in Figure 4.3. The inserts have a cylindrical shape and provide a contact surface with a diameter of 8 mm to the cooling contacts of the module. In total there are six different insert types that will be used in the TEDD disks depending on the position of the cooling pipe inside the disks and the location of the module on the disks. They differ mostly in length of the aluminum cylinder while the basis concept still applies to each type.

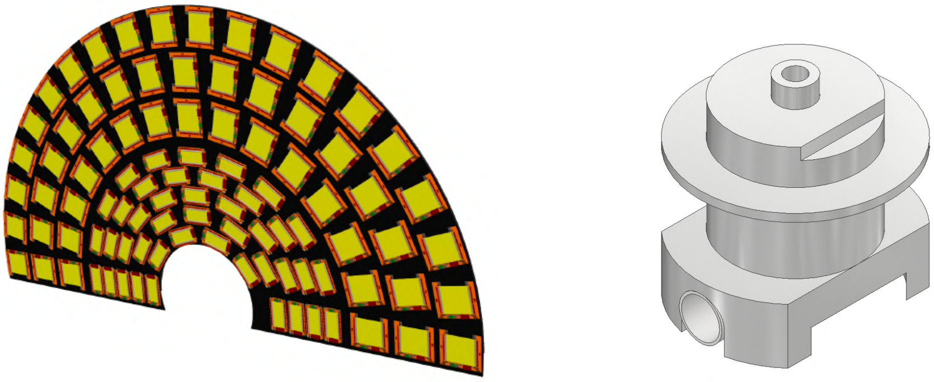

Figure 4.3: Left: CAD drawing of one fully assembled TEDD dee [4]. Right: CAD drawing of an insert that will be used in the TEDD disks as a thermal interface between the 2S modules and the cooling pipe [33].

The inserts enclose the cooling pipe with a so-called foot that extends the length of the contact along the pipe by 4 mm. The contact surface of the inserts to the cooling contacts sticks out of the TEDD disk surface and has a small nipple that allows to mount each cooling contact of the module with a screw and washer to the insert. The inserts are made out of aluminum and are glued to the cooling pipe that consists of stainless steel. With this concept the inserts enable to direct the accumulated heat flux at each cooling contact of the module to the CO_2 cooling system.

4.4.3 Thermal Runaway

The temperature dependent leakage current of the silicon sensors after irradiation induces the effect that in case of an unstable cooling scenario the module enters an uncontrolled self-heating loop called thermal runaway which would cause the module to be unusable for the further operation in the detector.

The appearance of this effect can be explained by the illustration in Figure 4.4. It shows the power of the hybrids with a dashed red line that is approximately stable with temperature, the exponential sensor power with a dotted red line and the full module power with a continuous red line as a result of both. In general the cooling power, P_{cooling}, of the cooling system can be described with

$$P_{\text{cooling}} = \frac{1}{\alpha} \left(T_{\text{sensor}} - T_{\text{cooling}} \right) \tag{4.8}$$

with the thermal resistance α, the sensor temperature T_{sensor} and the coolant temperature T_{cooling}. The thermal resistance is a specific characteristic of the given mechanical structure and expressed in units of K/W. It can be seen that the cooling power is linearly dependent on the thermal resistance of the cooling structure, which is also visible in Figure 4.4. The cooling power for a cooling system with a CO_2 temperature of $-35\,°C$ is given as a blue line while the cooling power for a cooling system with the same thermal resistance but a CO_2 temperature of $-31\,°C$ is depicted with a dashed blue line. A stable working point occurs when the power of the cooling system is equal or greater than the power of the module for a specific sensor temperature:

$$P_{\text{cooling}}(T_{\text{sensor}}) \geq P_{\text{module}}(T_{\text{sensor}}). \tag{4.9}$$

This is the point where the continuous red and blue line intersect in Figure 4.4. In this condition even small fluctuations in the sensor temperature or CO_2 temperature can be compensated so that the working point would be restored. This would not be the case for a higher CO_2 temperature of $-31\,°C$ as it is shown in Figure 4.4. It can be seen that with a higher coolant temperature and the same thermal resistance both lines do not have an intersection point so that a small increase of the sensor temperature would lead to the thermal runaway as the cooling power is not sufficient anymore to remove the heat load of the sensors and the module would enter an uncontrolled self-heating loop. By lowering the coolant temperature a working point could be restored but this is not always technically realizable. This indicates that the performance of the cooling system can also be described with the CO_2 temperature at which the modules will experience the thermal runaway.

Additionally Figure 4.4 illustrates that a small thermal resistance of the cooling structure is necessary to be able to achieve a stable cooling scenario in the first place since the slope is inversely proportional to the thermal resistance. This means that the slope for a cooling structure with a high thermal resistance could be too low so that an intersection with the module power is not possible even when substantially decreasing the coolant temperature. Overall it is crucial that the cooling system provides enough margin to the CO_2 temperature at which the thermal runaway occurs to avoid the appearance of this effect.

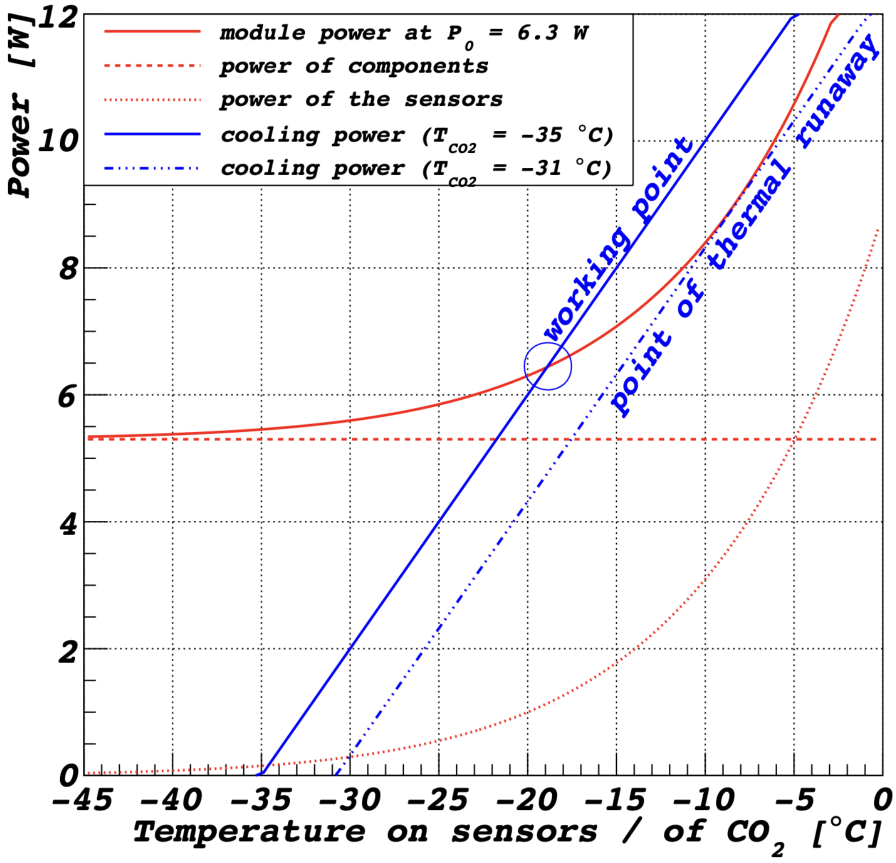

Figure 4.4: Example for the occurrence of the thermal runaway with values that are similar to the expected power and temperature of the 2S module and the cooling system. The power of the hybrids is depicted with a dashed red line, the exponential sensor power with a dotted red line and the full module power with a continuous red line as the sum of both. The cooling power of two cooling systems with the same thermal resistance but a different CO_2 temperature is given, where a CO_2 temperature of -35 °C is shown as a blue line while a CO_2 temperature of -31 °C is depicted with a dashed blue line. The intersection of the solid red and blue line shows the working point for stable cooling conditions. The dashed blue line indicates a cooling system whose cooling power is not sufficient so that the module enters the thermal runaway at a sensor temperature of -8 °C. This figure was taken from Ref. [34].

5 Experimental Setup

Within the scope of this thesis thermal measurements with a 2S module on a small cooling structure have been performed to study the thermal properties of the 2S module in a cooling environment similar to the expected conditions in the detector. A schematic overview of the experimental setup can be found in Figure 5.1.

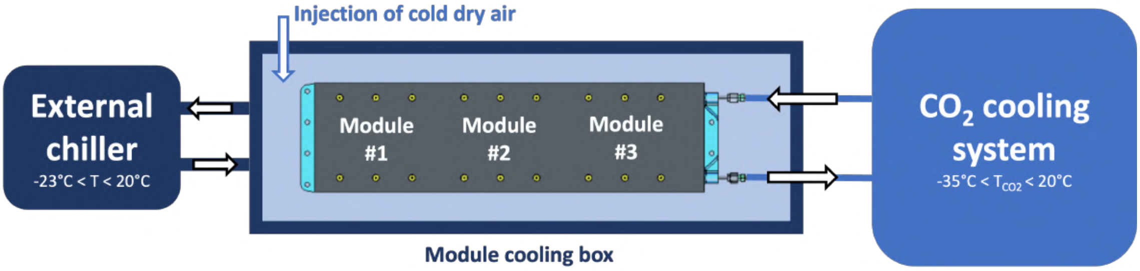

Figure 5.1: Sketched overview of the concept of the experimental setup used in this thesis. The cooling structure can host up to three modules on each side and is directly connected to the CO_2 cooling system. It is placed inside the module cooling box that is actively cooled by an external chiller. The volume of the module cooling box is additionally flushed with cold dry air.

To reconstruct these conditions a cooling system with evaporative CO_2 was used, which has been developed and constructed in the CMS working group of the Physics Institute 1B at RWTH Aachen University and has been available since for thermal measurements in the laboratory [35]. The cooling pipes of the cooling structure are directly connected to the CO_2 cooling system. The cooling structure itself has been constructed by the CMS working group at DESY [36] that will be responsible for the production and commissioning of approximately half of all required TEDD disks for the Phase-2 tracker. To achieve measurements under well defined ambient conditions a module cooling box has been developed and commissioned by Max Rauch in the framework of his PhD thesis at the Physics Institute 1B [34]. The module cooling box is actively cooled by a small external chiller and provides the possibility to mount the cooling structure inside its volume so that measurements in a temperature controlled environment can be carried out while minimizing the heat exchange with the ambient. A more detailed description of the individual components that are a part of the setup will follow in the next sections.

5.1 CO_2 Cooling System

The used CO_2 cooling system is based on the 2PACL method that has been described in Section 3.3. It consists mainly of an expansion vessel, one passive heat exchanger, one actively cooled heat exchanger, a CO_2 pump, a flow meter, two big chillers and a preheating loop. The expansion vessel [37] functions as the accumulator vessel with a mixture of liquid/vapor whose temperature and thus pressure is controlled by one big Huber unistat 815 cooling machine [38]. Consequently the CO_2 temperature inside the cooling system is defined by the pressure inside the accumulator vessel. A second Huber unistat 815 is used to actively cool one heat exchanger that is placed in front of the CO_2 pump [39] to ensure that only liquid CO_2 is transported by the pump. A flow meter [40] is used to measure the mass flow of the liquid CO_2 after the pump. The flow can be regulated in the range of 1 to 2 g/s by changing the rotational frequency of the pump. A pre-heating loop is installed directly before the detector inlet such that a small heat load can be applied to the cooling pipe by using a basic power supply to roughly adjust the vapor quality of the coolant. Additionally the CO_2 cooling system is equipped with several temperature [41] and pressure [42] sensors. The temperature sensors in the cooling system as well as the ones used for the 2S module are read-out by a Keithley Multimeter 2701 [43]. A graphical user interface implemented with a LabView [44] program is used to operate the cooling system. In Figure A.1 in Appendix A a schematic overview of the CO_2 cooling system as well as a picture in Figure A.2 can be found.

5.2 Module Cooling Box

The module cooling box was custom-built by using four ITEM profiles [45] so that one profile can be used as the lid of the box, which can be opened and closed with a handle. The box itself has approximate dimensions of 120 cm × 35 cm × 28 cm. The hollow channels of the ITEM profiles are filled with silicon oil that is used as a coolant. The channels of the three sides forming the box are joined together at the ends and are connected with a flexible tube to the lid of the box and the external chiller. To actively cool the box a Huber ministat 230 [46] is used. The left and right side of the box provide holes to pass all cables and the cooling pipe of the cooling structure through. The cooling structure itself has several mounting points that allow to fix the structure at the bottom of the box at approximately half height of the box. Figure 5.2 shows a picture of the cooling box from above where the cooling structure can be seen mounted in the cooling box. The grooves of the bottom profile inside the box are closed with caps and are constantly filled with dry air so that the dry air is cooled down to the wall temperature and then enters the box through small holes in the caps. Like this the module cooling box can be flushed with cold dry air to control the humidity inside the volume. The air flow into the volume can be regulated with a flow meter [47] between 2 and 100 l/min while the humidity and dew point is measured with a LabKit hygrometer [48] next to the cooling structure at the left side of the box. Additionally the LabKit sensor measures the temperature of the air inside

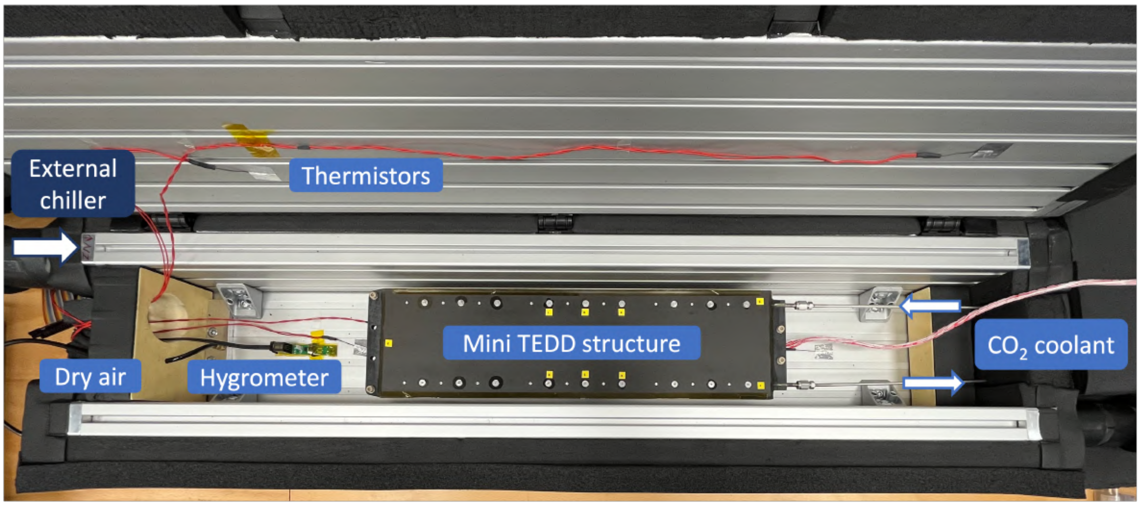

Figure 5.2: Picture of the module cooling box from above. The cooling structure is mounted at half height in the inner volume. The cooling pipes of the structure that are connected to the CO_2 cooling system are guided through the right side of the box. The external chiller is connected at the left side of the box. The CO_2 cooling system and the external chiller are not shown.

the volume of the box. A temperature sensor [41] is placed next to it to provide a second independent measurement of the air temperature. Several other temperature sensors are glued inside the box with aluminum tape to monitor the wall temperatures and the surface temperature of the cooling structure.

The temperature sensors, hygrometer and dry air supply can also be seen in the picture in Figure 5.2. The connecting cooling pipes of the cooling structure to the CO_2 cooling system are guided through the right side of the box. The chiller used to actively cool the outer faces of the box is connected at the left side. Additional pictures of the cooling system and the module cooling box in the laboratory can be found in Appendix A.

With the used external chiller air temperatures of down to $-23\,^{\circ}\mathrm{C}$ can be achieved inside the box, while the actual temperature of the coolant in the chiller is around 2 K lower. The insulation of the outside of the box and the tubes has been improved since its construction and includes two layers of 3 cm thick Armaflex insulation [49].

5.3 Cooling Structure and Inserts

The used cooling structure has been built as a small mock-up of a TEDD disk by the CMS tracker group at DESY and is therefore also referred to as a mini-TEDD structure. It consists of a cooling pipe made out of stainless steel that is embedded in a layer of Airex foam surrounded by a layer of carbon fibre skin on both sides [4]. The open sides of the structure are covered with kapton tape. The mini-TEDD structure can host up to six modules, three on each side, with each position having six cooling contacts. The two middle positions and the inlet, outlet and U-turn of the cooling pipe are outfitted with temperature sensors [50] that have been glued to the inserts/cooling pipe during the production of the cooling structure. Figure 5.3 shows the cooling structure from above mounted in the module cooling box. The positions of the overall 15 temperature sensors inside the structure are numbered according to the assigned numbers depicted in the figure. This numbering will be used throughout this thesis for these temperature sensors. The aluminum inserts that provide the thermal interface and mounting points for the 2S modules are glued to the cool-

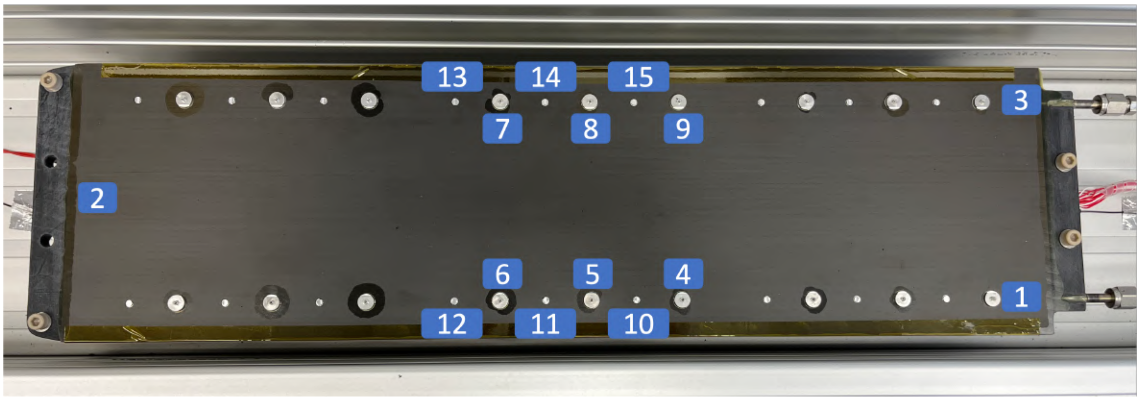

Figure 5.3: Picture of the cooling structure from above mounted in the module cooling box. The positions of the 15 temperature sensors inside the structure can be seen with the numbering that is used throughout this thesis for these temperature sensors. The shown top side of the structure can host three 2S modules with six cooling points, respectively, whereas the bottom side (facing the bottom of the cooling box, not visible here) can host another three 2S modules. Two different insert types are used in this cooling structure. The bottom tip of the inserts, facing the bottom side of the box, can be seen between the actual inserts of the top side. The detector inlet can be found at position 3 while the outlet is positioned at number 1.

ing pipe and protrude out of the carbon fibre surface of the cooling structure.

Each disk of the double disks of the TEDD in the endcap region of the CMS Phase-2 tracker will be assembled out of two half disks, also called dees, so that each dee has a small overlap region that is used to connect two dees to a full disk. Furthermore the cooling pipes are not placed exactly in the middle of the foam layer so that overall six different inserts types are needed for the different regions of the TEDD dees. Additionally the TEDD region in the detector will be subdivided into the TEDD 1 and TEDD 2 since the two regions require disks with different inner radii to accommodate the IT support tube which can also be seen in the tracker layout in Figure 3.1. The dimensions of the used components such as the insert size and the diameter of the cooling pipe are the final dimensions for the dees in the TEDD 1 [51].

The mini-TEDD structure contains two out of the six different insert types that will be later used in the TEDD disks. Since the kapton strips that are glued between the AlCF bridges and the silicon sensors of the 2S module, to isolate the bridges from the high voltage, have a small overhang beyond the size of the silicon sensors, a small step has to be cut out of the inserts so that the kapton strips do not clash with the cylindrical inserts. Figure 5.4 shows a cross section of the CAD drawing of the cooling structure where the picture is only showing the inserts on one side of the middle position. The two insert types that are used in the mini-TEDD, the top long and bottom short insert, can be seen.

Starting from the left side the top long insert is the first, composed of two parts shown in yellow and pink that are both made out of aluminum and enclose the cooling pipe. The orientation of the structure shown here matches the orientation in the cooling box meaning that the mounting holes of the top long inserts face the bottom of the box while the bottom short inserts are showing to the top. The bottom short inserts are also composed of two parts, the yellow part is the main insert part that is composed of aluminum and fully encloses the cooling pipe while the red part is a so-called insert support made out of plastic material [52].

It can be seen that the aluminum part that represents the bottom part of the top long insert, shown in pink in Figure 5.4, has a small tip that also sticks out at the surface and can be seen between the bottom short insert on the top side of the cooling structure. The specific positions of the temperature sensors that are glued to the inserts are indicated by the blue dots in Figure 5.4. An additional CAD drawing of the mini-TEDD structure can be found in Figure A.3 in Appendix A.

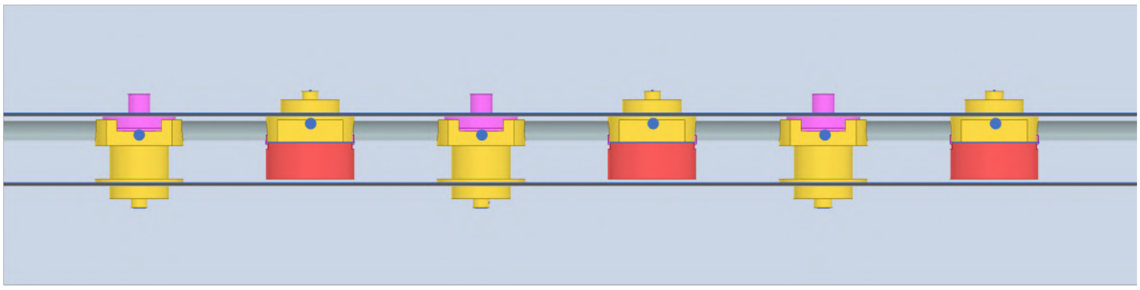

Figure 5.4: Cross section of the CAD drawing of the cooling structure showing the inserts on one side of the middle position. The two insert types used in the mini-TEDD can be seen, the top long and bottom short insert. Starting from the left side the top long insert is composed of two aluminum parts shown in yellow and pink. The bottom short inserts are also composed of two parts, an aluminum part in yellow and a red part made out of plastic material. The blue dots denote the positions of the temperature sensors that are glues to the inserts.

The module will be mounted onto the middle position of the cooling structure using the inserts that face the lid of the cooling box which means that the insert type bottom short will be used for the thermal measurements with the 2S module. In the following the inserts that face the lid of the cooling box will be referred to as the top inserts while the inserts that face the bottom of the box will be called the bottom inserts.

6 Preparatory Measurements

In order to perform thermal measurements a 2S module has to be equipped with temperature sensors that provide a precise temperature measurement of several components of the module, with special interest in the silicon sensors. To ensure a reliable measurement of low temperatures in the order of −20 °C the used temperature sensors have been thermally characterized to confirm that the deviations of the thermistors are in an acceptable range. Also gluing tests on dummy sensors have been performed to test several application processes and determine a method that can establish a good thermal contact between the silicon sensor surface and the temperature sensors. Additionally the expected leakage current in the silicon sensors for the HL-LHC scenario has to be generated in the silicon sensors to be able to emulate the expected power load of the sensors and measure the thermal runaway with unirradiated sensors. Therefore a solution using LED strips has been implemented in the module cooling box as well as a PID control to precisely adjust the generated sensor current by regulating the LED voltage. A detailed discussion of the aforementioned preparations will follow in this section.

6.1 Thermal Characterization of Temperature Sensors

For the precise measurement of temperatures small cylindrical NTC thermistor probes [41] with a diameter of 1.1 mm were chosen, with several of these thermistors already available from previous measurements. To ensure a sufficient accuracy and compatibility in the desired temperature range a characterization measurement has been carried out by binding eleven of these thermistors together and placing them in the cooling bath of a small circulation thermostat. A temperature measurement has been performed at several cooling bath temperatures, starting at −15 °C and increasing the temperature in steps of 5 K until the last measurement point at +20 °C. The measurement results of each thermistor are shown in Figure 6.1. It has been observed that with decreasing temperature of the cooling bath the measured temperatures of the individual thermistors exhibit larger deviations between each other. The largest deviation of two thermistors amounts to a difference of 4 K at a cooling bath temperature of −15 °C which in conclusion shows that these thermistors do not provide sufficient accuracy at low temperatures for the thermal measurements of the 2S module. Additionally the examination of a few temperature probes under the microscope has shown that individual probe tips exhibit small cracks that contribute to the observed aging effect. Two exemplary microscope pictures are provided in Appendix B.

After these observations new temperature sensors of the same kind as well as with a smaller tip with a diameter of 0.5 mm [53] have been procured. To test the new temperature sensors also a characterization measurement has been performed with a slightly improved method. The thermistors have been glued into a sliced can with copper tape and secured with kapton tape so that the can can be placed in the cooling bath of the previously used circulation thermostat. This provides a uniform temperature distribution for the sensors glued inside the can while avoiding direct contact with the coolant in the cooling bath to keep the sensors clean for the later use on the 2S module. A picture of the sensors glued inside the can can be seen on the right in Figure 6.2, with a picture of the setup on the left. In total 40 thermistors have been tested with this method, 20 of each type, distributed over three cans. Measurements have been taken at cooling bath temperatures starting at +20 °C. The temperature was decreased in 5 K steps down to −20 °C. Additionally a calibrated thermometer has been placed next to the can in the cooling bath for comparison.

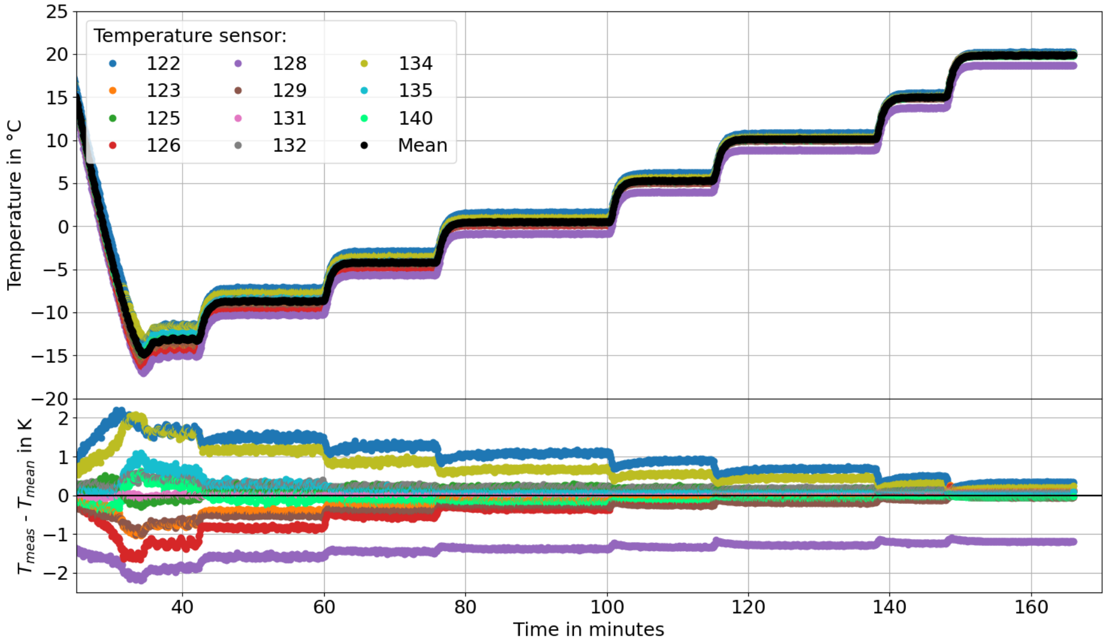

Figure 6.1: Results of the characterization measurement for eleven temperature sensors that have been available from previous measurements. The thermistors have been placed in the cooling bath of a circulation thermostat starting at −15 °C with a measurement point every 5 K up to +20 °C. The upper part of the plot shows the measured temperatures for each sensor and the mean value of all sensors, while the lower part shows the difference between the individual measured temperatures and the mean temperature.

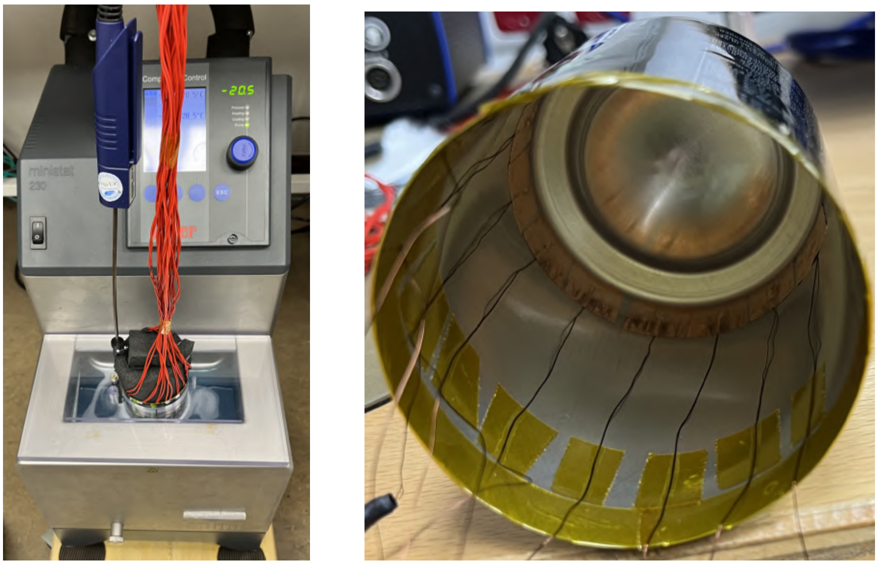

Figure 6.2: Picture of the setup of the characterization measurement of the temperature sensors on the left with the thermometer and a can with thermistors placed in the cooling bath of a small circulation thermostat. The inside of one can is shown on the right with several of the smaller thermistors [53] glued to the side of the can close to the bottom with copper tape and fixated with kapton tape at the top.

The results for all three cans have been very similar and the results for one can as well as the measured temperatures of the thermometer are shown in Figure 6.3. The results show that the measured temperatures of the individual sensors are much better compatible with each other than the old sensors. The measured temperature of the thermometer is generally about 0.5 K lower than the measured temperatures of the thermistors, which is a result of the additional heat load of the can from the environment in this setup.
Figure 6.4 shows a detailed view of the measured temperatures of the individual sensors at the lowest bath temperature of −20 °C. At this measurement point the largest deviation between two sensors is 1 K. During the measurement it has been observed that the measured temperatures are slightly depending on the orientation of the can inside the cooling bath. Thus an additional rotation measurement has been performed for a set of temperature sensors during which the can has been rotated around the mid axis so that each sensor was at each sensor position at −20 °C. By calculating the mean measured temperature of each sensor at each position of the can the deviation as a result of the can position in the cooling bath can be estimated. In this way the largest deviation between the different measurement positions for each sensor have been determined and averaged, resulting in a mean deviation of 0.72 K for the measured sensors. This means that overall an uncertainty of 0.3 K has been measured for the temperature sensors at a cooling bath temperature of −20 °C. Since the measurement of all three cans have shown similar results the measured uncertainty of 0.3 K will be used in the following as a systematic uncertainty for the measurement of each temperature sensor.

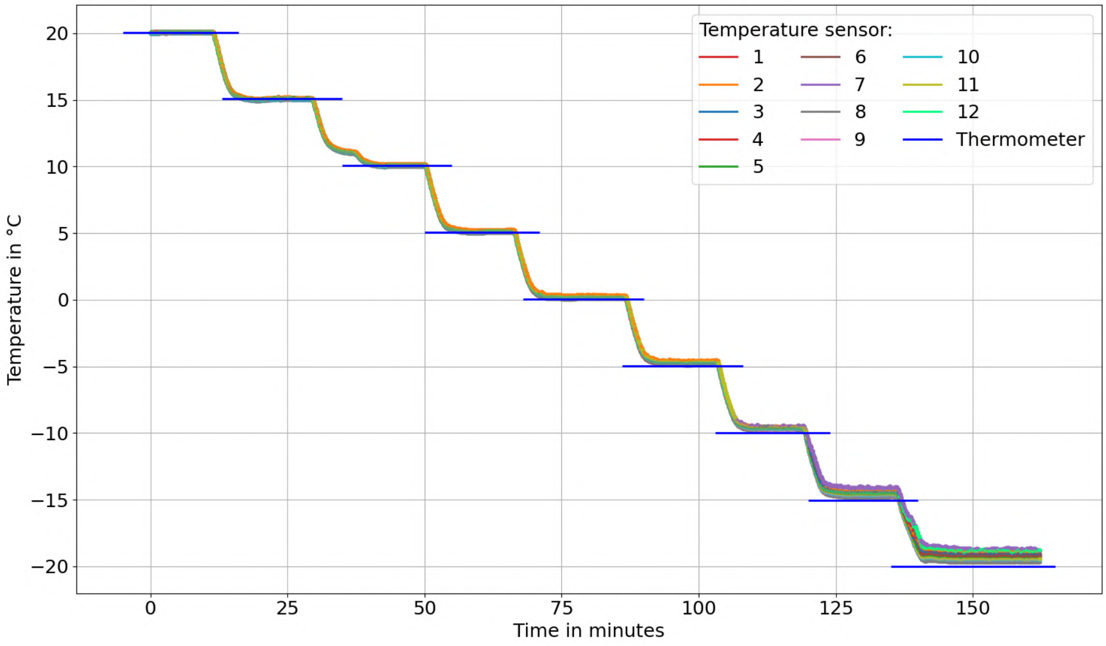

Figure 6.3: Results of the characterization measurement for one can with 12 new temperature sensors glued inside. The can has been placed in the cooling bath of a circulation thermostat starting at +20 °C with a measurement point every 5 K down to −20 °C. The measured temperatures for each temperature sensor are shown in this plot. Additionally a calibrated thermometer has been placed next to the can in the cooling bath and the measured temperatures at each measurement point are indicated with a blue line.

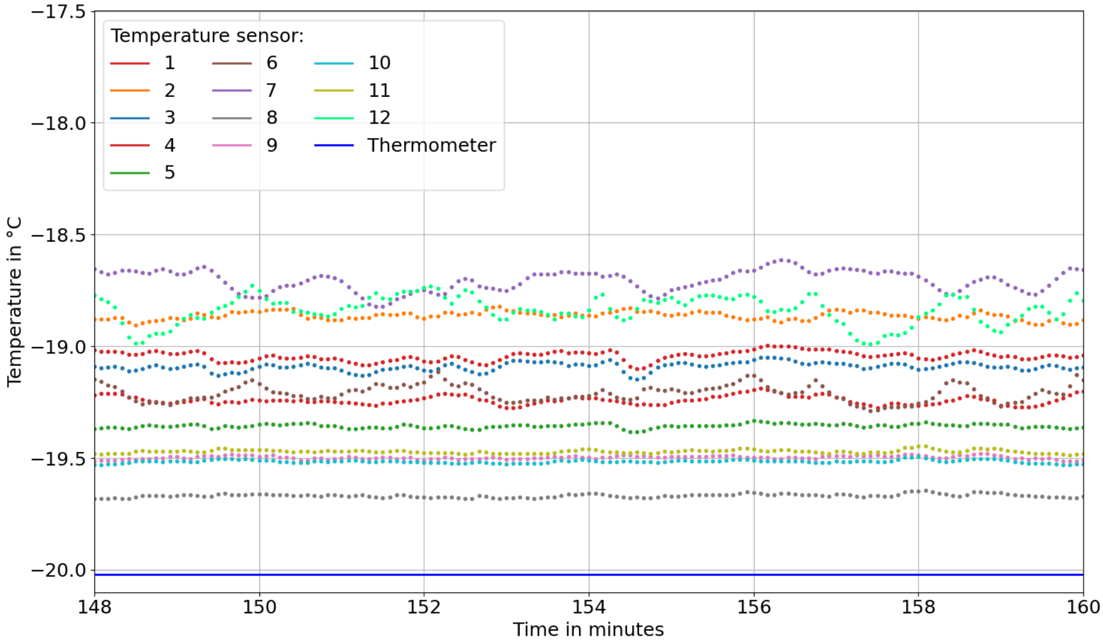

Figure 6.4: Detailed view of the measurement points at −20 °C of the characterization measurement of the temperature sensors. The measured temperature of each sensor is shown in a different color while the measured temperature of the calibrated thermometer is indicated with a blue line. It can be seen that the largest deviation between two sensors yields 1 K at this measurement point.

6.2 Gluing Tests of Temperature Sensors on Dummy Sensors

For the temperature measurement of all components of the 2S module the smaller temperature sensors [53] with a diameter of 0.5 mm have been chosen. To equip the 2S module with temperature sensors gluing tests have been performed on dummy sensors since a reliable measurement of the silicon sensor temperature is essential for the measurement of the thermal runaway while not damaging the silicon sensor surface.
Within the module assembly at this institute good results have been achieved with the usage of the encapsulant Sylgard 186 [54] for the protection of the wirebonds of the 2S module. Based on this experience the encapsulant was chosen as a suitable glue to secure the temperature sensors on the silicon sensor surface. To determine whether the usage of only encapsulation provides sufficient thermal contact to the silicon sensor surface or if additional thermal paste has to be applied between the temperature sensors and the silicon sensors, a first gluing test with three thermistors has been performed. Two thermistors have been coated with Gap Filler 4000 [55] before placing them on a dummy sensor by hand and gluing them to the surface by applying a small amount of the encapsulant with a hand dispenser. The third thermistor has been glued to the dummy sensor without the thermal paste. On the left picture in Figure 6.5 the three thermistors can be seen glued to the dummy sensor with the top two being the temperature sensors with the additional thermal paste. The dummy sensor was then placed onto the cooling plate of a peltier element [56] to test the thermal performance. A small box has been placed above the dummy sensor and flushed with dry air to avoid condensation on the cooling plate. For the measurement the temperature of the cooling plate was decreased in small steps from +20 °C until the last measurement point at +4.5 °C.

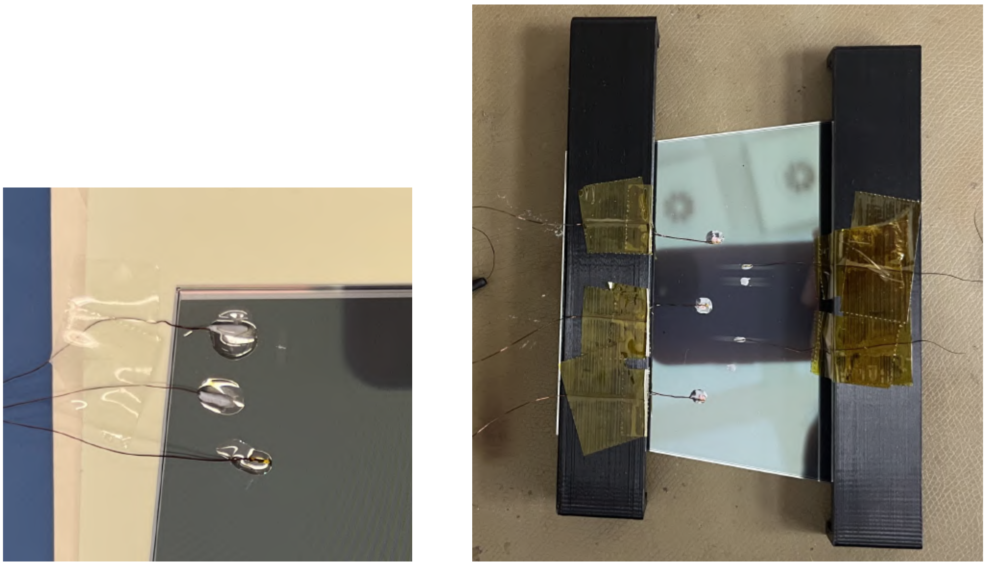

Figure 6.5: Left: picture of the first gluing test with three temperature sensors glued to a dummy sensor. The first two sensors from the top have been coated with Gap Filler 4000 and then secured on the silicon sensor with encapsulation, while the third sensor has been glued using only encapsulation. Right: picture of the second gluing test with five temperature sensors glued to a dummy sensor. The left row has been glued with Gap Filler 2000 and encapsulation while Keratherm KP 92 has been used for the row on the right.

The result of this measurement can be seen in Figure 6.6. It can be observed that especially at the end of the measurement at a cooling plate temperature of 4.5 °C the measured temperature of the thermistor that was glued with only encapsulation shows a deviation of 0.5 K to the two other thermistors glued with additional thermal paste. The measured temperatures of these thermistors are compatible with the set cooling plate temperature so that it can be concluded that the use of thermal paste is necessary to establish a good thermal contact to the silicon sensor surface.

However, the application of a small amount of Gap Filler 4000 to the temperature sensors was difficult because of its texture so that a second gluing test was performed with two other thermal pastes. A picture of this gluing test can be seen in Figure 6.5 on the right, showing two rows of temperature sensors glued on a dummy sensor. The left row is composed of three temperature sensors that have been glued to the dummy sensor with Gap Filler 2000 [57] and secured with encapsulation, while for the two sensors on the right Keratherm KP 92 [58] has been used as a thermal paste. In general the gluing procedure has been improved for this gluing test: two 3D printed bridges have been used to fixate the temperature sensors until the encapsulation is dry. The bridges have a height of a few centimeters so that the thin cables of the temperature sensors can be fixed with kapton tape on the bridge itself and bent until the tip of the sensor reaches the desired position. A small amount of thermal paste is then applied along the length of the thermistor tip. The thermistors are then placed on the silicon sensor and positioned in such a way above the dummy sensor that the thermistor tips reach the desired position on the silicon sensor surface. If necessary a small tweezer can be used to carefully correct the position of the thermistor tip. A small amount of encapsulation is then applied to each thermistor tip to secure it on the silicon sensor.

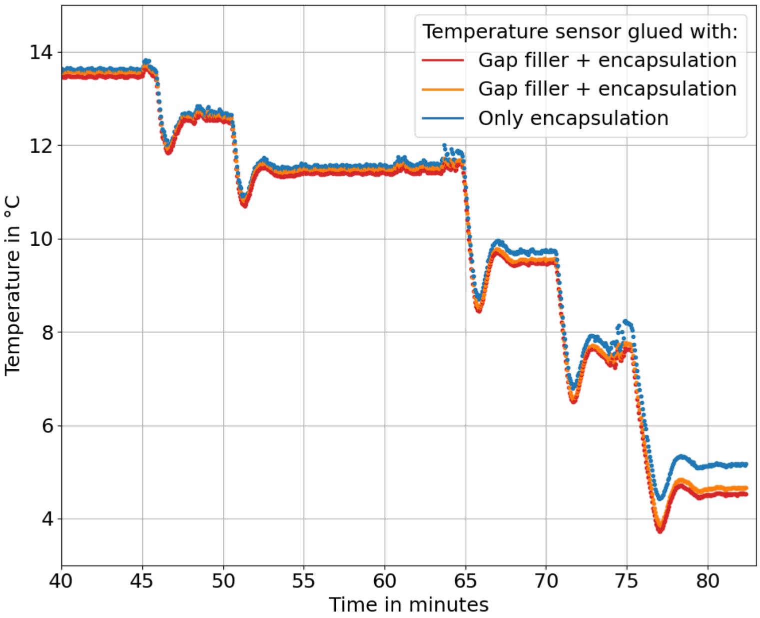

Figure 6.6: Results of the measurement of the dummy sensor of the first gluing test on a cooling plate of a peltier element. Two thermistors have been glued to the sensor with Gap Filler 4000 and encapsulation, the third using only encapsulation. Several cooling plate temperatures have been measured with the last temperature being set to +4.5 °C.

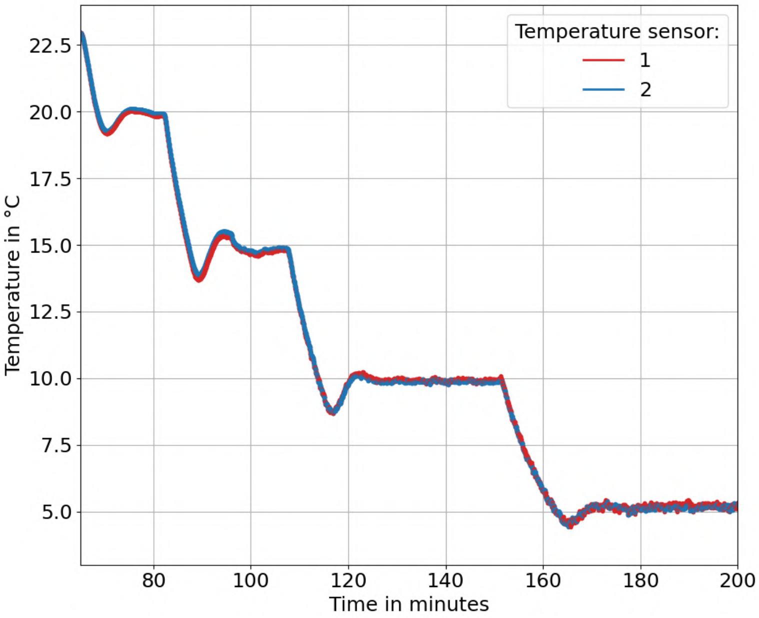

Figure 6.7: Results of the measurement of the dummy sensor of the second gluing test on a cooling plate of a peltier element showing the measured temperatures of two thermistors glued with Gap Filler 2000 and encapsulation to the dummy sensor. Measurements have been performed at cooling plate temperatures of +20 °C, +15 °C, +10 °C and +5 °C.

After approximately 24 hours the encapsulation is dry and the thermistor cables can be removed from the bridges. On the right picture in Figure 6.5 it can be seen that the used thermal paste Keratherm KP 92 in the right row leaves flowmarks on the silicon sensor surface which does not make it suitable for the gluing on the silicon sensors of the 2S module. Consequently only Gap Filler 2000 can be used as a thermal paste for this application.

The measurement at different temperatures on the cooling plate of the peltier element has been repeated for this dummy sensor to check the thermal contact of the thermistors. The results for two temperature sensors of the left row are shown in Figure 6.7. The third sensor was unfortunately broken due to an unrelated problem and could therefore not be read out for this measurement. The cooling plate temperature was initially set to $+20\,^{\circ}\mathrm{C}$ and then decreased in steps of $5\,\mathrm{K}$ down to a temperature of $+5\,^{\circ}\mathrm{C}$. The results show that the measured temperatures of the two temperature sensors are compatible with the set temperatures of the cooling plate and are well compatible with each other. This confirms that a good thermal contact can be established between the temperature sensors and the silicon sensor surface when using Gap Filler 2000 and encapsulation, which makes this a suitable gluing method.

6.3 Gluing of Temperature Sensors on the 2S Module

For the thermal measurements in this thesis the 2S module 2S_40_6_AAC-00003 built at the end of 2022 by the Physics Institutes 1B and 3B at RWTH Aachen University has been used. The module has a sensor spacing of 4.0 mm and six cooling contacts. For the gluing of the temperature sensors on the 2S module the gluing method of the second gluing test, described in the previous section, has been used for most of the components of the 2S module. The picture in Figure 6.8 shows the glued temperature sensors on the top sensor of the 2S module during the drying time. Both silicon sensors of the 2S module have been equipped with seven temperature sensors each, one in the middle of each sensor and two rows of three thermistors in parallel to the FEHs. In Figure 6.8 it can be seen that the 3D printed bridges have been used for the gluing of the thermistors on the sensor to fixate and position the thermistors during the process. The 2S module itself is placed onto a so-called carrier made out of aluminum for the overall procedure.

After the drying time the 3D printed bridges have been removed and the three hybrids of the 2S module have been equipped with temperature sensors using the same technique. Each FEH has been equipped with five temperature sensors, three on the top and two on the bottom side. On the top side a thermistor has been placed on the CIC, one CBC and directly on the surface of the FEH next to the CIC, respectively. On the bottom side a temperature sensor has been glued at each corner of the FEH next to the edges of the AlCF bridges to which the FEHs themselves are glued to. Five temperature sensors are distributed over the different components of the SEH: on the aluminum shield of the DC-DC converters, the LpGBT, the bottom side of the VTRx+ and two respectively under the tails of the SEH that are used to connect the SEH with the FEHs.

Each AlCF bridge of the 2S module is also equipped with a temperature sensor. Since the three hybrids are glued onto the AlCF bridges from the top side, the temperature sensors are glued to the AlCF bridges from the bottom side of the module using copper tape. A picture of the flipped 2S module can be found in Figure 6.9. The six temperature sensors on the AlCF bridges, the seven thermistors on the silicon sensor and the four thermistors in the corners of the FEHs can be seen after the gluing process.

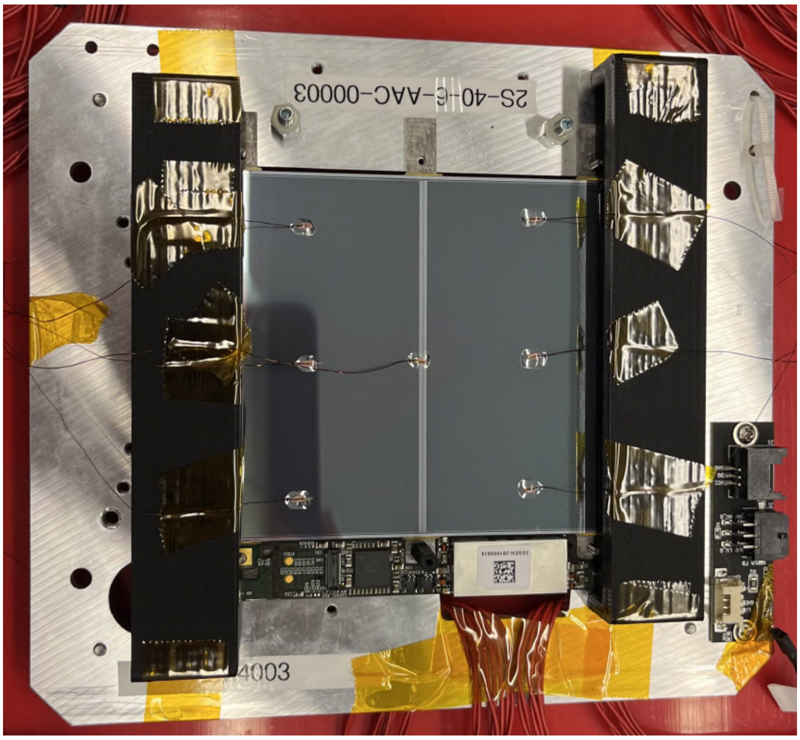

Figure 6.8: Picture of seven temperature sensors glued onto the top sensor of the 2S module during the drying time. Two 3D printed bridges are used to fixate and position the thermistors during the process. The 2S module itself is placed onto a carrier during the procedure.

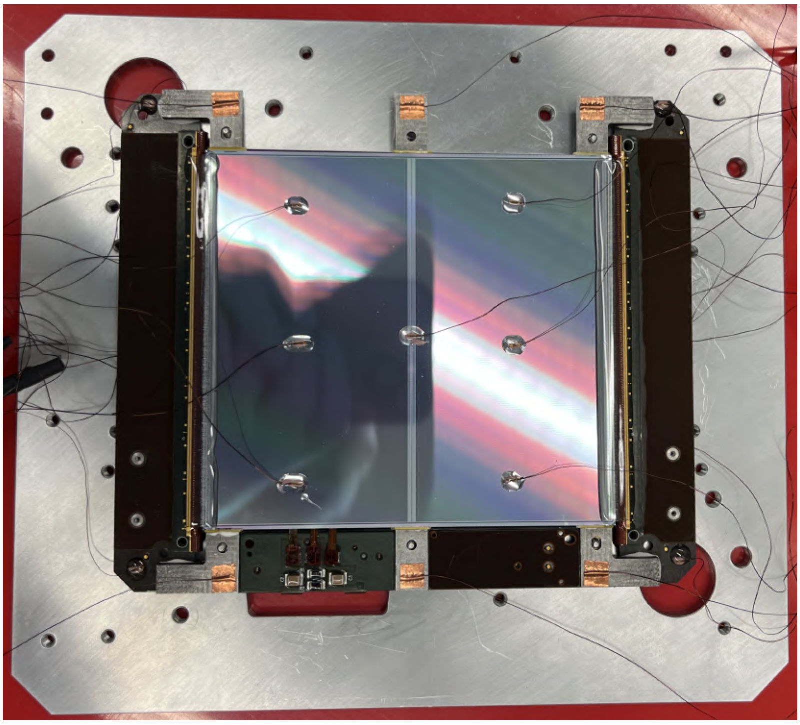

Figure 6.9: Picture of the bottom side of the 2S module after the gluing of the thermistors. In total six thermistors are glued onto the AlCF bridges with copper tape, seven thermistors are glued with thermal paste and encapsulation onto the silicon sensor and four in the corners of the FEHs.

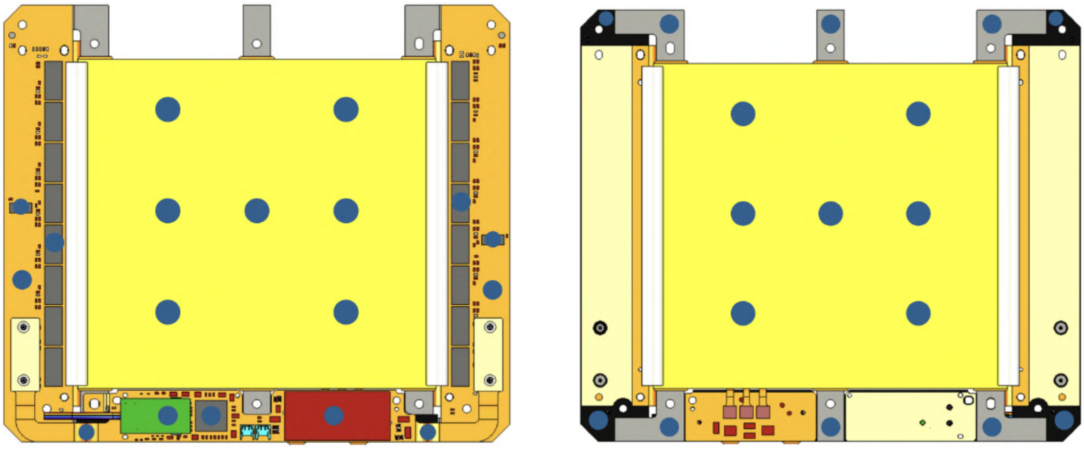

Figure 6.10: Overview of all 35 temperature sensors that are glued to the 2S module. The top side of the module is shown on the left, the bottom side on the right. The positions of the sensors are indicated by the blue dots.

In total the 2S module is thus equipped with 35 thermistors. An overview of the positions of all glued thermistors on the top and bottom side of the 2S module is shown in Figure 6.10. For the integration of the 2S module on the mini-TEDD structure the bottom sensor only has a small distance of around 1.4 mm to the surface of the cooling structure. Since the temperature sensors themselves already have a diameter of 0.5 mm special attention has been paid to keep the used thermal paste and encapsulation material to a minimum during the gluing of the temperature sensors to the bottom sensors to prevent a contact of the temperature sensors and the surface of the cooling structure after installation.

6.4 Generation of Leakage Current with LEDs

In case of insufficient cooling the effect of thermal runaway can occur as a consequence of the temperature-dependent leakage current of irradiated silicon sensors. To measure the thermal runaway with the used 2S module in this thesis a method has been implemented to emulate the expected temperature-dependent leakage current in the unirradiated silicon sensors of the module. The basic idea is to use a light source to illuminate the top and bottom sensor since the emitted photons generate electron-hole pairs in the silicon and thus induce a current in the strips of the sensor. For the measurements in this setup the concrete realization has to meet several specifications: both silicon sensors have to be illuminated so that an equal power load is generated, the light source has to fit into the small space between the bottom sensor and the surface of the cooling structure without touching the sensor surface or the glued temperature sensors and it should not produce any additional heat load itself. Lastly the light source has to be dimmable such that the generated leakage current in the silicon sensor is adjustable in the range of a few mA.
The first idea was to use a thin electroluminescent foil but since it is AC powered this induced an AC current in the silicon sensors which is not suitable to produce a constant power load in the sensors. Eventually a solution using LED strips [59] with small LEDs with a height of 0.75 mm on a self-adhesive strip with a distance of 1.5 cm between the LEDs was found that meets all previously mentioned specifications. The LEDs emit white light, are powered with 12 V DC and are dimmable by regulating the applied voltage. In general the LED strips are separable every 5 cm with three LEDs on each section.

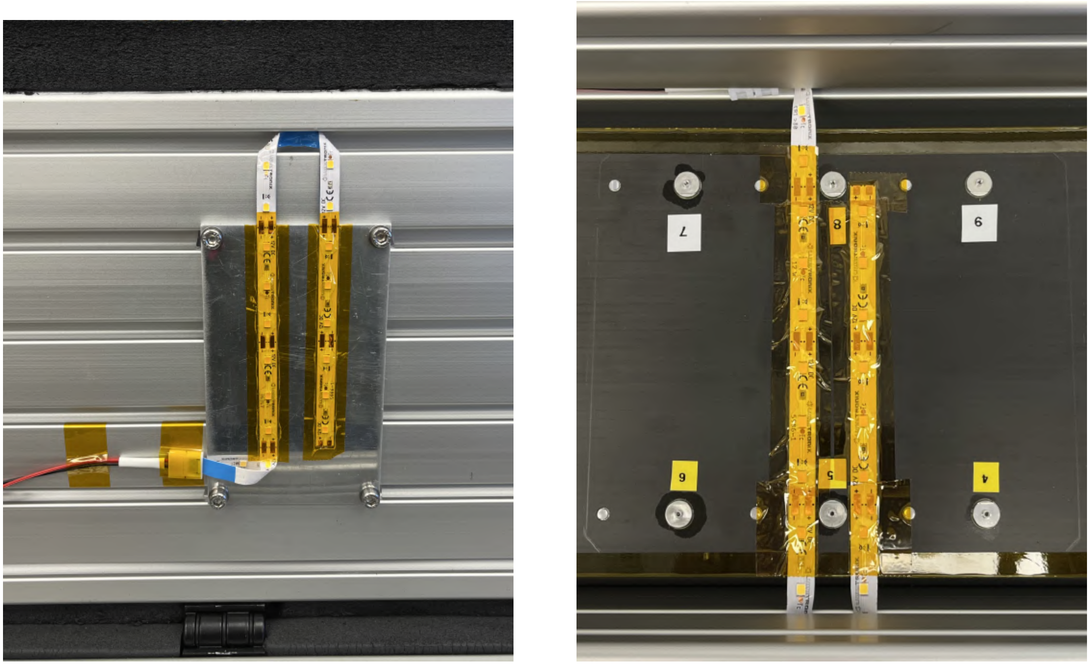

Figure 6.11: Picture of the LED strip attached to an aluminum plate in the lid of the module cooling box on the left, while the LED strip placed on the surface of the cooling structure can be seen on the right.

Two LED strips have been placed in the module cooling box to illuminate the top and bottom sensor of the module in the middle position of the cooling structure. In the left picture in Figure 6.11 the LED strip for the top sensor in the lid of the cooling box can be seen. It has been attached to a small aluminum panel that is screwed to the inside of the lid of the box. In the right picture of Figure 6.11 the LED strip to illuminate the bottom sensor attached to the surface of the cooling structure can be seen. It has been arranged such that the LEDs sit in between the rows of temperature sensors of the bottom sensor and do not collide with them when placing the 2S module on the inserts of this position. Both LED strips have been positioned so that six LEDs in one row can illuminate one half of each silicon sensor. Since the LED strips are arranged in sections of three, one can permanently turn off the LEDs of a section by removing a resistor in the circuit of that specific section. This has been done with the LED sections in the U-turn of each strip so that only the six LEDs of each row of each strip are turned on when powering the strip. This means that in total 12 LEDs are used to illuminate one sensor, respectively. Both strips are connected to a Hameg HMP 4040 power supply [60] and are powered separately by regulating the voltage. The strips have been isolated with kapton tape.
To measure the induced leakage current in dependence of the applied LED voltage the high voltage for the sensors is provided by a Keithley 2410 SourceMeter [61]. A detailed description of the integration of the 2S module onto the cooling structure will follow in Section 7.3. The measurement has been performed in cold with a module cooling box temperature of $-20\,^{\circ}\mathrm{C}$ and a bias voltage of $300\,\mathrm{V}$ while the low voltage of the module has not been turned on. For the measurement the LED voltage was increased in steps of $10\,\mathrm{mV}$ and the sensor current was measured after each voltage step. This has been performed separately for the top and bottom LED strip while both sensors of the module have been connected to the high voltage. The results of the measurement are shown in the left plot in Figure 6.12.

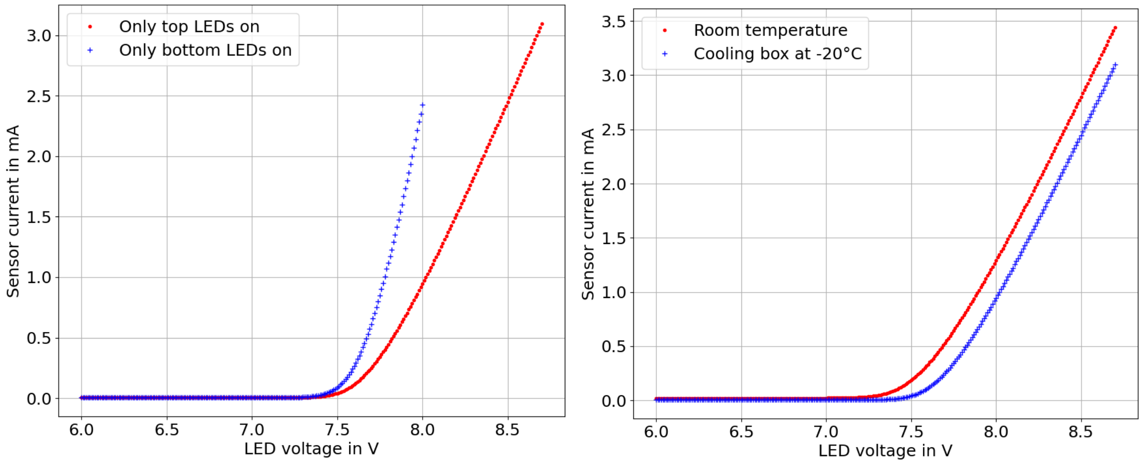

Figure 6.12: Left: result of the measurement of the sensor current at a module cooling box temperature of $-20\,^{\circ}\mathrm{C}$ and a bias voltage of 300 V. The voltages of the LED strips have been increased in steps of 10 mV and the sensor current has been measured after each step. The result for the top LED strip is shown in red, while the result for the bottom strip is shown in blue. Right: result of the measurement of the top LED strip at room temperature in red, while the measurement at a cooling box temperature of $-20\,^{\circ}\mathrm{C}$ is shown in blue.

First of all it can be seen that the measured current increases with increasing LED voltage in the desired range of a few mA. It can be noticed that after reaching a certain LED voltage the induced current increases linearly, but with a different gradient for the top and bottom LED strip. This is a result of the different distances between the two LED strips and the respective sensor surface. The bottom LED strip is much closer to the bottom sensor and thus a smaller LED voltage already leads to a higher sensor current than for the top sensor.

To test if by regulating the voltage of the top LEDs a current is induced only in the top sensor and the other way around an additional measurement at room temperature has been performed. Since both sensors are connected to the high voltage circuit via the high voltage pigtails, for this measurement the pigtail has been plugged out for one sensor so that only the current of the other sensor can be measured. By illuminating the sensor that is not connected to the high voltage the influence of the LEDs on the current of the other sensor can be estimated. In Figure 6.13 the left plot shows the measured current of the bottom sensor with increasing voltage of the top LEDs while the top sensor is plugged out, while the right plot shows the measured current of the top sensor with increasing voltage of the bottom LEDs while the bottom sensor is plugged out. Both measurements exhibit a small dependence of the measured current on the LED voltage, but since this effect is in the order of $10\,\mu$A for the bottom sensor and even lower for the top sensor, it can be neglected. Therefore it will be further assumed that the current can be regulated independently for both sensors.

Furthermore it has been observed that when comparing measurements at room temperature with measurements at cold temperatures the LED voltage that is necessary to generate a certain leakage current value in the silicon sensors is also dependent on the temperature of the module cooling box. In the right plot of Figure 6.12 the measurement of the current with increasing voltage of the top LEDs can be seen at room temperature in red and at a module cooling box temperature of $-20\,^{\circ}\mathrm{C}$ in blue. Since thermal measurements at different ambient temperatures with the 2S module will be performed, a PID control has

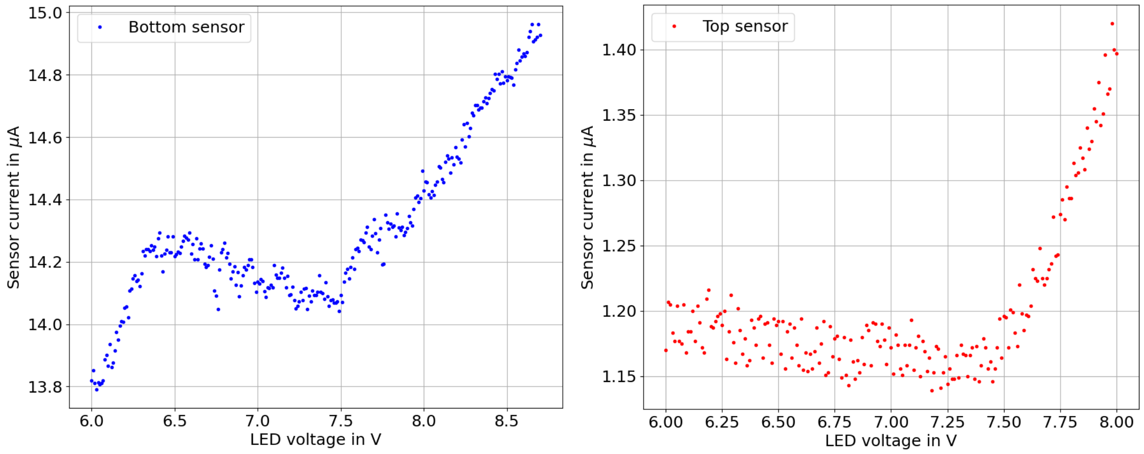

Figure 6.13: The left plot shows the measured current of the bottom sensor with the top LED strip turned on while the right plot shows the measured current of the top sensor with the bottom LED strip turned on. For each measurement the high voltage pigtail of the respective other sensor of the 2S module is plugged out.

been implemented that automatically regulates the LED voltage of both LED strips until the desired current is reached so that this temperature effect is accounted for. A detailed description of the developed PID control is given in the next section.

6.4.1 Regulation of the Generated Current using a PID Control

To automatically regulate the induced current of the LED strips in the silicon sensors of the 2S module to a specific current value a proportional-integral-derivative (PID) control has been developed that adjusts the voltage of the LED strips until the desired current value is reached. In general a PID control denotes a routine that uses a feedback loop to apply a correction to a control function. It calculates the difference between the desired value and the measured process variable and determines the correction based on a proportional, an integral and a derivative term. Here the PID control has been implemented in LabView using an already available PID control application. The used PID algorithm can control one process variable, the measured sensor current in this case, by correcting one control variable, which is here the LED voltage.

Since the generated current at a specific voltage value is different for each LED strip but only one variable can be corrected in the control loop of the PID algorithm the following concept is applied. Based on the assumption that each LED strip only induces current in its respective opposed sensor, the ratio of the voltages of the two LED strips is determined so that the PID algorithm can use one LED voltage as the control variable and the second LED voltage can then be set according to the determined relation between the two voltages. For this the linear parts of the measured sensor current for both LED strips as seen in the left plot in Figure 6.12 have been fitted with a linear function so that the ratio of the voltages of both LED strips can be calculated for a current range of 0.5 mA to 2.4 mA. The ratio has been calculated by dividing the voltage of the bottom LED strip by the voltage of the top LED strip in the given current range with a step size of 0.1 mA. The result can be seen in Figure 6.14. The calculated ratio shows a linear relation between the LED voltages so that by fitting this ratio with a linear function an equation can be determined that can be used to calculate the necessary voltage of the bottom LED strip

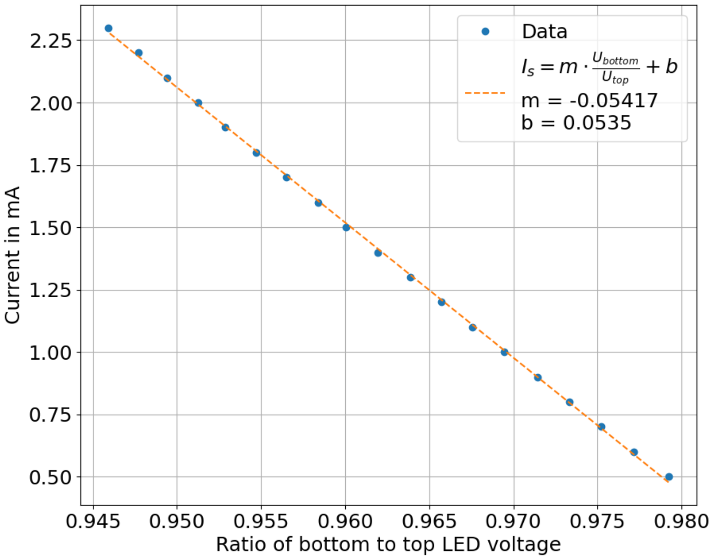

Figure 6.14: Ratio of the voltage of the bottom LED strip to the voltage of the top LED strip in a current range of 0.5 mA to 2.4 mA. The data in blue has been fitted with a linear function. The result of the fit is shown in orange.

from the top LED voltage as optimized by the PID control. The result of the fit can also be seen in Figure 6.14. With this method the PID control can generate half of the desired leakage current with the top LEDs and the other half with the bottom LEDs so that the full high voltage power is equally distributed among both silicon sensors.
A screenshot of the LabView program is shown in Figure 6.15. The desired current value can be entered in the program that then regulates the LED voltages with the described method, measures the present sensor current and corrects the voltages until the desired current value is reached. The plot in Figure 6.15 shows the slow increase of the measured sensor current until the desired value of 1.57 mA has been reached. The used PID parameters for the algorithm have been experimentally found and optimized.

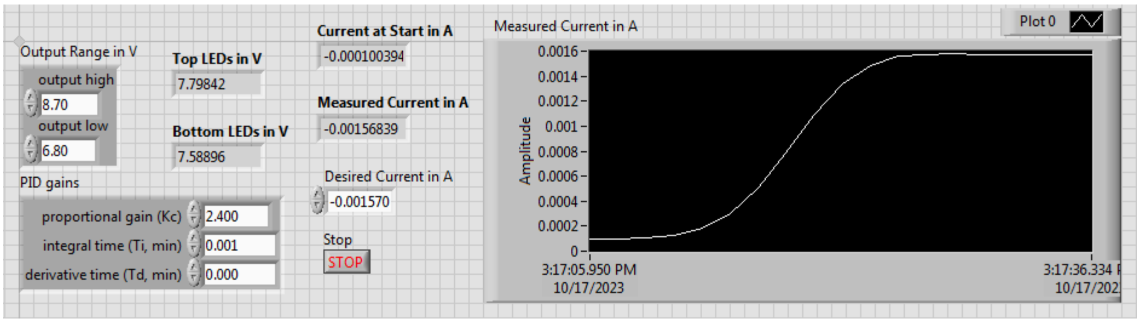

Output Range in V
output high 8.70
output low 6.80

Top LEDs in V 7.79842

Bottom LEDs in V 7.58896

PID gains
proportional gain (Kc) 2.400
integral time (Ti, min) 0.001
derivative time (Td, min) 0.000

Current at Start in A -0.000100394

Measured Current in A -0.00156839

Desired Current in A -0.001570

Figure 6.15: Screenshot of the PID control for the sensor current as implemented in LabView. The desired sensor current can be entered and the PID control then regulates the LED voltages until the desired value is reached. Here the regulation to a sensor current of 1.57 mA using the PID control at a sensor bias voltage of 600 V can be seen. The plot shows the measured sensor current versus the time. The sensor current increases slowly until the desired value is reached and the program is stopped.

7 Thermal Characterization of the Setup and Integration of the 2S Module

To test the thermal behavior of the cooling structure in the setup two characterization measurements have been carried out before the integration of the 2S module onto the cooling structure. In a first measurement the thermal interface between the inserts and the cooling pipe has been investigated by using a heating resistor to apply a certain heat load onto the inserts and measure the temperature difference between the insert and the resistor to determine the thermal resistance of each insert. By comparing the different values their compatibility can be evaluated. In the second part the thermal contact between the AlCF bridges and the inserts as a function of the applied torque has been measured using a heating device composed of a heating resistor glued to a stump bridge. The results of these measurements will be discussed in the following sections as well as the integration of the 2S module onto the cooling structure inside the module cooling box.

7.1 Thermal Characterization of the Inserts

For the thermal characterization of the inserts a small heating resistor [62] with a resistance of 200 Ω was used that was screwed to the respective insert with screws and a flat washer out of brass with a torque of 6 Nm. A small temperature sensor was glued on top of the heating resistor with copper tape. In Figure 7.1 a picture of the heating resistor screwed to insert 7 of the middle position of the cooling structure can be seen on the left while an overview of the numbering of the inserts of the middle position is shown in the right picture. To characterize the individual inserts of the middle position of the cooling structure the heat load was varied between 0.2 W and 1.6 W in steps of 0.2 W.

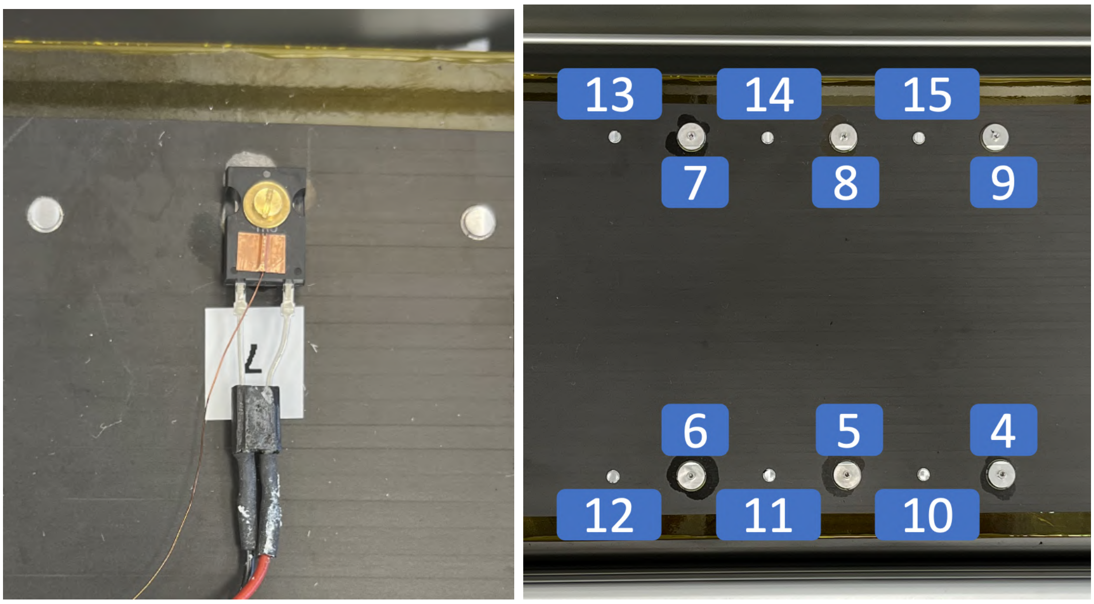

Figure 7.1: Left: picture of the heating resistor used for the thermal characterization of the inserts. It is screwed to insert 7. A temperature sensor is glued to its surface with copper tape. Right: overview of the insert numbering of the middle positions of the mini-TEDD cooling structure.

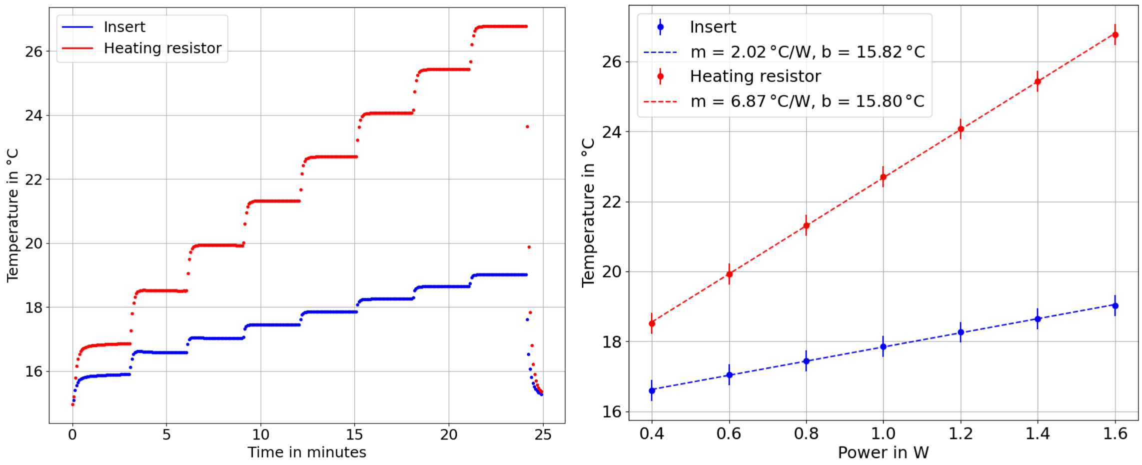

Figure 7.2: Left: results of the measurement with the heating resistor for insert 7. A heat load from 0.2 W to 1.6 W was applied in steps of 0.2 W. The measured temperature of the insert is shown in blue, the heating resistor is shown in red. Right: results of the linear fit of the measured temperatures per power step for the insert and heating resistor for insert 7. The insert is shown in blue, the heating resistor in red. The thermal resistances resulting from the fit can also be seen.

For each insert the temperatures of the heating resistor and the respective insert, using the temperature sensor glued to the insert inside the cooling structure, have been measured. The measurements have been performed at a CO_2 temperature of $+15\,°C$ with a mass flow of around $1.8\,g/s$, an ambient temperature inside the module cooling box of $+15\,°C$ and a small dry air flow of $4\,l/min$ into the box.

The result of the measurement for insert 7 is shown in the left plot in Figure 7.2. It can be seen that the measured temperature increases for each power step, while the temperature of the heating resistor is generally higher than the insert temperature, which is the expected behavior. To compare the thermal performance of the six inserts with each other the thermal resistance is estimated for each insert. Therefore the mean measured temperature is calculated for each measurement point and plotted against the applied power load. Although the waiting time has been the same for each measurement point, it has been observed that stable condition could not be achieved for the measurement with a heat load of 0.2 W. This is why the analysis will start at a heat load of 0.4 W for all inserts. The data is then fitted for each insert with a linear function. An uncertainty of 0.3 K has been used for the temperature measurement of the heating resistor and the insert, respectively. The result of the fit for insert 7 is shown in the right plot in Figure 7.2. The determined thermal resistances for all six inserts can be found in Table7.1. The mean value is $\alpha_{15\,°C} = (2.10 \pm 0.20)\,K/W$.

When comparing the thermal resistances of the six inserts a maximum difference of $0.5\,K/W$ can be observed between the minimum and maximum measured resistances. Since the inserts are glued to the cooling pipe, the fluctuations can be attributed to varying glue thicknesses between the individual inserts and the cooling pipe. A similar measurement on an earlier version of a cooling structure prototype performed at this institute exhibited deviations between the inserts in a comparable range, which could be attributed to the individual glue thicknesses based on a comparison with a Finite Element (FE) simulation [34]. Overall the results of the measurement indicate that all tested inserts display a sufficient thermal behavior without any distinctive features.

Insert number	Thermal resistance of insert in K/W	Thermal resistance of heating resistor in K/W
4	1.91	6.52
5	2.05	6.91
6	2.31	6.56
7	2.02	6.87
8	1.88	7.08
9	2.43	7.22

Table 7.1: Results of the measured thermal resistances of the insert and heating resistor for all six inserts of the middle position of the cooling structure. The measurement was performed at a CO_2 temperature of +15 °C.

7.2 Thermal Contact between Bridge and Insert as a Function of the Torque

For the installation of the 2S modules on the cooling structures the modules will be screwed to the inserts using the holes in the AlCF bridges with torques in the range of a few cNm. To determine the dependence of the thermal contact between the bridges and the inserts on the torque and find the optimal value a series of measurements with different torque values has been performed. For this measurement a dedicated heating device has been built that is composed of a heating resistor glued to a single AlCF stump bridge. The same heating resistor as for the measurements in the previous section has been used while a stump bridge designed for a 2S module with a sensor spacing of 1.8 mm has been chosen. The heating resistor was glued to the stump bridge using Polytec EP 601-LV [63], which is also used to glue the SEH to the bridges of a 2S module during the assembly.

For all measurements the stump bridge has been screwed to insert 7 using a brass screw with a M1.6 thread and a length of 4 mm and washers also made out of brass that have been specially designed to embrace the nipple of the insert as well as the screw head. Small temperature sensors have been glued to the heating resistor as well as the stump bridge with copper tape. A picture of this heating device screwed to insert 7 of the middle position of the mini-TEDD structure is shown on the left in Figure 7.3.

For the measurements a power load of 3 W has been applied to the heating resistor. The CO_2 temperature was set to 0 °C while the module cooling box has been cooled down to a temperature of +7.6 °C, which is in the range of the bridge temperature, so that the heat exchange between the stump bridge and the ambient is minimized. Measurements have been performed for torque values between 5 and 12 cNm in steps of 1 cNm and each torque value has been measured three times. Between each torque step the screw has been fully loosened and then screwed in again with the new torque value using a torque wrench. For each torque value the resistor, bridge and insert temperatures have been measured.

To investigate the thermal contact the temperature difference between the bridge and the insert has been calculated for each of the three measurements of each torque. The individual results of these differences can be seen in the right plot in Figure 7.3 in red, while the mean value and standard deviation for each measured torque can be seen in blue. It can be observed that the temperature difference between the bridge and the insert decreases with increasing torque, which is compatible with the idea that the thermal contact improves when a higher force is applied. It is also visible that some torque values exhibit larger deviations between the three measurements than others. A possible explanation could be

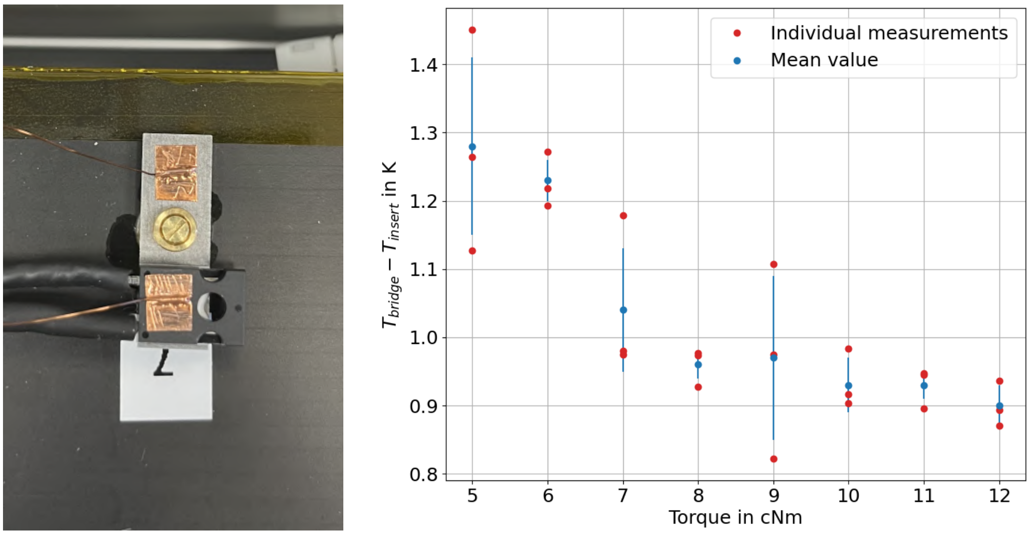

Figure 7.3: Left: picture of the heating device composed of a heating resistor glued to an AlCF stump bridge. The stump bridge is screwed to insert 7 of the cooling structure with the dedicated brass screw and washer. Temperature sensors are glued to the stump bridge and resistor with copper tape, respectively. Right: result of the difference between the measured bridge and insert temperature for each of the three measurements for each applied torque in red. The mean value and standard deviation for each torque is shown in blue. The measurements have been performed at a CO_2 temperature of 0 °C and a module cooling box temperature of +7.6 °C. A power load of 3 W has been applied to the heating resistor.

that the thread of the insert has been damaged especially when using a higher torque but the cause has not been fully identified. The measurement shows that the temperature difference reaches a plateau after a torque of 8 cNm, which indicates that a value of 8 cNm or higher provides an optimized thermal contact between the bridge and the insert. Within the collaboration so far a value of 10 cNm has been targeted whose use can be reassured with this measurement.

7.3 Integration of the 2S Module on the Cooling Structure

For the thermal measurements in this thesis the 2S module 2S_40_6_AAC-00003 with a sensor spacing of 4.0 mm and six cooling contacts has been equipped with temperature sensors, as described in Section 6.3. In Figure 7.4 a picture of the 2S module integrated onto the cooling structure can be seen. The 2S module has been carefully placed on the six inserts of the middle position of the cooling structure. In general there is a small distance between the surface of the cooling structure and the bottom sensor of the module of 1.4 mm. Although it has been made sure that during the gluing of the temperature sensors to the bottom sensor the used encapsulation material is kept to a minimum as far as possible it has been realized at the first integration attempt of the module on the cooling structure that the module does not lie flat on all six inserts. This has been caused by too much encapsulation material on the central temperature sensor on the bottom sensor who was in contact with the cooling structure surface. Subsequently this temperature sensor had to be removed by carefully pulling it from the bottom sensor and removing the encapsulation left on the sensor with a pair of tweezers.

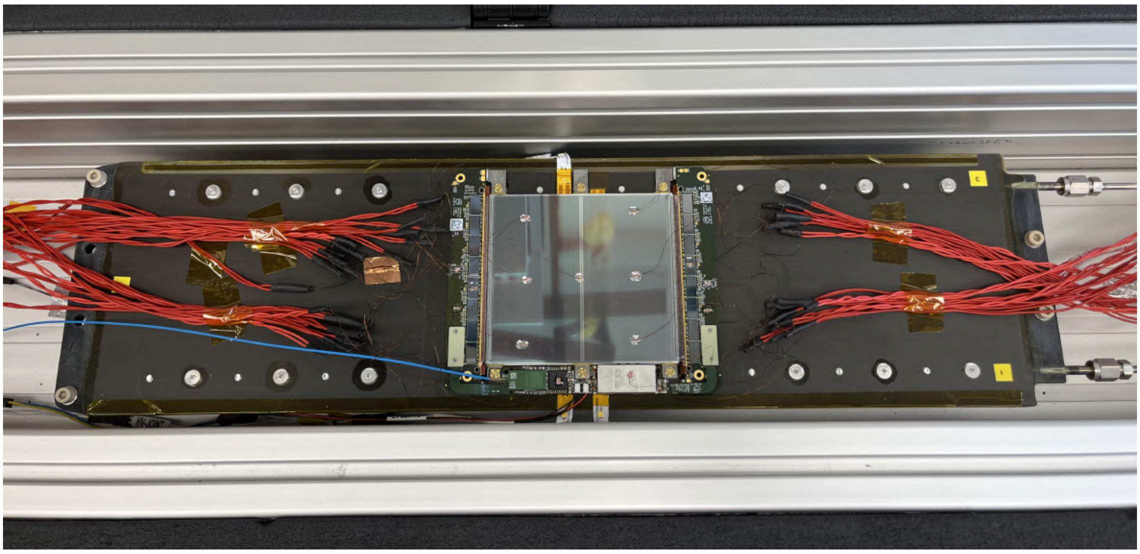

Figure 7.4: Picture of the 2S module equipped with temperature sensors integrated onto the cooling structure inside the module cooling box. The module is placed on the middle position of the cooling structure and screwed to the six inserts with the dedicated screws and washers. The cables of the attached thermistors can be seen in red. They are directed out of the box at the left and right side.

The temperature sensor has then been re-glued at the same position on the bottom sensor with less encapsulant. This process has been successful and later measurements have shown that this has not left any significant damage to the silicon sensor. After the re-gluing of the temperature sensor on the bottom sensor the 2S module has been successfully integrated onto the cooling structure. It has been placed onto the inserts of the middle position by hand and screwed to the six inserts with the dedicated M1.6 screws and washers made out of brass using a torque of 10 cNm. The same screw and washer have also been used for the measurements with the stump bridge in Section 7.2.

The cables of the temperature sensors have been fixed in bundles on the surface of the cooling structure with kapton tape and are routed out of the box through the holes at the right and left side of the module cooling box. They are read out by a Keithley Multimeter 2701 [43]. The high voltage of the module for the silicon sensors is supplied by a Keithley 2410 SourceMeter [61] while the low voltage circuit is connected to a Hameg HMP 4040 power supply [60].

7.3.1 Measurement of the Noise

After the integration of the 2S module on the mini-TEDD structure the noise has been measured inside the module cooling box at room temperature. For the readout of the module the VTRx+ is connected via two optical fibers to an FC7 [64], which is an Advanced Mezzanine Card. The FC7 is a common readout board used within the CMS tracker community for testing of the 2S modules and it will also be used during the production phase of the 2S modules. The FC7 is placed in a μTCA crate and connected to a computer via ethernet. The Phase-2 Acquisition and Control Framework (Ph2 ACF) [65] developed by the CMS tracker group is used as readout software. It allows the user to perform several routines on the 2S module such as the calibration of the chips, noise scans and data readout.

The CBCs of the 2S module use an analogue front-end with a pre- and post-amplifier and a comparator to read out the individual strips of the silicon sensors with a binary hit detection. Every CBC has a global chip threshold called the V_{CTH} value. In general high V_{CTH} values correspond to low physical thresholds. A hit is generated when the measured voltage pulse of the deposited charge in the channel surpasses this threshold. This voltage pulse is modified by Gaussian noise that originates for example from electronic components. To determine a useful threshold value a scan is performed that measures the occupancy of each channel with increasing threshold value. The occupancy is defined as the number of measured noise signals divided by the total number of events. The obtained result of such a threshold scan has the form of a so-called S-curve since the occupancy increases with increasing V_{CTH} values until it reaches a value of 1.0 which is the point where all noise signals surpass the threshold. An example for such a S-curve can be found in Figure C.1 in Appendix C. This curve would be a step function in case of no Gaussian noise. The so-called pedestal value is determined at the threshold value where the occupancy yields a value of 0.5 while the noise is defined as the width of the S-curve in V_{CTH} units [66].

Overall the noise is determined during a noise scan where the S-curve of each channel is measured and then fitted to determine the width of the curve. Before each noise measurement a calibration is performed per chip so that channel to channel threshold differences are corrected by adjusting an offset value for each channel. For the successful operation of the 2S module the noise has to be kept as low as possible, currently a value of around 6 V_{CTH} units is targeted.

In this setup in the module cooling box the ground level of the low and high voltage circuit is connected to the ground of the used Hameg power supply. Additionally the cooling pipe of the mini-TEDD structure is grounded via a cable connection to this level as well as all inserts of the middle position since they are electrically connected to the cooling pipe. In Figure 7.5 the result of a noise scan performed with the 2S module mounted to the cooling structure inside the cooling box at room temperature can be seen.

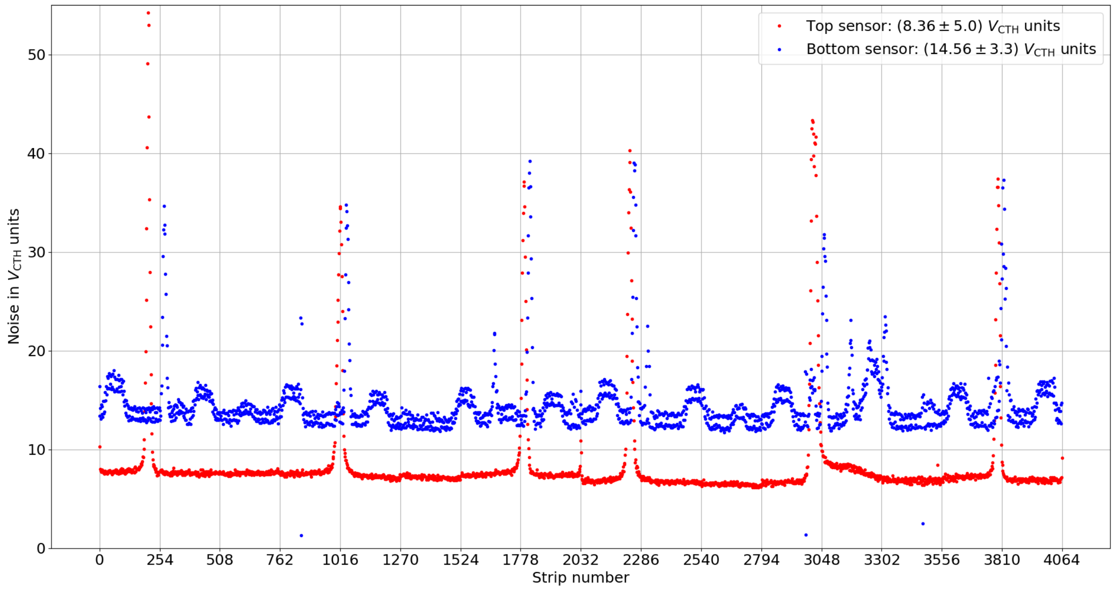

Figure 7.5: Noise distribution per strip of the 2S module mounted on the cooling structure inside the module cooling box measured at room temperature. The measured values for the strips of the top sensor are shown in red while the values of the strips of the bottom sensor are shown in blue.

It shows the noise distribution per strip using the strip numbering as explained in the following. The readout of the module starts, when using the orientation of the module as shown in Figure 7.4, at the right FEH with the strips of the CBC that is the furthest away from the SEH side of the module. The strips of the top and bottom sensor are read out alternately so that the odd numbered strips belong to the top sensor and the even numbered strips to the bottom sensor starting at strip number 0. The strip numbering then continues in the direction towards the SEH until the strip closest to the SEH, which corresponds to a strip number of 2031. The numbering then continues on the left FEH starting at the side close to the SEH and ends at strip 4063 at the far side of the left FEH. The ticks on the x-axis are chosen in such a way that it denotes the group of strips that are read out by the same CBC.

In general a flat noise distribution is expected for the 2S module as it can be seen in Figure 7.6. The plot shows the noise distribution of the 2S module before the assembly of the temperature sensors to the silicon sensors. This measurement was performed in an aluminum box that is usually used for noise measurements of 2S modules at this institute. A flat noise distribution was measured for the module as expected with a mean value of (6.96 ± 0.30) V_{CTH} units for the top sensor and a value of $7.40 \pm 0.43)$ V_{CTH} units for the bottom sensor. In general a higher noise value is expected for the bottom sensor since the channels of the bottom sensor have longer traces on the FEH than the channels of the top sensor.

In comparison to this measurement the noise distribution measured at room temperature in Figure 7.5 exhibits several peaks for the top and bottom sensor. These peaks are caused by the temperature sensors that are glued to the silicon sensors. The temperature sensors significantly increase the noise of the strips at their respective positions. Especially for the top sensor it is clearly visible that the peaks appear at strip numbers that correspond to the expected positions of the temperature sensors. Nevertheless in-between these peaks

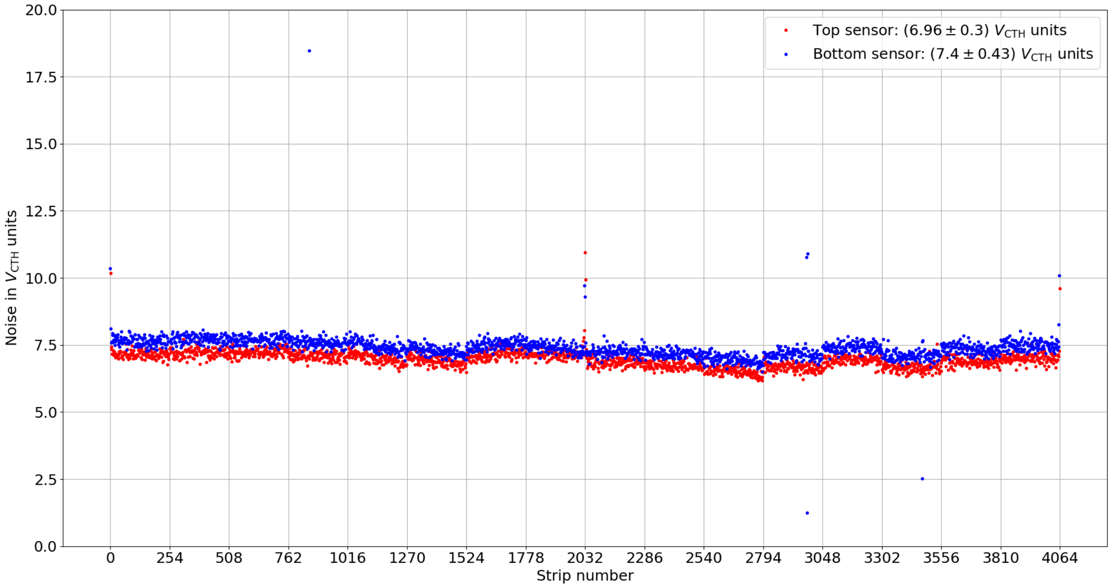

Figure 7.6: Noise distribution per strip of the 2S module placed in an aluminum box at room temperature. This noise measurement was performed before the assembly of the temperature sensors to the silicon sensors of the module. The measured values for the strips of the top sensor are shown in red while the values of the strips of the bottom sensor are shown in blue.

the top sensor exhibits a flat noise distribution within acceptable noise values so that it can be concluded that the glued temperature sensors only partially affect the electrical performance at their respective position on the sensor and do not restrict the overall usability of the other sensor areas of the module.

However the bottom sensor exhibits several peaks additionally to the peaks of the temperature sensors, located in-between these temperature sensor peaks. Per hybrid six of those peaks can be observed. The origin of these peaks can be attributed to the LEDs on the LED strips that are glued to the cooling structure underneath the bottom sensor. In total there are two LED strips with six LEDs each that illuminate one sensor half respectively. The locations of these LEDs correspond to the positions of the observed peaks in the noise distribution. This ultimately shows that the LEDs additionally inject noise in the bottom sensor. The noise of the top sensor is not affected by the LEDs since the strips have a larger distance to the top sensor when the lid of the module cooling box is closed.

For the top sensor the noise distribution yields a mean value of (8.36 ± 5.00) V_{CTH} units and a value of $14.56 \pm 3.30)$ V_{CTH} units is measured for the bottom sensor. The mean values have been calculated with the noise values of all strips of the respective sensor.

8 Thermal Measurements with the 2S Module

Within this thesis several measurements of a CO_2 cooled 2S module equipped with temperature sensors on a mini-TEDD structure have been performed. The use of LED strips to emulate a leakage current in the unirradiated silicon sensors of the used module in the setup allows to adjust the power consumption according to several radiation scenarios that are possible at the HL-LHC. The temperature distributions on the module for three radiation scenarios at the nominal expected CO_2 temperature have been measured as well as the thermal runaway for one scenario. Additionally thermal simulations of the 2S module have been performed in this working group by Nicolas Röwert in the scope of his ongoing doctorate. The performed simulations can be compared to the measurements executed in this thesis. The possible scenarios at the HL-LHC, the measurement concept as well as the results of the thermal measurements and the comparison with the simulation will be discussed in the following sections.

8.1 Possible Scenarios for the Operation at the HL-LHC

The capabilities of the cooling system significantly influence the longevity of the 2S modules in the Phase-2 tracker. To assess the thermal properties of the 2S module and the cooling structure at the planned end three possible radiation and operation scenarios at the HL-LHC are under investigation. Important parameters within these scenarios are the expected fluence depending on the location of the module in the detector, the bias voltage of the silicon sensors and the radiation damage constant for silicon since the power consumption of the silicon sensors depends on these values according to Equation 4.5.
The used 2S module has a sensor spacing of 4.0 mm so that the scenarios for the measurements have been chosen with the intention to investigate the worst 4.0 mm 2S module regarding the cooling conditions in the detector. This corresponds to the module that is exposed to the highest fluence in the TEDD region of the Phase-2 tracker. These would be the 2S modules that are located in the TEDD 2 on ring 11 of disk 3 with an estimated fluence of $3.73 \cdot 10^{14}\,\mathrm{n_{eq}/cm^2}$ for an operation scenario at the HL-LHC after $3000\,\mathrm{fb^{-1}}$ [67]. Figure 8.1 shows an overview of one quarter of the Phase-2 tracker with the corresponding location of the 2S module encircled in red.

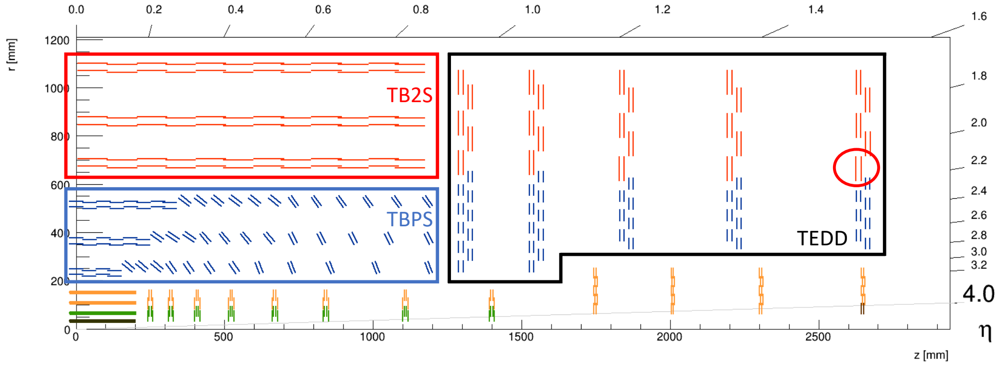

Figure 8.1: Sketched overview of one quarter of the new CMS Phase-2 Tracker. The 2S modules of the Outer Tracker are depicted in red. The encircled module marks the position (TEDD 2, ring 11, disk 3) of the worst 4.0 mm 2S module in the detector regarding the cooling as a result of the expected fluence. Modified from Ref. [14].

With a bias voltage of 600 V for the silicon sensors and an estimated radiation damage constant of $4.28 \cdot 10^{-17}$ A/cm [67] for 3000 fb^{-1} this is defined as the nominal scenario. For an ultimate performance of the HL-LHC with 4000 fb^{-1} the fluence would increase by 33 % to a value of $4.96 \cdot 10^{14}\,\mathrm{n_{eq}/cm^2}$. This is referred to as the Ultimate@600V scenario. A possible third scenario after 4000 fb^{-1} with the bias voltage increased by 33 % to 800 V and a 20 % increase in the radiation damage constant to a value of $5.14 \cdot 10^{-17}$ A/cm is the so-called Ultimate@800V scenario [23]. A summary of the respective parameters for the three scenarios is provided in Table 8.1.

Scenario	Bias voltage in V	Radiation damage constant in A/cm	Fluence in $\mathrm{n_{eq}/cm^2}$
Nominal	600	$4.28 \cdot 10^{-17}$	$3.73 \cdot 10^{14}$
Ultimate@600V	600	$4.28 \cdot 10^{-17}$	$1.33 \cdot 3.73 \cdot 10^{14}$
Ultimate@800V	$1.33 \cdot 600$	$1.2 \cdot 4.28 \cdot 10^{-17}$	$1.33 \cdot 3.73 \cdot 10^{14}$

Table 8.1: Summary of the parameters and respective values that are relevant for the three possible scenarios at the HL-LHC with regard to radiation and operation at the specific module location in the detector [67, 23].

In Figure 8.2 the left plot shows the total expected leakage current for a 2S module as a function of the sensor temperature for all three scenarios, while the right plot shows the expected power consumption for both sensors as a function of the sensor temperature for the three scenarios. For the nominal scenario a leakage current of 1.57 mA is expected for a sensor temperature of −20 °C, leading to a power consumption of 0.94 W, while a leakage current of 2.08 mA leading to a power consumption of 1.25 W is expected for the Ultimate@600V scenario. The Ultimate@800V scenario yields the highest power consumption with a value of 2.00 W and a leakage current of 2.51 mA for the two sensors for a sensor temperature of −20 °C and is thus the most critical scenario for the cooling performance.

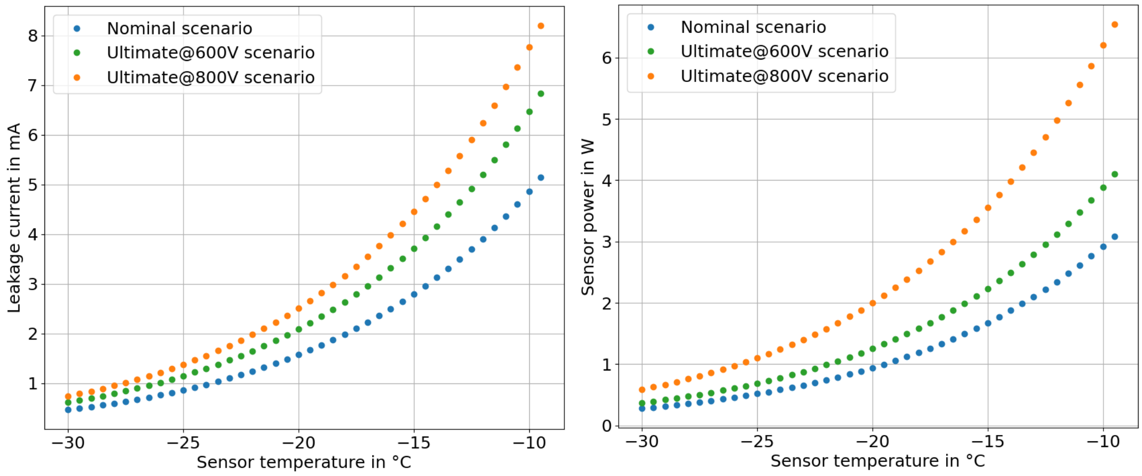

Figure 8.2: Left: expected leakage current for both silicon sensors together in dependence on the sensor temperature for all three scenarios. Right: expected sensor power for both sensors in dependence on the sensor temperature for all three scenarios. The values in both plots are specific for the considered 2S module position in the detector.

8.2 Measurements with Realistic Power Consumption for Different Scenarios at the Nominal CO_2 Temperature

The CO_2 cooling system of the Phase-2 tracker has a design temperature of −35 °C. With pressure drops along the cooling lines a CO_2 temperature of −33 °C is expected as the maximal temperature, hence this value will be referred to as the nominal operating temperature in the following. To analyze the temperature distribution on the 2S module a measurement has been performed for each of the three scenarios at the nominal CO_2 temperature. For the following measurements the CO_2 temperature has been defined as the mean value of the measured temperatures at the inlet, outlet and U-turn of the cooling pipe inside the mini-TEDD structure. The mean sensor temperature is determined by the mean value of the temperature values measured by all 14 temperature sensors that are glued to the silicon sensors.

For the following measurements the CO_2 has been cooled down with the CO_2 cooling system to a temperature of −33.1 °C while the module cooling box has been cooled down as low as possible. With the temperature sensor inside the module cooling box air temperatures in the range of −22 °C were measured. A small dry air flow of 4 l/min has been supplied to the module cooling box. For the measurements the pre-heating loop of the CO_2 cooling system has been used with a power load of 10 W to make sure that the CO_2 is in a two-phase state when entering the cooling structure in this setup. The CO_2 mass flow during the measurements has been set to the expected value of 1.6 g/s in the TEDD 2 region. The procedure to adjust the power consumption of the hybrids and the silicon sensors to the required values for each measured scenario will be described in the next paragraphs.

Adjustment of the Hybrid Power

Within the regular configuration routine of the 2S module the threshold values of the CBCs are chosen such that they have sufficient distance to the pedestal value so that noise signals are not falsely detected as hit signals. It has been observed that when using this normal configuration routine the power consumption of the three hybrids of the module yields a lower value of 3.92 W than the expected nominal values, given in Table 4.1. To bring the power consumption of the hybrids closer to the nominal values the thresholds of the channels in the CBCs have been set to the pedestal values at the start of each measurement. With this setting a power consumption of 4.59 W has been achieved for the hybrids, which is as close to the expected nominal values as possible within the performed measurements.

Procedure for the Regulation of the Sensor Power

When cooling a 2S module with irradiated sensors the power load on the sensors automatically arises depending on the sensor temperature according to Equation 4.5. To emulate this behavior the current generated with the LED strips in the unirradiated sensors of the used 2S module has to be regulated until the measured mean sensor temperature and the power load of the sensors satisfy the power equation. When this condition is met a proper working point has been achieved. To realize this working point in the measurements the PID control described in Section 6.4.1 is used to generate a specific power load in the silicon sensors that corresponds to a mean sensor temperature based on the power equation. The mean sensor temperature of the 2S module is then determined by a LabView program that measures the sensor temperatures and calculates the mean value. By changing the applied power load on the sensors in an iterative process the working point can be found when the applied power load and the measured mean sensor temperature fulfill the power equation. In practice around three to four iterations are necessary to find the working point during the measurement. By using the different parameters of Table 8.1 corresponding to the desired scenario for the power equation all three radiation and operation scenarios can be measured.

Results of the Measurements for the Three Scenarios

For the measurement of the temperature distribution on the 2S module the previously explained measurement procedure has been applied to find the working point for each of the three scenarios at the nominal CO_2 temperature. For the nominal scenario the working point at the nominal operating temperature was found for a mean sensor temperature of $-27.4\,°C$ and a total sensor power of 0.38 W. An overview of the mean values of all measured temperatures on the 2S module during the measurement of the working point for the nominal scenario can be found in Figure 8.3. A heat map of the front and backside of the module is shown, and each circle represents the location of the respective temperature sensor on the module. The individual temperature values are depicted by the colors of the circles that are color-coded according to the given color bar, whereas the exact measured values are also given next to each dot.

For the nominal scenario a mean sensor temperature of $-27.0\,°C$ has been measured for the top sensor while a mean temperature of $-27.7\,°C$ has been measured for the bottom sensor. In general a homogeneous temperature distribution can be observed on the silicon sensors with deviations along the sensor within 1 K. Additionally a small influence of the power load of the hybrids on the temperature distribution on the silicon sensors can be recognized since the temperature measured on the silicon sensor next to the DC-DC converters is the warmest point for both sensors, while the temperatures measured on the sensors at the SEH far side of the module are the coldest points.

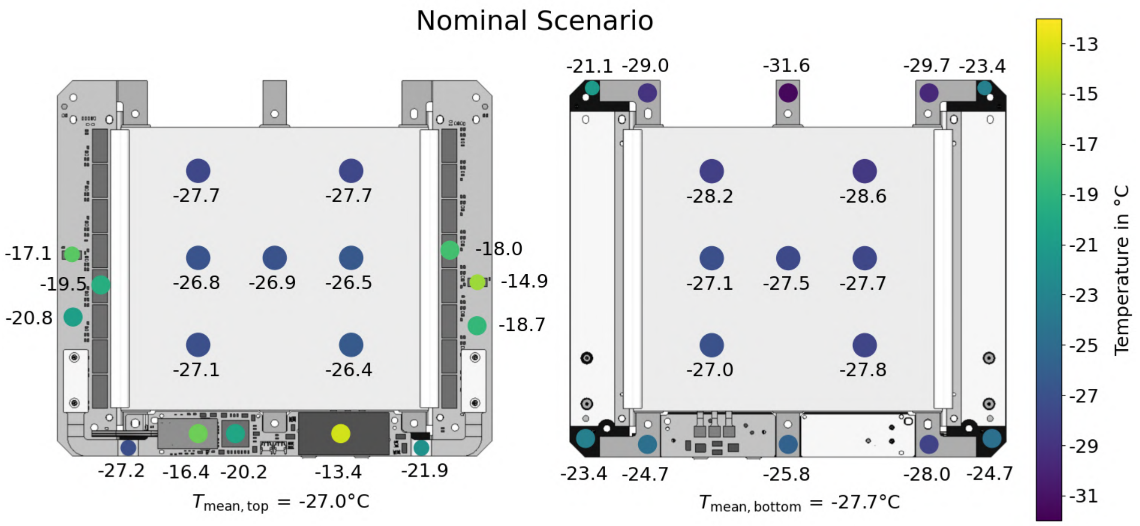

Figure 8.3: Overview of the measured temperatures on the 2S module for the nominal scenario at a CO_2 temperature of $-33.1\,°C$ with an air temperature of $-22.6\,°C$ inside the module cooling box. A heat map for the top side of the module is shown on the left, while the temperatures measured on the bottom side are shown on the right. A mean sensor temperature of $-27.4\,°C$ was measured at a sensor power of 0.38 W and a hybrid power of 4.59 W.

The temperatures measured on the three hybrids have a broader spread. The CBCs and CICs on the FEHs have higher temperatures than the measurement directly on the surface of the FEH on the top or bottom side. This is also valid for the SEH where the measured temperatures on the VTRx+, the LpGBT and the DC-DC converters are about 5 K higher than the temperature measured on the carbon support plate of the SEH under the tails of the SEH. Overall this is an expected behavior since the active components produce the heat load that has to be removed. The temperature measured on the shield of the DC-DC converters is the hottest point with −13.4 °C, which is expected since the converters alone produce a heat load of around 2 W. In general the right FEH is also warmer than the left side. This is caused by the asymmetric power distribution on the SEH induced by the DC-DC converters.

The results for the measurements of the Ultimate@600V and Ultimate@800V scenario can be found in Figures 8.4 and 8.5, where the respective heat maps of the 2S module are shown. For the Ultimate@600V scenario the working point at the nominal operating temperature has been found for a mean sensor temperature of −27.0 °C and a total sensor power of 0.54 W, with a mean temperature of −26.7 °C for the top and −27.4 °C for the bottom sensor. For the Ultimate@800V scenario the working point has been obtained at a mean sensor temperature of −26.2 °C and a sensor power of 0.95 W. For the top sensor a mean temperature of −25.8 °C and for the bottom sensor a mean temperature of −26.6 °C has been measured.

In general the temperature distributions on the 2S module for these two scenarios are qualitatively similar to the observations made for the nominal scenario. Nevertheless the temperatures on the 2S module generally rise with the higher demands of the scenarios since the power consumption of the sensors increases respectively. A detailed analysis of the different thermal interfaces within the 2S module and the cooling structure will follow in the next section.

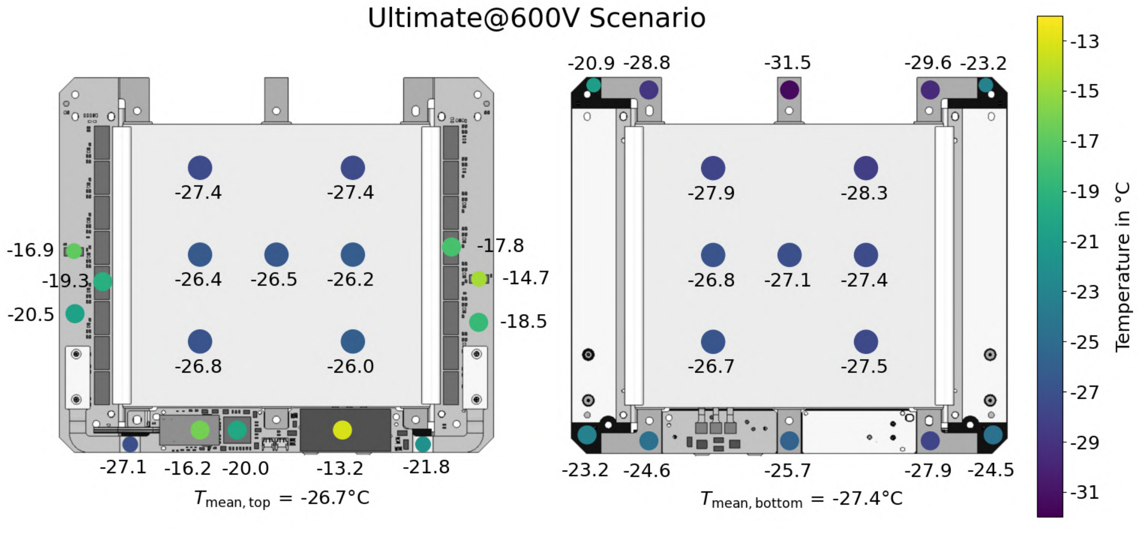

Figure 8.4: Overview of the measured temperatures on the 2S module for the Ultimate@600V scenario at a CO_2 temperature of −33.1 °C with an air temperature of −22.2 °C inside the module cooling box. A heat map for the top side of the module is shown on the left, while the temperatures measured on the bottom side are shown on the right. A mean sensor temperature of −27.0 °C was measured at a sensor power of 0.54 W and a hybrid power of 4.60 W.

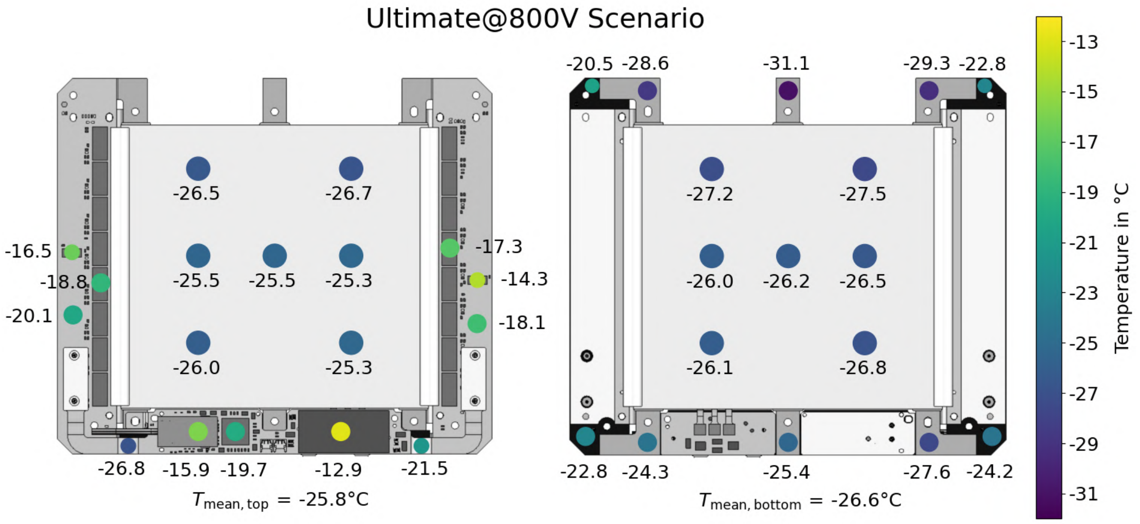

Figure 8.5: Overview of the measured temperatures on the 2S module for the Ultimate@800V scenario at a CO_2 temperature of $-33.1\,°C$ with an air temperature of $-22.1\,°C$ inside the module cooling box. A heat map for the top side of the module is shown on the left, while the temperatures measured on the bottom side are shown on the right. A mean sensor temperature of $-26.2\,°C$ was measured at a sensor power of 0.95 W and a hybrid power of 4.59 W.

8.2.1 Analysis of the Thermal Interfaces

In this section the thermal interfaces of the 2S module are analyzed on the basis of the measurement for the nominal scenario. In the left plot in Figure 8.6 the averaged temperatures for each area of the 2S module are shown with the error bars depicting the deviation of the temperature within an area. The CO_2 temperature is referred to as 'pipe' in this plot. It can be observed that the temperature rises along the path of the heat load, as expected.

The right plot in Figure 8.6 shows the individual temperatures measured by all sensors inside the cooling structure, i. e. the temperatures of the inserts of the middle positions and the cooling pipe, for the nominal scenario. In this plot the sensor numbers are arranged in the order of the CO_2 flow direction along the cooling pipe. The cooling pipe temperature is measured by sensor number 3, 2 and 1 at the inlet, U-turn and outlet of the pipe, respectively, shown in blue. The measured temperatures show that the CO_2 temperature in general is constant within the cooling structure with a slight decrease at the outlet of the cooling pipe. This is consistent with the expected pressure decrease for two-phase CO_2 at the end of the pipe. Sensors 9, 8, 7, 6, 5 and 4 are measuring the temperatures of the top inserts depicted in red. The top inserts exhibit higher temperatures than the remaining sensors that measure the temperatures of the bottom inserts, shown in green, because of the power load of the module. Since the bottom inserts are placed between the top inserts along the cooling line they are also slightly affected by the heat load at the middle position so that the temperatures of the bottom inserts are in-between the top inserts and the measured CO_2 temperature.

Since the removal of the heat load of the silicon sensors is crucial in case of the 2S module the different interfaces between the CO_2 and the silicon sensors are analyzed in more detail. For this the temperature differences between the individual interfaces along the path of the sensor heat flux have been determined. This includes the temperature difference between

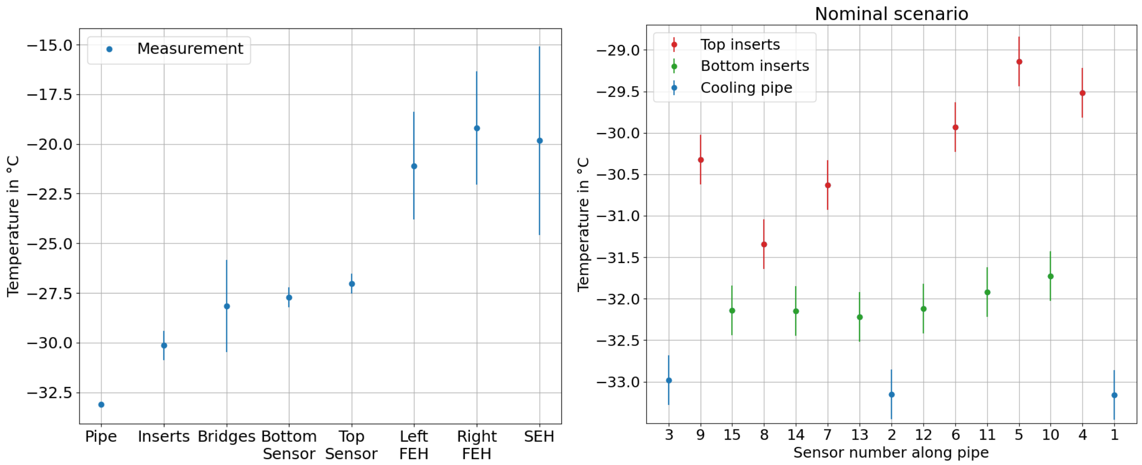

Figure 8.6: Left: averaged temperatures of the different areas of the 2S module during the measurement of the nominal scenario at the nominal CO_2 temperature. The error bars depict the deviation between the components of the individual areas. Right: mean measured values of the insert and cooling pipe temperatures during the measurement of the nominal scenario. The temperature sensors are ordered along the CO_2 flow direction through the cooling pipe.

the mean sensor temperature and the individual temperatures of the six AlCF bridges, the difference between the bridge and its respective insert temperature and the difference between the inserts and the cooling pipe. The left plot in Figure 8.7 shows the determined temperature differences for each interface for the nominal scenario. The color code used in this plot is illustrated in the right picture in Figure 8.7. The AlCF bridges are numbered according to its respective insert with an individual color and symbol for each bridge. For each temperature measurement an uncertainty of 0.3 K has been assumed, which leads to a combined uncertainty of 0.6 K for each temperature difference. Overall the determined temperature differences between the sensor and the bridges as well as between the bridges and the inserts are in a range of 2 K. For the interface between the inserts and the pipes a

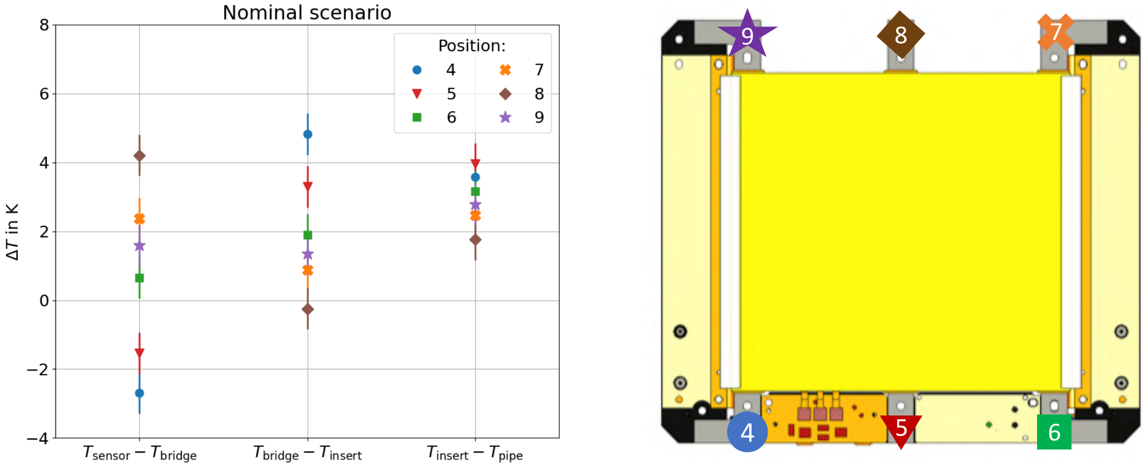

Figure 8.7: Left: temperature differences for three thermal interfaces of the 2S module for the measurement of the nominal scenario. The temperature differences are determined for each bridge/insert position. Right: illustration of the numbering and color code used for the six AlCF bridges shown on the backside of the 2S module.

slightly higher difference in the order of 3 K can be observed for the nominal scenario. With a closer look to the individual temperature differences in the left plot in Figure 8.7 it can be seen that bridge 4 and 5 exhibit a higher temperature than the measured mean sensor temperature, meaning that there is no heat flux from the sensors to these bridges. But these two bridges nevertheless transport a heat load to the inserts since it can be seen that they have the highest temperature distance to their respective insert. Based on this one can conclude that for low sensor powers the bridges 4 and 5 next to the DC-DC converters only remove heat load from the SEH.
Also noticeable in this plot is the negative temperature difference of position 8 for the interface between the bridge and the insert. This would mean that bridge 8 is colder than its respective insert which is physically not possible. Within the measurement uncertainty this temperature difference is compatible with 0 K, which would indicate that nevertheless there is no heat flux from the bridge to the insert. Within the characterization measurements of the setup all inserts of the middle position have been tested without any distinctive features so that it is also not possible that the insert has insufficient contact to the cooling pipe so that it would adapt to the temperature of the bridge. To investigate this further two other measurements are analyzed: a measurement of the 2S module in a not powered state at the nominal CO_2 temperature and a measurement with a high sensor power performed for the measurement of the thermal runaway of the Ultimate@800V scenario that will follow in Section 8.3.
The data for the measurement with an unpowered module have been recorded before the module was powered on for the measurement of the nominal scenario, which means that this measurement was also taken at a CO_2 temperature of $-33.1\,°\mathrm{C}$. Since the ambient temperature during this measurement is at $-22.6\,°\mathrm{C}$ there is still a small heat flux from the ambient to the 2S module even if the module itself is not powered. Figure 8.8 shows an overview of the temperature distribution of the 2S module during that measurement. It can be observed that the whole module is at an average temperature of around $-32\,°\mathrm{C}$.

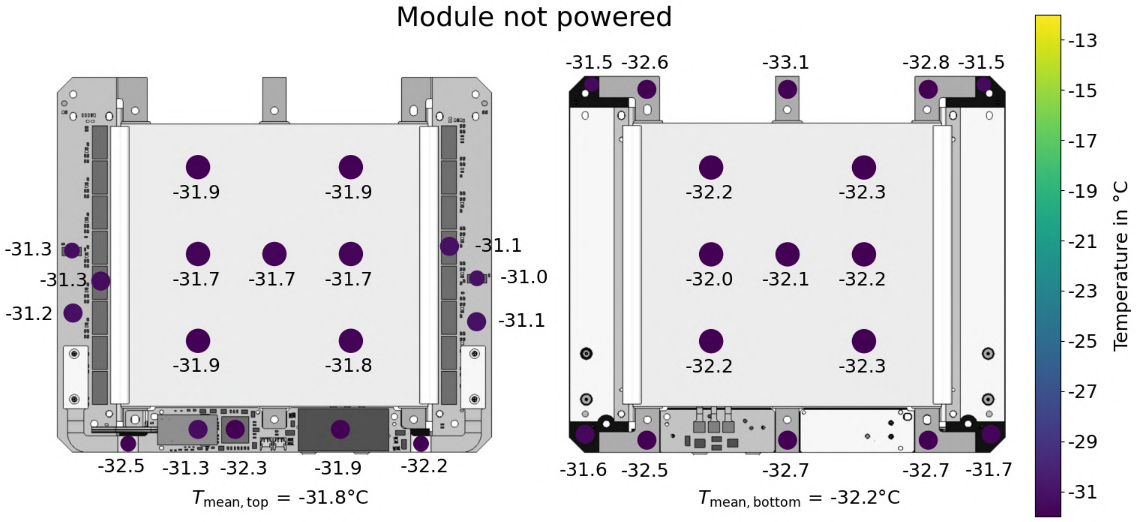

Figure 8.8: Overview of the temperature distribution on the 2S module in a state where the module is not powered but cooled with the nominal CO_2 temperature of $-33.1\,°\mathrm{C}$. A heat map for the top side of the module is shown on the left, while the temperatures measured on the bottom side are shown on the right. The ambient temperature is at $-22.6\,°\mathrm{C}$.

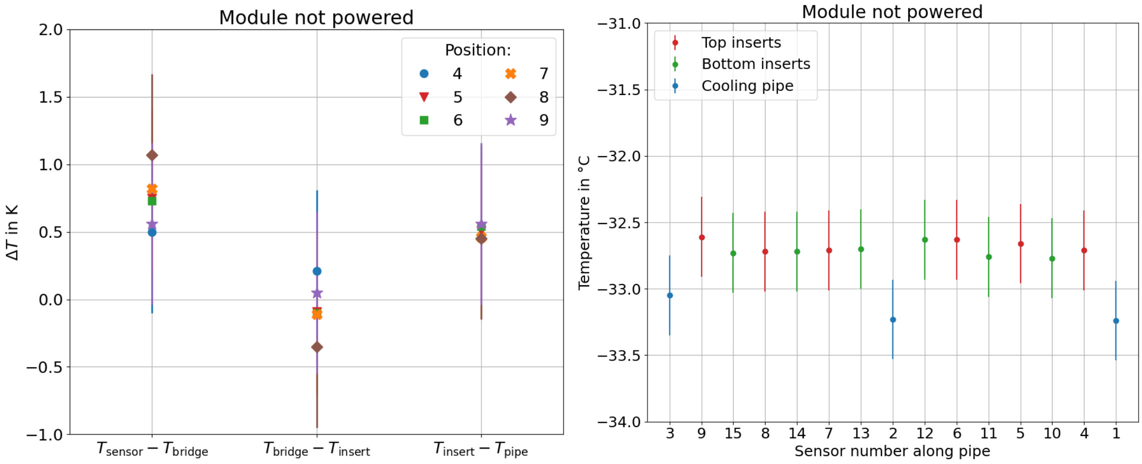

Figure 8.9: Left: temperature differences of the three thermal interfaces for the measurement with an unpowered module at −33.1 °C. Right: overview of the measured mean temperatures for the inserts and the cooling pipe during that measurement.

The left plot in Figure 8.9 shows the temperature differences for the thermal interfaces for this measurement, while the right plot shows the measured insert and cooling pipe temperatures. It is visible that the mean sensor temperature is around 0.8 K higher than the bridges as well as the inserts that are around 0.5 K warmer than the measured CO_2 temperature. This is a result of the small heat flux from the ambient to the module and the inserts.

When looking at the temperature difference between the bridge and the insert of position 8 a difference of −0.4 K can be observed. Given that this position exhibits such an offset even at no sensor power it can be concluded that there is still a small heat flux from the bridge to the insert at small sensor powers such as in the measured nominal scenario. This measurement with no module power also shows that the temperature difference between the sensor and bridge 4 and 5 is in the same range as for the other positions in case of a symmetric heat load distribution on the silicon sensors coming from the ambient. This reassures the earlier observation that in case of asymmetric heat loads with low sensor powers compared to the hybrid power only the heat load of the hybrids is removed through these points.

To investigate the thermal interfaces for a case with a high sensor power a measurement that has been performed for the measurement of the thermal runaway for the Ultimate@800V scenario is analyzed. For this measurement the working point has been found at a mean sensor temperature of −13.0 °C and a sensor power of 4.51 W at a CO_2 temperature of −26.0 °C. The air temperature inside the module cooling box was at −13.0 °C so that the silicon sensors are in thermal equilibrium with the ambient. For the hybrids a power of 4.63 W has been measured. Figure 8.10 shows an overview of the temperature distribution on the 2S module during that measurement. A broader distribution of the temperature on the sensors can be observed with the temperatures being within a range of 3 K.

The left plot in Figure 8.11 shows the temperature differences for the three interfaces, while the right plot shows the overview of the measured insert and cooling pipe temperatures. In general higher temperature differences for all interfaces in comparison to the nominal scenario can be seen. The temperature difference between the sensor and the bridges is in the order of 5 K as well as the difference between the inserts and the cooling pipe. For the bridges and the inserts the temperature differences are in a range of 5 K.

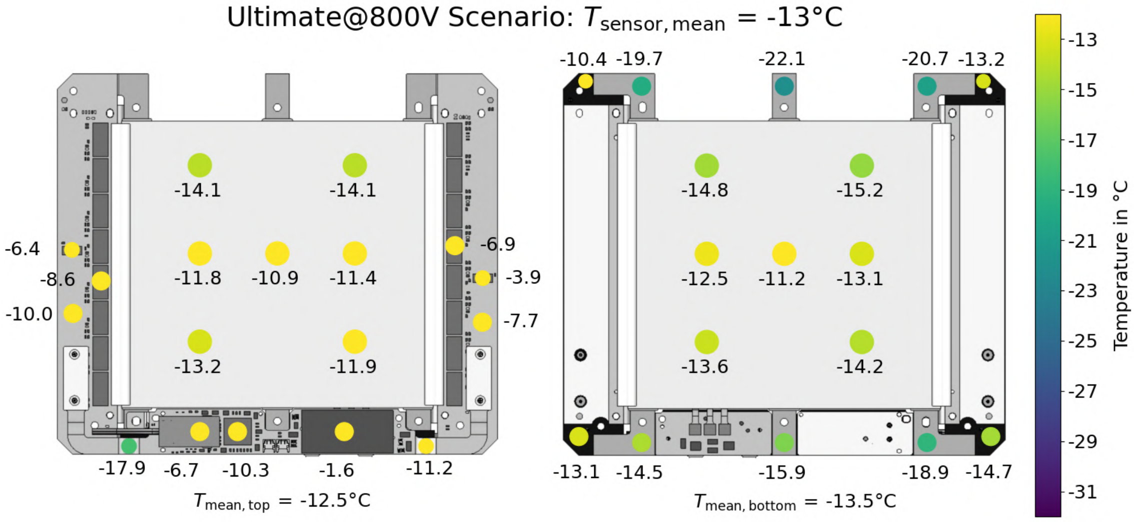

Figure 8.10: Overview of the temperature distribution of the 2S module for a measurement at a CO_2 temperature of $-26.0\,°C$ with a mean sensor temperature of $-13.0\,°C$ and a sensor power of 4.51 W. A heat map for the top side of the module is shown on the left, while the temperatures measured on the bottom side are shown on the right. The ambient temperature was at $-13.0\,°C$ while a hybrid power of 4.63 W was measured.

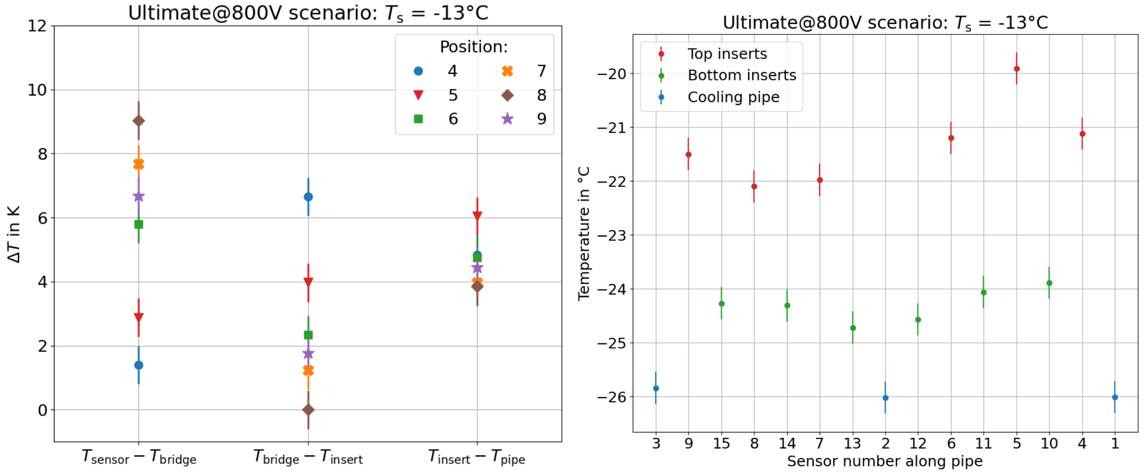

Figure 8.11: Left: temperature differences of the three thermal interfaces for the measurement with a sensor power of 4.51 W. Right: overview of the measured insert and cooling pipe temperatures during that measurement.

In comparison with the previously discussed measurements with low and no sensor power for this measurement with a high sensor power no negative temperature differences can be observed for all positions and interfaces. This means in conclusion that for a high sensor power the heat load of the sensors is also partly removed by the bridges of position 4 and 5 in addition to the heat load of the SEH.

Also the determined temperature difference of 0 K between the bridge and the insert for position 8 indicates that with respect to the measured offset at no module power the removed sensor heat load at this position increases. This is also visible in the right plot of Figure 8.11 where it can be seen that the temperature of insert 8 has increased while the other inserts exhibit a qualitatively similar behavior in comparison with the measured temperatures of the nominal scenario.

8.2.2 Comparison with a Thermal Simulation

In this working group also thermal simulations of the 2S module have been performed by Nicolas Röwert that can be used for comparison with the measurements. For the simulations a thermal model of the 2S module based on a Finite Volume Method (FVM) that had been previously used in the CMS tracker group [68] has been modified to meet the specifications of the setup. The inserts of the thermal model have been updated to the insert type in the cooling structure used for the measurements by adjusting the thermal conductivity in the model. Also the glue layer thickness between the kapton strips and the silicon sensors has been decreased based on the measured height profile of the used 2S module. The thermal simulations themselves have been performed by using the simulation software ANSYS [69].

The thermal simulation has been performed at a CO_2 temperature of $-33\,^\circ\mathrm{C}$. The CO_2 temperature is implemented in the simulation by setting the inner surface of the cooling pipe to the CO_2 temperature. The power load of the sensors was chosen to match the measured sensor power during the measurement of the nominal scenario so that the temperature distributions of the 2S module can be compared between the measurement and the simulation. Therefore a fixed power load of 0.38 W has been applied to the silicon sensors equally distributed among the two sensors. The heat load of the three hybrids has also been scaled to match the measured power consumption of 4.59 W. The resulting temperature distribution on the thermal model of the 2S module can be seen in Figure 8.12. An overview of the temperature values of several components in the measurement as well as in the simulation and the respective temperature difference is given in Table 8.2. For the top and bottom sensor and the bridges the temperature values refer to mean values. The temperature difference is formed by subtracting the simulated values from the measured ones.

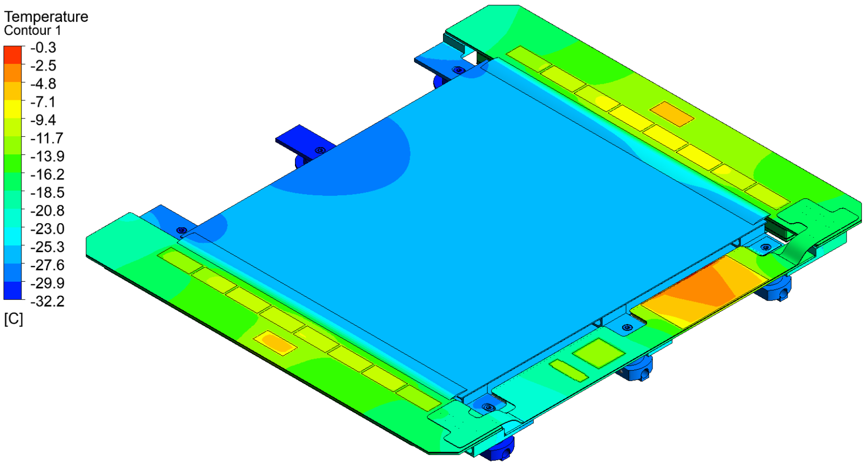

Figure 8.12: Results of the temperature distribution for the simulation of the thermal model of the 2S module. The simulation has been performed at a CO_2 temperature of $-33\,^\circ\mathrm{C}$ with a fixed sensor power of 0.38 W and a scaled hybrid power of 4.59 W [70].

When comparing the values for the top and bottom sensor and the bridges it can be observed that the temperatures match well with a maximal deviation of 1.5 K with the simulation being warmer than the measurement. It has to be noted that the thermal simulation is performed with the assumption that there is no heat exchange with the ambient while in the measurement there is a small heat flux from the ambient to the sensors because of the temperature difference. This means that the measured sensor temperatures would be even colder in case of a thermal equilibrium with the ambient.

When comparing the measured temperatures of the electronic components it is apparent that the simulation exhibits higher temperature values for all components with deviations in the range of 10 K. This is a result of the simplified modeling of the electronic components in the simulation since the thermal model only considers them as surfaces on the hybrids with an assigned power load. This leads to an overestimation of the temperatures in the simulation. But since the thermal model of the 2S module has been mainly designed to focus on the modeling of the temperature-dependent sensor current it can be concluded that this comparison shows that the simulated sensor temperature can be used as a good estimate for the sensor temperature.

Component	Measured T in °C	Simulated T in °C	Temperature difference in K
Top sensor	-27.0	-26.5	-0.5
Bottom sensor	-27.7	-26.5	-1.2
Bridges	-28.1	-26.5	-1.6
Left CIC	-17.1	-7.7	-9.4
Left CBC	-19.5	-10.0	-9.5
Right CIC	-14.9	-6.6	-8.3
Right CBC	-18.0	-9.0	-9.0
DC-DC converter	-13.4	-5.3	-8.1
VTRx+	-16.4	-13.4	-3.0
LpGBT	-20.2	-14.0	-6.2

Table 8.2: Overview of the measured and simulated temperature values for several components of the 2S module as well as the temperature differences. The values for the top and bottom sensor and the bridges refer to mean values of the component. The temperature difference is calculated by substracting the simulated temperature values from the measured values.

8.3 Thermal Runaway for the Ultimate at 800V Scenario

For the measurement of the thermal runaway the Ultimate@800V scenario has been chosen to estimate the CO_2 temperature at which the 2S module undergoes the thermal runaway. For this a specific procedure has been applied to find the working point of the silicon sensors at different CO_2 temperatures that allows the adjustment of the ambient temperature to the mean sensor temperature more easily for each measurement point. Additionally a simulation of the thermal runaway has been performed by Nicolas Röwert that can be compared to the measurement. The following sections will provide a detailed explanation of the general measurement concept, the results of the measurement and a comparison with the thermal simulation.

8.3.1 General Concept of the Measurement

The aim of the thermal runaway measurement is to determine the CO_2 temperature at which the 2S module enters an uncontrolled self-heating loop to evaluate if sufficient margin is given for the operation at the nominal CO_2 temperature. To achieve this the CO_2 temperature inside the cooling structure has to be increased until this point is reached. In the used setup the sensor power and temperature have to be regulated for each CO_2 temperature so that the power equation is fulfilled for the silicon sensors.

A possible measurement procedure could be to iterate through different CO_2 temperatures and to regulate the sensor power with the LED strips according to the method used for the measurements in Section 8.2. Since the basic idea of the setup with the module cooling box is to set the ambient temperature inside the box to the mean sensor temperature in order to minimize the heat exchange between the ambient and the sensors, the temperature of the box would also have to be adjusted within the process of finding the correct working point. Because of the volume of the module cooling box it takes a long time to reach a stable temperature inside the box so that this method is not applicable. This is why another measurement concept is used to find the working point of the 2S module for different CO_2 temperatures.

For the method in Section 8.2 the sensor power was varied at a fixed CO_2 temperature until the measured sensor temperature matched the power equation. The basic idea of the concept for the measurement of the thermal runaway is to set the sensor power to a certain fixed value with the use of the LED strips and find the working point by iterating through several CO_2 temperatures until the matching sensor temperature according to the power equation is reached. By iterating through different sensor temperatures the CO_2 temperature at which the thermal runaway occurs can then be found. This approach also allows the adjustment of the ambient temperature more easily to the sensor temperature.

The detailed procedure works as follows: the PID control is used to generate a specific current in the silicon sensors that corresponds to a mean sensor temperature. This will be the target sensor temperature for this measurement point that has to be reached by adjusting the CO_2 temperature. The temperature of the module cooling box is then adjusted so that the ambient temperature is equal to the target sensor temperature.

It has to be noted that only ambient temperatures down to $-23\,^{\circ}\mathrm{C}$ can be reached inside the module cooling box so that for sensor temperatures below that a small heat exchange with the ambient occurs. But for sensor temperatures above or equal to this value, the ambient temperature can be adjusted to match the sensor temperature. After setting the sensor power the CO_2 temperature is adjusted using the CO_2 cooling system until the actual measured mean sensor temperature matches the desired target sensor temperature. At this point a stable working point has been reached that fulfills the power equation for the silicon sensors. This procedure is repeated for several sensor temperatures until unstable cooling conditions are found which means that it is not possible to find a CO_2 temperature for the target sensor temperature that can provide stable cooling conditions. When these circumstances are found one has arrived at the point of thermal runaway.

To illustrate this a simplified excerpt from the measurement can be found in Figure 8.13. It shows the measured mean temperature of the cooling pipe, of both sensors and the ambient during the process of finding the working point. The individual steps are marked with numbers in the plot. Starting at step 1 the ambient temperature is set to the target sensor temperature. In step 2 the module is powered, configured and the chip thresholds are set to the pedestal values to maximize the power consumption of the hybrids. In step 3 the LED strips are turned on to generate a sensor power according to the target sensor

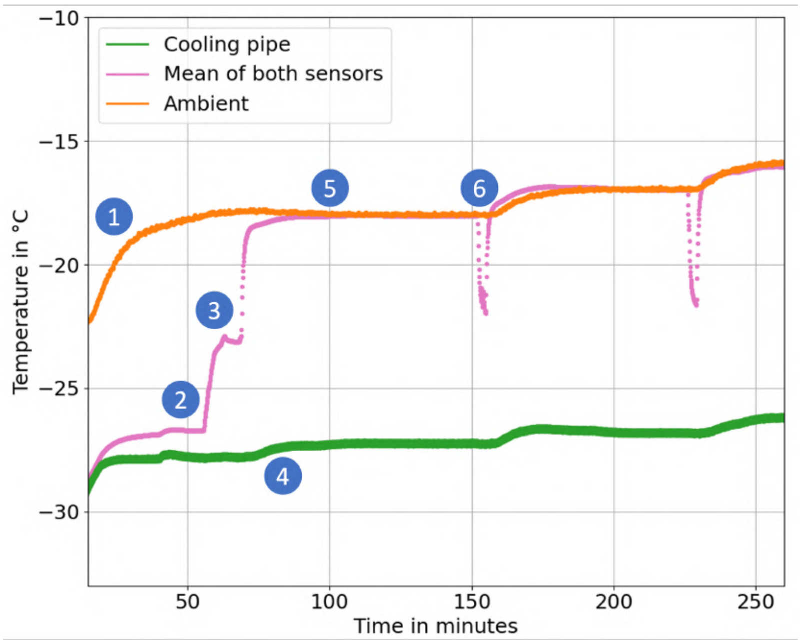

Figure 8.13: Simplified excerpt from the measurement of the thermal runaway for the Ultimate@800V scenario. The plot shows the mean temperatures of the cooling pipe, both sensors and the ambient over time. Individual steps of the measurement procedure to find the working point are numbered.

temperature. Step 4 shows the regulation of the CO_2 temperature until the target sensor temperature is reached. Step 5 denotes the point at which stable measurement conditions are reached and the working point is achieved. This point resembles one measurement point within the measurement of the thermal runaway. At step 6 the LEDs are turned off and on again to regulate the sensor power according to the next desired target temperature. At this point the overall procedure starts again.

8.3.2 Measurement of the Thermal Runaway

For the measurement of the thermal runaway the previously explained measurement concept has been applied until the point of thermal runaway was reached. For the whole measurement a power load of 10 W has been applied to the pre-heating loop of the CO_2 cooling system. The dry air flow into the module cooling box was kept as low as possible at a flow of 4 l/min, while the CO_2 mass flow was regulated during the measurement to the expected value of 1.6 g/s for the TEDD 2. The ambient temperature was adjusted to the mean sensor temperature when possible. For sensor temperatures below −23 °C the module cooling box could not be adjusted accordingly and was therefore kept at its minimal temperature of −23 °C.

Results of the Measurement

For the measurement the sensor temperature is defined as the mean value of the measured temperatures of all 14 temperature sensors that are glued to the top and bottom sensor. For now the CO_2 temperature is defined as the mean value of the measured temperatures at the inlet, outlet and U-turn of the cooling pipe inside the cooling structure.
The left plot in Figure 8.14 shows the measured sensor temperature for each measurement

point against the measured CO_2 temperature for the Ultimate@800V scenario in orange. The measurement of the nominal and Ultimate@600V scenario at the nominal operating temperature can also be found in this plot for comparison as well as the measured ambient temperature inside the module cooling box for each measurement point. In general it can be observed that the sensor temperature rises steadily with increasing CO_2 temperature until it reaches the point of thermal runaway at a CO_2 temperature of $-26\,°\mathrm{C}$. This confirms that the used measurement method generally works. It can also be seen that the ambient temperature is at around $-23\,°\mathrm{C}$ for sensor temperatures below $-23\,°\mathrm{C}$ and matches the measured sensor temperature for equal or higher temperatures. This is why the data points of the measured sensor temperature are overlapping the measured data points of the ambient temperature in this region. The fluctuation of the ambient temperatures for sensor temperatures below $-23\,°\mathrm{C}$ is a result of the different minimal achievable temperatures of the module cooling box, which differ slightly depending on the overall conditions inside the laboratory since this is at the edge of the working range of the chiller that is used to cool the module cooling box.

To investigate the thermal runaway the difference between the sensor temperature and the CO_2 temperature is plotted against the measured CO_2 temperature. With this representation the region where the difference between the sensor and the CO_2 temperature is still rather constant with increasing CO_2 temperature can be better distinguished from the region where the module slowly enters the thermal runaway. The right plot in Figure 8.14 shows the temperature difference between the sensor and the CO_2 against the measured CO_2 temperature for the measurement of the Ultimate@800V scenario as well as for the other scenarios measured at the nominal CO_2 temperature. It is visible that the temperature difference stays approximately constant until a CO_2 temperature of $-30\,°\mathrm{C}$. From this point on the difference increases exponentially until reaching the point of thermal runaway at a CO_2 temperature of $-26\,°\mathrm{C}$ where the measurement was then stopped at a mean sensor temperature of $-11\,°\mathrm{C}$.

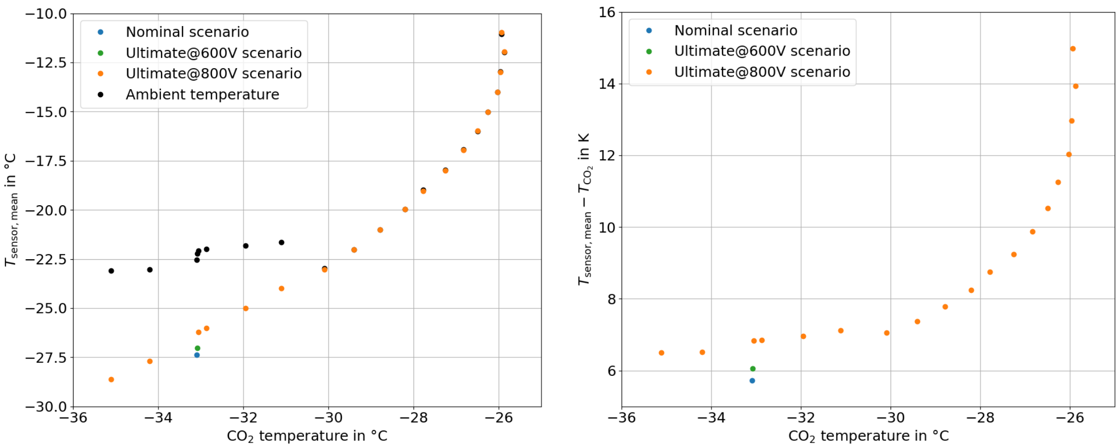

Figure 8.14: Left: measured mean sensor temperature against the measured CO_2 temperature for the Ultimate@800V scenario for the measurement of the thermal runaway in orange. The Ultimate@600V scenario (green) and the nominal scenario (blue) are also shown for the measurement at the nominal CO_2 temperature. The measured ambient temperature is shown for each measurement point in black. Right: difference between the mean measured sensor temperature and the CO_2 temperature as a function of the measured CO_2 temperature for all respective measurement points of the three scenarios.

The measurement points of the two other scenarios provide the opportunity to roughly estimate the trend of these scenarios in comparison to the Ultimate@800V scenario. It can be observed that the nominal scenario exhibits the smallest temperature difference between the sensor and the CO_2 with the Ultimate@600V scenario being in-between the other two scenarios at the nominal operating temperature. Since the radiation levels and the operating bias voltage increases from the nominal scenario to the Ultimate@800V scenario it is expected that the nominal and Ultimate@600V scenario reach the thermal runaway later at CO_2 temperatures higher than $-26\,°C$. The measured data for the nominal and Ultimate@600V scenario will also be shown in all following result plots of this paragraph. During the measurement of the thermal runaway the leakage current of the silicon sensors as well as the current in the low voltage circuit of the hybrids was measured for each measurement point. Based on this the power consumption of the sensors, the three hybrids and the full 2S module can be determined for each measurement point. In the left plot in Figure 8.15 the measured sensor power is shown against the measured mean sensor temperature. Additionally the expectation for each scenario based on the corresponding power equation is depicted in orange, green and blue respectively. For the mean sensor temperature an uncertainty of $0.3\,K$ is assumed while the uncertainty of the sensor power was determined by calculating the standard deviation of the leakage current for each measurement point and multiplying it with the applied high voltage. The uncertainty of the leakage current is in the order of $1\,\mu A$ and thus not visible within the shown power range of the plot.

Overall it can be observed that the measured data matches well with the expectation for each scenario within the uncertainties. This demonstrates that the used method to emulate the expected leakage current in the sensors as well as the general measurement procedure for the thermal runaway fulfill the requirements and have worked successfully. The right plot in Figure 8.15 displays the measured sensor power against the measured CO_2 temperature for each measurement point. The sensor power increases exponentially until the last measurement point where the thermal runaway was reached at a sensor power of $5.63\,W$.

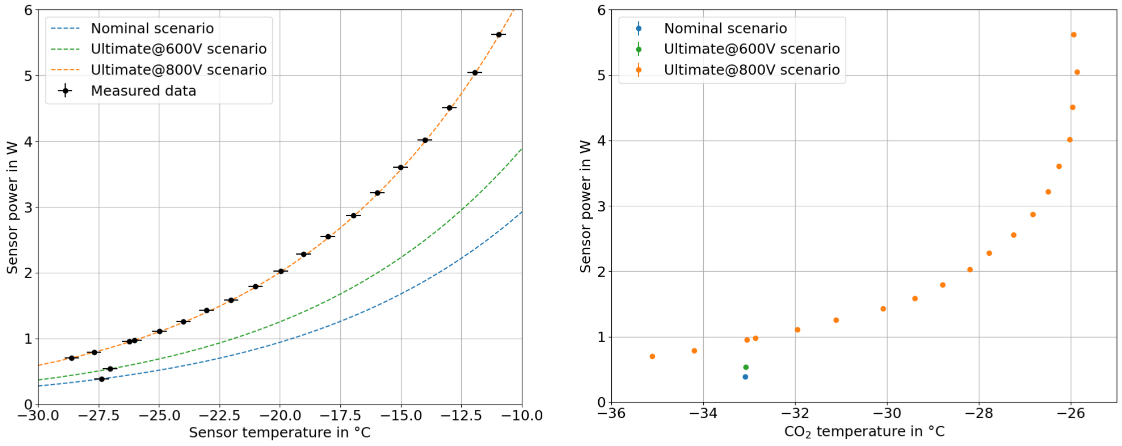

Figure 8.15: Left: measured sensor power against the measured sensor temperature for each measurement point in black. The expected sensor power per sensor temperature based on the power equation is shown for all three scenarios respectively in blue, green and orange. Right: measured sensor power against the measured CO_2 temperature for the measurement points of all three scenarios.

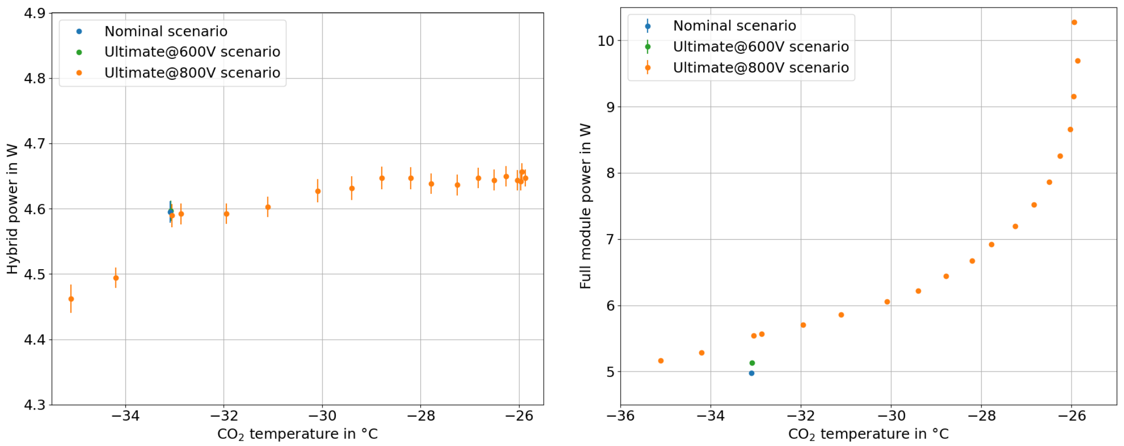

Figure 8.16: Left: measured hybrid power against the measured CO_2 temperature for the measurement points of all three scenarios. Right: measured full 2S module power against the measured CO_2 temperature for all three scenarios.

In the left plot in Figure 8.16 the measured hybrid power is shown against the measured CO_2 temperature for each measurement point. The uncertainty of the hybrid power was obtained by determining the standard deviation of the measured low voltage current for each measurement point and multiplying it with the applied low voltage of 10.5 V. It can be observed that for CO_2 temperatures below −30 °C the hybrid power decreases with decreasing CO_2 temperature. So far the hybrid power was estimated to be approximately constant for different operating temperatures but the measurement indicates that there is also a small dependency on the temperature. It is possible that the tuning of the module during the configuration before each measurement point is the cause for this, but this effect has not been investigated further within this thesis. Since the observed dependency is more significant for low CO_2 temperatures, it does not affect the incidence of the thermal runaway.

The right plot in Figure 8.16 displays the measured power of the full 2S module for each measurement point. The uncertainties of the sensor and hybrid power have been added but are not visible within the range of the plot. The full module power increases exponentially with increasing CO_2 temperature as expected until reaching a power consumption of 10.29 W at the point of thermal runaway.

Uncertainty of the CO_2 Temperature Measurement

For the investigation of the thermal runaway it is crucial to have a reliable measurement of the CO_2 temperature in order to give a proper estimate of the CO_2 temperature at which the runaway occurs. So far the CO_2 temperature has been determined by measuring the temperature of the cooling pipe at three points inside the cooling structure. Within the CO_2 cooling system it is also possible to assess the CO_2 temperature indirectly by measuring the pressure of the CO_2. In the CO_2 cooling system there are two pressure sensors that are positioned at point 3 and 6 in the CO_2 cooling system as visible in the sketch of the system in Figure A.1 in Appendix A. Since the pressure drop along the detector lines occurs between both pressure sensors, the CO_2 temperature can be obtained by calculating the mean CO_2 pressure out of the two pressure measurements for each thermal runaway measurement point. The measured pressure is then used to calculate the corresponding CO_2 temperature with a CO_2 calculator [19].

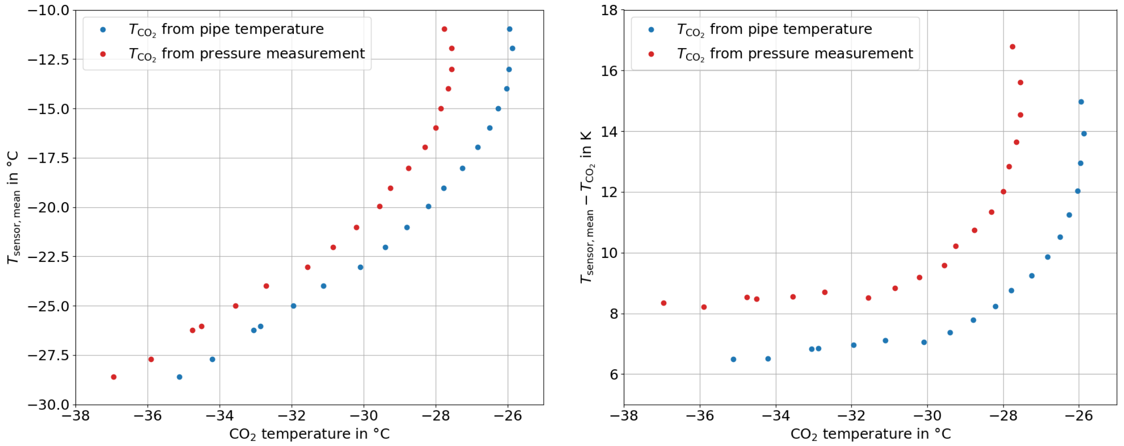

Figure 8.17: Left: mean sensor temperature against the CO_2 temperature. The blue data points show the CO_2 temperature based on the temperature measurement on the cooling pipe, while the red data points show the measurement with the CO_2 temperature on the basis of the pressure measurement of the CO_2. Right: temperature difference of the measured mean sensor temperature and the CO_2 temperature against the CO_2 temperature also showing the measurements based on the two different CO_2 temperature measurement methods.

In Figure 8.17 the left plot shows the measured mean sensor temperature against the CO_2 temperature where the blue data points represent the CO_2 temperature measurement based on the temperature measurement of the cooling pipe while the red data points display the CO_2 temperature measured on the basis of the mean measured CO_2 pressure. The right plot shows both measurements with the representation of the temperature difference between the sensor and the CO_2 against the measured CO_2 temperature. In these and the following plots the focus will shift to only the measurement points of the thermal runaway for the Ultimate@800V scenario without the other two scenarios.

Both plots show that there is a significant distance between the two different CO_2 temperature measurement methods. The 2S module would undergo the thermal runaway at −26 °C based on the temperature measurement on the cooling pipe, while the thermal runaway with a CO_2 temperature measured indirectly via the pressure yields a value of −28 °C. Since the CO_2 temperature measurement on the cooling pipe provides an upper limit on the true CO_2 temperature the observed effect can be taken into account by calculating a mean CO_2 temperature based on both CO_2 temperature measurements. The observed effect can then be accounted for by assessing the uncertainty on the CO_2 temperature by using the halved difference between the two temperatures. Since the measurement of the CO_2 temperature on the cooling pipe also has an additional uncertainty of 0.3 K, the final uncertainty of the CO_2 temperature is obtained by calculating the quadratic sum of the halved difference and the temperature measurement uncertainty of 0.3 K.

Discussion of the Thermal Runaway

The results of the measurement of the thermal runaway for the Ultimate@800V scenario using the combined CO_2 temperature values are shown in Figure 8.18. In the left plot the mean sensor temperature is plotted against the measured CO_2 temperature, while in the right plot the temperature difference between the sensor and the CO_2 against the CO_2 temperature can be found.

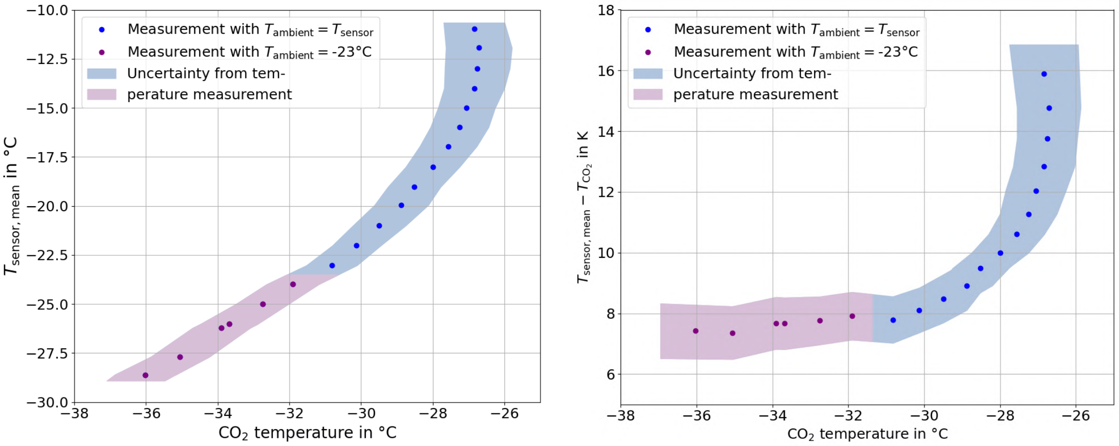

Figure 8.18: The left plot shows the measured mean sensor temperature against the measured CO_2 temperature, while the right plot shows the difference between the sensor and the CO_2 temperature against the CO_2 temperature. The error band in both plots covers the uncertainty arising from the measurement of the CO_2 temperature as well as the uncertainty of the measured sensor temperature. Two regions are distinguished in these plots: the region with an ambient temperature of −23 °C is marked in purple while the region with matching ambient and sensor temperature is depicted in blue.

The error bands depict the uncertainty that arises from the temperature measurement of the CO_2 as explained earlier. An uncertainty of 0.3 K is assumed for the measured sensor temperature which is also covered by the error bands. The region where a small heat exchange occurs between the sensors and the ambient as a result of the minimal ambient temperature of −23 °C is denoted in purple to distinguish it from the region with matching ambient temperature shown in blue. The measurement of the thermal runaway with the combined CO_2 temperature measurement results in a CO_2 temperature of −27 °C with an uncertainty of 1 K for the thermal runaway in the Ultimate@800V scenario and the used insert type in the cooling structure. In conclusion the measurement provides a sufficient margin for the occurrence of the thermal runaway of 6 K to the nominal operating CO_2 temperature of −33 °C.

8.3.3 Comparison with a Thermal Simulation

For the thermal runaway of the Ultimate@800V scenario a thermal simulation has been performed by Nicolas Röwert using the previously described thermal model of the 2S module. For the simulation the temperature dependent leakage current of the silicon sensors has been implemented according to the parameters of the Ultimate@800V scenario and applied to the two silicon sensors of the 2S module. By iterating through several CO_2 temperatures the mean sensor temperature can be determined and the thermal runaway curve obtained.

The heat transfer coefficient (htc) is an important parameter for the heat transfer at the interface of two materials, see Section 3.3.2 for the definition. The used value for the htc of the CO_2 to the inner wall of the cooling pipe in the simulation has an essential effect on the CO_2 temperature at which the thermal runaway occurs. Thus in fact two simulations with different htc values for the interface between the cooling pipe and the CO_2 have been performed. For the first simulation the commonly used htc value of 5 kW/m^2/K has been applied to the interface, which represents a more conservative approach.

In Ref. [20] the heat transfer between the inner wall of the cooling pipe and the boiling CO_2 has been measured in dependence of the heat flux density. For a temperature of $-30\,°C$ and a value of $7.5\,kW/m^2$ the htc is in the order of $5\,kW/m^2/K$, whereas a higher value of $10\,kW/m^2/K$ can be expected for $29.8\,kW/m^2$.

Within previous measurements at this institute [34] the heat flux density for a 2S module power in the order of 6 W has been estimated based on the contact surface of the insert and the cooling pipe yielding a value of $24\,kW/m^2$, which is closer to a value of $29.8\,kW/m^2$. Since the geometries of the inserts and the cooling pipe as well as the mass flow of the CO_2 are similar to the used setup in this thesis, this estimation is also applicable here. Based on this a higher htc of $10\,kW/m^2/K$ for the CO_2 represents a more realistic scenario so that a second simulation was performed using this value.

The results of the two simulations with an htc value of $5\,kW/m^2/K$ in green and $10\,kW/m^2/K$ in red as well as the measurement of the thermal runaway are presented in Figure 8.19 where the difference between the sensor and the CO_2 temperature is plotted against the CO_2 temperature. For the visualization of the measurement the same color code is used as explained in the previous section. The simulation with an htc of $5\,kW/m^2/K$ yields a CO_2 temperature of $-29.5\,°C$ for the thermal runaway, while the simulation with $10\,kW/m^2/K$ yields a value of $-28\,°C$. By comparing the two simulations it can be seen that the htc value for the interface of the cooling pipe and the CO_2 leads to a significant difference for the point of thermal runaway of 1.5 K. Additionally it can be observed that the increase of the htc value does not influence the shape of the curve itself but shifts the simulation with $10\,kW/m^2/K$ for CO_2 temperatures below $-31\,°C$ to lower temperature differences, while also shifting the temperature of the thermal runaway to higher CO_2 temperatures.

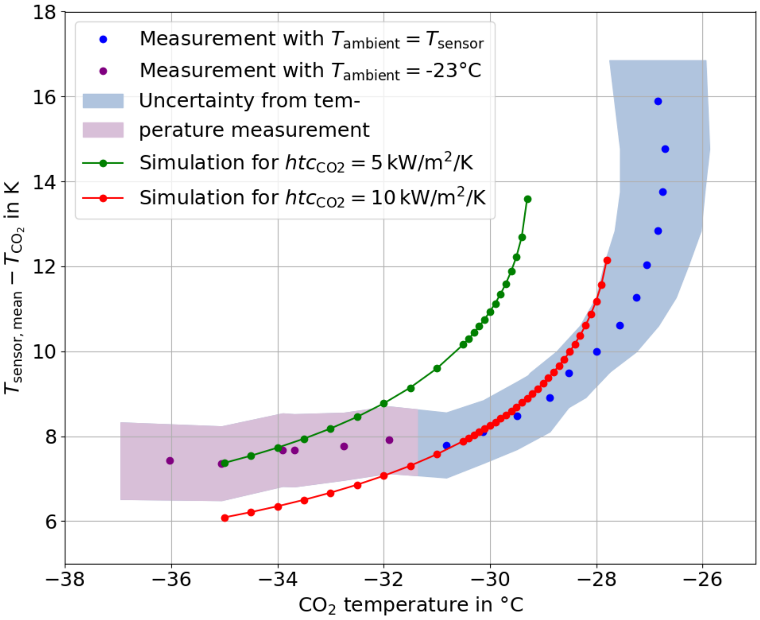

Figure 8.19: The plot shows the difference between the sensor temperature and the CO_2 temperature against the CO_2 temperature for the measurement of the Ultimate@800V scenario in blue/purple. Additionally a simulation of the thermal runaway for this scenario with a htc value of $5\,kW/m^2/K$ for the interface between the cooling pipe and the CO_2 is shown in green, while a second simulation with a value of $10\,kW/m^2/K$ is presented in red.

In addition to the modification of the htc value, the glue layer thickness between the kapton strips and the silicon sensors has been varied in the simulation. The results have shown that this has only a small impact on the CO_2 temperature of the thermal runaway with a temperature shift in the order of 0.1 K and is therefore negligible.

When comparing the measurement with a CO_2 temperature of $-27\,^{\circ}$C for the thermal runaway and the simulations, a distance of 2.5 K to the simulation with $5\,\mathrm{kW/m^2/K}$ and a distance of 1 K to the simulation with $10\,\mathrm{kW/m^2/K}$ can be observed. In general the measurement and simulations display a similar shape as the temperature difference between the sensor and the CO_2 rises with increasing CO_2 temperature. Overall the simulation with $10\,\mathrm{kW/m^2/K}$ matches better with the measurement and lays within the uncertainty of the measurement for CO_2 temperatures above $-31\,^{\circ}$C. This corresponds to the region in the measurement where the ambient temperature was set to the sensor temperature so that the sensors are in thermal equilibrium with the ambient. For CO_2 temperatures below $-31\,^{\circ}$C the simulated temperature differences between the sensor and the CO_2 are lower than the measured differences. In this region a small heat flux occurs from the ambient to the 2S module since the ambient temperature is above the sensor temperature at $-23\,^{\circ}$C. Consequently the measured temperature difference between the sensor and the CO_2 in this region would be smaller in case of a thermal equilibrium with the ambient. To conclude the observed deviation between the measurement and the simulation with a htc of $10\,\mathrm{kW/m^2/K}$ for CO_2 temperatures below $-31\,^{\circ}$C can be attributed to the heat exchange with the ambient as the simulation is performed without a heat exchange between the ambient and the sensors.

Apart from the simplified modeling of the hybrids in the simulation, as already discussed in Section 8.2.2, another difference between the measurement and the simulation is the modeling of the leakage current in the silicon sensors. The measurement concept for the thermal runaway is assuming a homogeneous distribution of the leakage current within the sensors, whereas the simulation takes into account the inhomogeneous heat generation that will occur for a real irradiated silicon sensor. Nevertheless this is estimated to only have a small effect on the measured point of thermal runaway. Also the CO_2 temperature has been set to the same value for all inserts in the simulation without taking into account the temperature differences of the individual inserts that can be observed during the measurement.

Overall the measurement and simulation exhibit a similar shape for increasing CO_2 temperatures while being in good agreement in the region where the ambient temperature is equal to the sensor temperature. This shows that they ultimately provide a reliable estimate for the expected point of thermal runaway for the Ultimate@800V scenario for a 2S module with a sensor spacing of 4.0 mm and six cooling contacts in the TEDD 2 region.

9 Summary

The 2S modules, as part of the new Phase-2 tracker, will exhibit a temperature-dependent leakage current after irradiation. Therefore it is crucial that the cooling system provides stable conditions throughout the operation of the detector to especially avoid the incidence of the thermal runaway. In the TEDD region of the Phase-2 tracker the 2S modules will be mounted onto aluminum inserts that provide the thermal interface to the cooling pipe. Within this thesis thermal measurements with a 2S module have been carried out on a small cooling structure similar to the dees in the TEDD region. A custom CO_2 cooling system as well as a module cooling box that minimizes the heat exchange with the ambient have been used.

To assess the thermal properties of the 2S module during the measurements a module with a sensor spacing of 4.0 mm and six cooling contacts has been successfully equipped with temperature sensors including the two silicon sensors. For this a dedicated gluing procedure has been developed and used to equip the top and bottom sensor of the 2S module as well as several components of the FEHs and SEH with temperature sensors. Prior to the gluing the temperature sensors have been thermally characterized at temperatures down to $-20\,°\mathrm{C}$ in the cooling bath of a chiller. An uncertainty of 0.3 K has been determined for the used temperature sensors.

The used inserts of the mini-TEDD structure are also equipped with temperature sensors inside the cooling structure. Before the integration of the 2S module the thermal resistance of the inserts has been determined as well with the use of a heating resistor. Within the measurements all inserts have been found to be properly connected to the cooling pipe. Additionally the thermal contact between the bridges of the 2S module and the inserts as a function of the applied torque has been investigated. With the use of a heating resistor glued to a stump bridge measurements with different torque values have been performed. The results indicate that a torque of 8 cNm or higher provides an optimized thermal contact between the bridge and the insert.

The 2S module was integrated onto the mini-TEDD structure and a noise scan was performed inside the module cooling box at room temperature. The strips at the location of the glued temperature sensors showed a strongly increased noise. Since the silicon sensors of the 2S module are not irradiated two LED strips have been implemented in the setup to emulate the expected leakage current of irradiated silicon sensors. A PID control has been developed with LabView that can adjust the leakage current according to the expected sensor temperature based on the power equation that has to be fulfilled for irradiated sensors. This allows to adjust the power consumption of the silicon sensor according to the expectation for three possible scenarios that are under investigation in the community. The three scenarios, namely the nominal, Ultimate@600V and Ultimate@800V scenario, represent different operation scenarios at the HL-LHC, with the Ultimate@800V scenario describing the operation in a case of maximal performance where the HL-LHC would reach $4000\,\mathrm{fb}^{-1}$ at the end of its lifetime.

Within this thesis thermal measurements of the 2S module for all three scenarios at the nominal operating CO_2 temperature of $-33\,°\mathrm{C}$ have been performed. Based on the analyzed temperature distributions on the 2S module for all three scenarios the thermal design of the 2S module can be validated. Additionally thermal simulations of the 2S module have been performed in this working group by Nicolas Röwert. For the nominal scenario a simulation has been compared to the measured temperature distribution. It has been observed that the mean temperature of the top and bottom sensor and the bridges of the 2S module are in good agreement with the simulation, with deviations below 1.5 K, while the measured and simulated temperatures of the different components of the SEH and FEHs exhibit significant deviations. This is a result of the simplified modeling of the electronics in the simulation. Still the comparison with the measurement shows that the simulated sensor temperatures can be used as a good estimate.

The thermal runaway curve of the 2S module in this setup has been measured for the Ultimate@800V scenario. For each measurement point the ambient temperature has been adjusted to the sensor temperature. A CO_2 temperature of −27 °C has been obtained for the point of thermal runaway, which corresponds to a margin of 6 K to the nominal operating temperature of −33 °C.

Furthermore two simulations of the thermal runaway have been conducted by Nicolas Röwert using htc values of $5\,\mathrm{kW/m^2/K}$ and $10\,\mathrm{kW/m^2/K}$ for the interface between the boiling CO_2 and the cooling pipe. The simulation with a htc value of $10\,\mathrm{kW/m^2/K}$ showed a better agreement to the measurement, yielding a value of −28 °C for the point of thermal runaway. While the measurement is dominated by the uncertainty of the measured CO_2 temperature the simulation is strongly influenced by the htc value of the CO_2. By studying these two effects in more detail the results of the measurement and the simulation can be enhanced further.

To conclude the presented results of the thermal runaway constitute the first measurement of its kind with a fully functional 2S module as well as the first thermal measurements on a TEDD-like cooling structure. Overall the results indicate that a sufficient margin is given with the nominal CO_2 temperature to the determined point of thermal runaway for a 2S module with a sensor spacing of 4.0 mm, six cooling contacts and the used insert type in an environment where the ambient temperature is equal to the mean sensor temperature. It would be interesting to study the thermal runaway for other cases such as a 2S module with a sensor spacing of 1.8 mm, five or six cooling contacts, the other insert type that is built-in in the mini-TEDD structure as well as to measure other operation scenarios in order to gain a deeper understanding of the thermal conditions in the endcap region of the detector.

Bibliography

[1] The CMS Collaboration, *Observation of a new boson at a mass of 125 GeV with the CMS experiment at the LHC*, Physics Letters B 716, 2012, pp. 30–61, DOI: `10.1016/j.physletb.2012.08.021`.

[2] L. Evans and P. Bryant, *LHC Machine*, JINST 3 S08001 (2008), DOI: `10.1088/1748-0221/3/08/s08001`.

[3] The CMS Collaboration, *The CMS experiment at the CERN LHC*, JINST 3 S08004 (2008), DOI: `10.1088/1748-0221/3/08/s08004`.

[4] CMS Collaboration, *The Phase-2 Upgrade of the CMS Tracker*, CERN-LHCC-2017-009, 2017, URL: `https://cds.cern.ch/record/2272264`.

[5] The ALICE Collaboration, *The ALICE experiment at the CERN LHC*, JINST 3 S08002 (2008), DOI: `10.1088/1748-0221/3/08/s08002`.

[6] The ATLAS Collaboration, *The ATLAS Experiment at the CERN Large Hadron Collider*, JINST 3 S08003 (2008), DOI: `10.1088/1748-0221/3/08/s08003`.

[7] The LHCb Collaboration, *The LHCb Detector at the LHC*, JINST 3 S08005 (2008), DOI: `10.1088/1748-0221/3/08/s08005`.

[8] A. Lopes and M. Perrey, *LHC Guide*, CERN-Brochure-2021-004-Eng, 2022, URL: `https://cds.cern.ch/record/2809109`.

[9] E. Lopienska, *The CERN accelerator complex*, CERN, 2022, URL: `https://cds.cern.ch/record/2800984`.

[10] CMS Collaboration, *CMS Luminosity - Public Results*, URL: `https://twiki.cern.ch/twiki/bin/view/CMSPublic/LumiPublicResults`.

[11] T. Sakuma, *CMS detector sketch*, 2019, URL: `https://cms-docdb.cern.ch/cgi-bin/PublicDocDB/RetrieveFile?docid=13631&filename=cms_160312_06.png`.

[12] The Tracker Group of the CMS Collaboration, *The CMS Phase-1 Pixel Detector Upgrade*, JINST 16 P02027 (2021), DOI: `10.1088/1748-0221/16/02/P02027`.

[13] I. Alonso et al., *High-Luminosity Large Hadron Collider (HL-LHC)*, CERN-2020-010, 2020, URL: `https://cds.cern.ch/record/2749422`.

[14] F. Luongo, *The CMS tracker upgrade for HL-LHC*, CMS Conference Report, CMS CR-2023/235, 2023.

[15] F. Hartmann, *Evolution of Silicon Sensor Technology in Particle Physics*, Springer, 2017, DOI: `10.1007/978-3-319-64436-3`.

[16] B. Verlaat, *Controlling a 2-phase CO2 loop using a 2-phase accumulator*, ICR07-B2-1565, 2007.

[17] LHCb Collaboration, *LHCb VELO (VErtex LOcator): Technical Design Report*, CERN-LHCC-2001-011, 2001, URL: `https://cds.cern.ch/record/504321`.

[18] P. Tropea et al., *CO2 evaporative cooling: The future for tracking detector thermal management*, Nucl. Instrum. Methods Phys. Res., A 824 (2016), pp. 473–475, URL: `https://doi.org/10.1016/j.nima.2015.08.052`.

[19] B. Wischnewski, CO_2 Calculator, URL: `https://www.peacesoftware.de/einigewerte/co2.html`.

[20] J. Wu et al., *Investigation of heat transfer and pressure drop of CO2 two-phase flow in a horizontal minichannel*, International Journal of Heat and Mass Transfer, Volume 54 Issues 9-10, 2011, pp. 2154–2162, URL: `https://doi.org/10.1016/j.ijheatmasstransfer.2010.12.009`.

[21] S. Venkateshan, *Heat Transfer*, Springer, 2021, DOI: `10.1007/978-3-030-58338-5`.

[22] F. Bianchi, INFN Perugia, private communication, Aug. 2023.

[23] G. Baldinelli et al., *The Tracker End-Cap Double Disks (TEDD) of the CMS Phase 2 Outer Tracker*, private communication, 2023.

[24] The Tracker Group of the CMS Collaboration, *Selection of the silicon sensor thickness for the Phase-2 upgrade of the CMS Outer Tracker*, JINST 16 P11028 (2021), DOI: `10.1088/1748-0221/16/11/P11028`.

[25] N. Röwert, *CAD Drawing 2S Module*, private communication, 2023.

[26] M. Prydderch et al., *CBC3: a CMS microstrip readout ASIC with logic for track-trigger modules at HL-LHC*, PoS TWEPP-17 (2018) 001, DOI: `10.22323/1.313.0001`.

[27] B. Nodari et al., *CIC: a radiation tolerant 65 nm data aggregation ASIC for the future CMS tracking detector at LHC*, JINST 18 C02035 (2023), DOI: `10.1088/1748-0221/18/02/C02035`.

[28] LpGBT Main Page, URL: `http://lpgbt-fpga.web.cern.ch/doc/html/`.

[29] J. Troska et al., *The VTRx+, an Optical Link Module for Data Transmission at HL-LHC*, PoS TWEPP-17 (2017) 048, DOI: `10.22323/1.313.0048`.

[30] DCDC Converter Project Website, URL: `https://espace.cern.ch/project-DCDC-new/_layouts/15/start.aspx#/index/Home.aspx`.

[31] S. Paoletti, INFN Florence, private communication, 2023.

[32] G. Lutz, *Semiconductor Radiation Detectors*, Springer, 1999, DOI: `10.1007/978-3-540-71679-2`.

[33] N. Röwert, *CAD Drawing Top Long Insert*, private communication, 2023.

[34] M. Rauch, *Thermal Measurements and Characterizations for the CMS Phase-1 Barrel Pixel Detector and the CMS Phase-2 Upgrade Tracker 2S Module with Evaporative CO2 Cooling Systems*, RWTH Aachen University, PhD Thesis, 2020.

[35] F. Scholz, *Untersuchung der Eigenschaften eines CO2-Kühlsystems für das Upgrade des CMS-Spurdetektors*, RWTH Aachen University, Bachelor Thesis, 2012.

[36] CMS working group at DESY, URL: `https://desy-cms.desy.de`.

[37] Swagelok, Double Ended Sample Cylinder, URL: `https://products.swagelok.com/en/c/dot-compliant-cylinders/p/304L-HDF4-1GAL`.

[38] Huber, Unistat 815 Circulation Thermostat, URL: `https://www.huber-online.com/en/products/dynamic-temperature-control-systems/unistats-down-to-120c/unistat-815-1`.

[39] Hanning, VARICON Three-phase Motor, URL: `https://www.all-electronics.de/wp-content/uploads/migrated/document/158069/57c643481cb.pdf`.

[40] Rheonik, RHM 015 Flow Sensor, URL: `https://www.rheonik.com/products/coriolis-sensor/rhm015/`.

[41] TE connectivity, Mini Betacurve (MBD) Thermistor Probe, URL: https://www.te.com/commerce/DocumentDelivery/DDEController?Action=showdoc&DocId=Data+Sheet%7FMBD_100K6MBD1%7FA%7Fpdf%7FEnglish%7FENG_DS_MBD_100K6MBD1_A.pdf%7FGA100K6MBD1.

[42] Aplisens, Smart Pressure Transmitter, URL: https://aplisens.com/apc-2000alw.html.

[43] Tektronix, Keithley 2701 Multimeter, URL: https://www.tek.com/en/products/keithley/switching-and-data-acquisition-systems/2700-multimeter-data-acquisition-switch-system.

[44] National Instruments, LabView Graphical Programming Environment, URL: https://www.ni.com/de/shop/labview.html.

[45] item Industrietechnik, Aluminum Construction Profiles, URL: https://www.item24.com/de-de/profiltechnik/konstruktionsprofile.

[46] Huber, Ministat 230 Circulation Thermostat, URL: https://www.huber-online.com/en/products/baths-and-circulators/cooling-heating-circulators/ministats-to-45c/ministat-230.

[47] SMC, PFM7 Digital Flow Switch, URL: https://www.smc.eu/en-gb/products/pfm7-2-color-display-digital-flow-switch-integrated-display~35976~cfg.

[48] IST, HYGROCHIP Humidity Sensor LabKit, URL: https://asset.conrad.com/media10/add/160267/c1/-/de/000505678DS01/datablad-505678-labkit-f-digital-humidity-sensors-hyt.pdf.

[49] armacell, Armaflex Sheets, URL: https://local.armacell.com/en/armacell-germany/products/afarmaflex/.

[50] Amphenol, NTC Thermistor MC65F103A, URL: https://f.hubspotusercontent40.net/hubfs/9035299/Documents/AAS-920-306C-NTC-Type-65-Series-031314-web.pdf.

[51] M. Guthoff, DESY, private communication, 2023.

[52] M. Guthoff et al., *Specifications for the Production of Support Structures for Silicon Detector Modules for the Upgrade of the CMS Tracker*, private communication, 2023.

[53] TE connectivity, Micro BetaCHIP (MCD) Thermistor Probe, URL: https://www.te.com/commerce/DocumentDelivery/DDEController?Action=showdoc&DocId=Data+Sheet%7FGA10K3MCD1%7FA%7Fpdf%7FEnglish%7FENG_DS_GA10K3MCD1_A.pdf%7FGA10K3MCD1.

[54] Dow Corning, SYLGARD 186 Silicone Elastomer, URL: https://www.dow.com/documents/en-us/productdatasheet/11/11-12/11-1253-sylgard-186-silicone-elastomer.pdf.

[55] BERGQUIST, Gap Filler TGF 4000, URL: https://www.henkel-adhesives.com/de/en/product/thermal-gap-fillers/bergquist_gap_fillertgf4000.html.

[56] BELEKTRONIG, OEM Peltier Module Air and Plate Cooler/Heater, URL: https://belektronig.de/en/pid-controller-products/accessories-temperature-control/oem-peltiercooler-heater/.

[57] BERGQUIST, Gap Filler TGF 2000, URL: https://www.henkel-adhesives.com/de/en/product/thermal-gap-fillers/bergquist_gap_fillertgf2000.html.

[58] Kerafol, KERATHERM Thermal Grease KP 92, URL: `https://asset.conrad.com/media10/add/160267/c1/-/en/000189070DS02/datasheet-189070-kerafol-keratherm-kp92-78-g-thermally-conductive-paste-10-wmk-78-g-max-temperature-200-c.pdf`.

[59] LUMITRONIX, LumiFlex 300 LED-Streifen, URL: `https://www.leds.de/cdn/shop/files/36347_de_Datenblatt_LumiFlex300_Economy_LED-Streifen_4000K_300_LEDs_5m_12V_R2R.pdf?v=13508408589667365151`.

[60] Rhode & Schwarz, Hameg HMP4040 Programmable Power Supply, URL: `https://www.rohde-schwarz.com/de/produkte/messtechnik/dc-netzgeraete/rs-hmp4000-netzgeraeteserie_63493-47360.html?change_c=true`.

[61] Tektronix, Keithley 2410 High Voltage SourceMeter, URL: `https://www.tek.com/en/products/keithley/source-measure-units/2400-standard-series-sourcemeter`.

[62] TRU Components, TCP10S 200R Resistor, URL: `https://asset.re-in.de/add/160267/c1/-/en/001625331DS01/DA_TRU-COMPONENTS-TCP10S-A2R00JTB-Hochlast-Widerstand-2-radial-bedrahtet-TO-126-20W-5-1St..pdf`.

[63] Polytec PT, Polytec EP 601-LV, URL: `https://www.polytecstore.fr/polytec_images/documents/FT_PT/ep/polytec-ep-601-lv_en.pdf`.

[64] M. Pesaresi et al., *The FC7 AMC for generic DAQ & control applications in CMS*, JINST 10 C03036 (2015), DOI: `10.1088/1748-0221/10/03/C03036`.

[65] F. Ravera, Phase-2 Acquisition and Control Framework, URL: `https://gitlab.cern.ch/cms_tk_ph2/Ph2_ACF`.

[66] N. Röwert, *Assembly and Characterization of a First Functional 2S Module for the CMS Phase-2 Upgrade at LHC*, RWTH Aachen University, Master Thesis, 2018.

[67] G. Bianchi et al., Irradiation Outer Tracker, URL: `https://ghugo.web.cern.ch/ghugo/layouts/test/OT616_IT613_power/irradiation_Outer.html`.

[68] C. Turrioni, *Thermal model of the 2S module*, private communication, INFN Perugia.

[69] Thermal Analysis Software ANSYS, URL: `https://www.ansys.com/applications/thermal-analysis-simulation-software`.

[70] N. Röwert, RWTH Aachen University, ongoing doctorate.

A Cooling System, Module Cooling Box and Cooling Structure

In the following a schematic overview of the CO_2 cooling system, additional pictures of the module cooling box and the CO_2 cooling system as well as a CAD drawing of the cooling structure can be found.

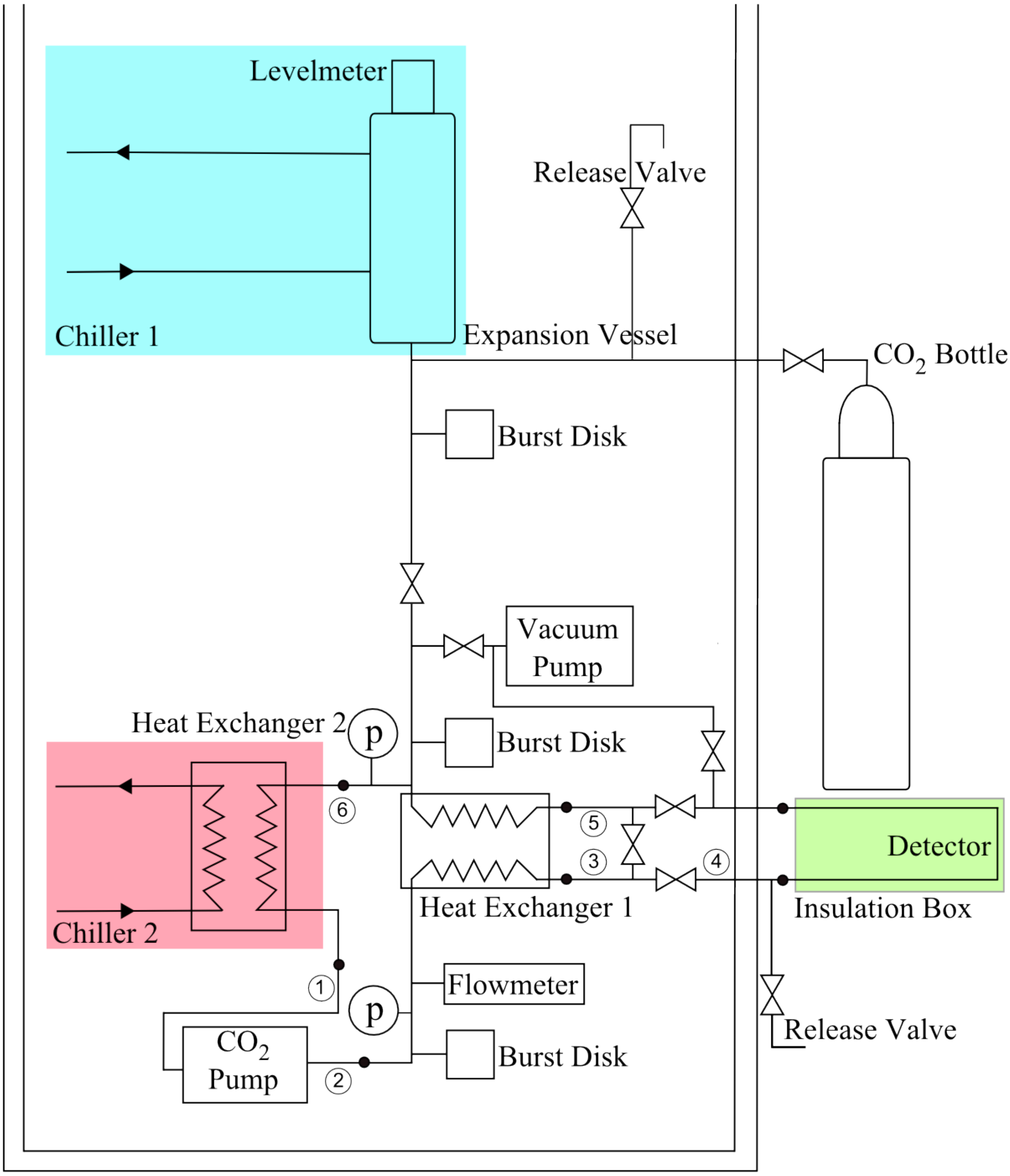

Figure A.1: Schematic overview of the main components of the custom-built CO_2 cooling system that has been used for the thermal measurements in this thesis. The cooling system is based on the 2PACL method.

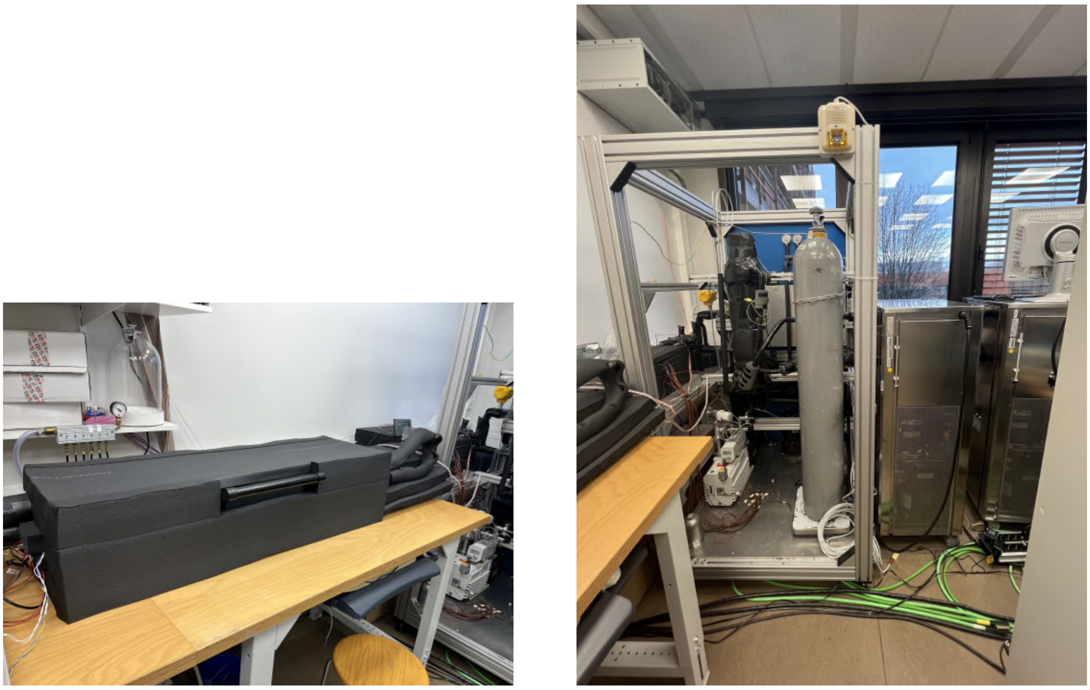

Figure A.2: Left: picture of the closed module cooling box in the laboratory. The connection of the cooling structure inside the box to the CO_2 cooling system is made from the right side of the box. The chiller that actively cools the module cooling box is connected on the left side. It is not visible in this picture. Right: picture of the CO_2 cooling system in the laboratory. The main tubing as well as the CO_2 pump, the flow meter, the pressure sensors et cetera are located in the ITEM rack on the left. The two big Huber chillers that are used to control the temperature of the accumulator vessel and the heat exchanger that is installed before the CO_2 pump can be seen on the right next to the rack.

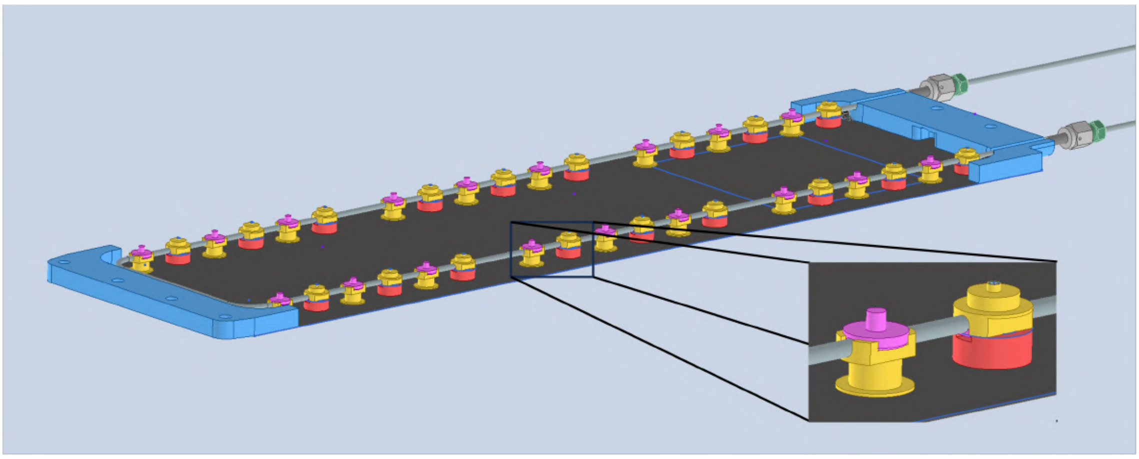

Figure A.3: CAD drawing of the mini-TEDD structure that is used as a cooling structure for the 2S module in this thesis. The cooling pipe as well as the inserts glued to the cooling pipe can be seen. The zoom in the right corner shows the two insert types that are used in this structure. The structure is shown here in the same orientation as it is mounted in the module cooling box.

B Characterization of Temperature Sensors

For the measurement of the temperature distribution on the 2S module several small NTC thermistor probes [41] have been available from previous measurements at this institute. Within characterization measurements of these sensors at a temperature of −15 °C it has been observed that the measured temperatures of the individual temperature sensors exhibit large deviations in the order of 4 K in comparison with each other. The examination of a few temperature probes under the microscope has shown that individual probe tips exhibit small cracks that contribute to the observed aging effect. In Figure B.1 two microscope pictures are exemplary shown for one temperature sensor. It can be clearly seen that this sensor has a damaged tip with a small crack in the middle.

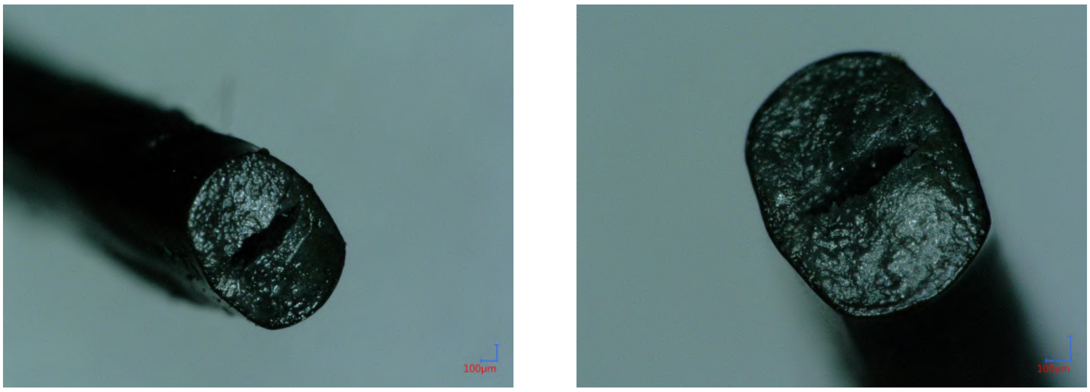

Figure B.1: Two microscope pictures of a temperature sensor that has a damaged sensor tip.

C Measurement of the Noise

The noise of a 2S module is determined with a noise scan that is performed for each strip of the two silicon sensors. For this a threshold scan is performed that measures the occupancy of each channel with increasing threshold value. The occupancy is defined as the number of measured noise signals divided by the total number of events. High V_{CTH} values correspond to low physical thresholds. The obtained result of such a threshold scan has the form of a so-called S-curve since the occupancy increases with increasing V_{CTH} values until it reaches a value of 1.0 which is the point where all noise signals surpass the threshold. An example for such a S-curve can be found in Figure C.1. It shows the S-curve for a strip of CBC 0 of FEH 0 of the used 2S module 2S_40_6_AAC-00003. The noise is defined as the width of the S-curve.

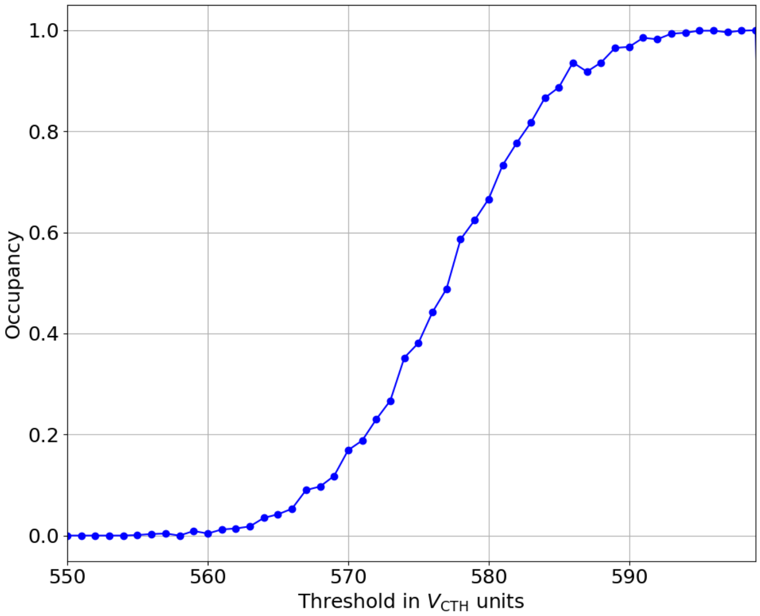

Figure C.1: Result of the measured S-curve from a channel of CBC 0 of FEH 0 from the 2S module 2S_40_6_AAC-00003.

Danksagung

An dieser Stelle möchte ich mich noch bei Allen bedanken, die mich das Jahr über unterstützt haben.

An erster Stelle möchte ich mich bei Prof. Dr. Lutz Feld für die Möglichkeit bedanken, meine Masterarbeit in seiner Arbeitsgruppe schreiben zu können. Seine vielen Erklärungen, Vorschläge und Hinweise haben wesentlich zum Fortschritt dieser Arbeit beigetragen. Auch für die vielen Möglichkeiten zur Teilnahme an verschiedenen Tagungen und Konferenzen, wie der DPG-Frühjahrstagung, dem CMS FSP-Meeting am DESY und den Tracker Weeks am CERN und in Santander, möchte ich mich bedanken.

Bei Prof. Dr. Oliver Pooth möchte ich mich für die vielen hilfreichen Kommentare in unseren wöchentlichen Meetings als auch für die Übernahme der Zweitkorrektur dieser Arbeit bedanken.

Ein großer Dank gilt Dr. Katja Klein für die außerordentlich gute Betreuung über die gesamte Arbeit hinweg. Ich möchte mich für alle Überlegungen zu verschiedensten Fragestellungen und die vielen konstruktiven Diskussionen zu allen möglichen Problemen bedanken. Insbesondere für das Korrekturlesen dieser Arbeit möchte ich mich noch bei ihr bedanken.

Ein besonderer Dank gilt Nicolas Röwert, der mich als Doktorand während der gesamten Zeit betreut hat. Ich möchte mich bei ihm für die vielen Ideen und die tolle Unterstützung bei allen aufkommenden Problemen im Rahmen der zahlreichen Vorbereitungen als auch bei den thermischen Messungen bedanken. Insbesondere für die gute Zusammenarbeit bei den thermischen Simulationen und der Bereitstellung dieser für meine Arbeit möchte ich mich bedanken.

Im Allgemeinen möchte ich mich für die angenehme Arbeitsatmosphäre in der Arbeitsgruppe bedanken. Dabei möchte ich mich insbesondere bei Dr. Martin Lipinski für die Einführung in die Bedienung der CO_2 Anlage und die Beantwortung aller Fragen rund um das Kühlsystem und LabView, als auch bei Alexander Pauls für die vielen Erklärungen und Diskussionen zu allen möglichen Fragen rund um das 2S Modul, bedanken. Michael Wlochal und Clara Ebisch danke ich für die gute Beratung und Untersützung im Bereich der Mechanik. Auch bei meinem Co-Masteranden Felix Thurn möchte ich mich für den guten Austausch über die gesamte Zeit bedanken.

Abschließend möchte ich mich noch bei meiner Familie und Freunden für die Unterstützung während des gesamten Studiums bedanken.